

Industrial

Electronics

Biomedical

Civil

Aerospace

Computer

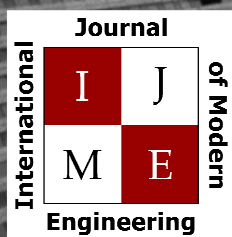
Electrical

Chemical

Mechanical



ENGINEERING



[www.ijme.us](http://www.ijme.us)

Print ISSN: 2157-8052  
Online ISSN: 1930-6628



[www.iajc.org](http://www.iajc.org)

## INTERNATIONAL JOURNAL OF MODERN ENGINEERING

### ABOUT IJME:

- IJME was established in 2000 and is the first and official flagship journal of the International Association of Journal and Conferences (IAJC).
- IJME is a high-quality, independent journal steered by a distinguished board of directors and supported by an international review board representing many well-known universities, colleges and corporations in the U.S. and abroad.
- IJME has an impact factor of **3.00**, placing it among the top 100 engineering journals worldwide, and is the #1 visited engineering journal website (according to the National Science Digital Library).

### OTHER IAJC JOURNALS:

- The International Journal of Engineering Research and Innovation (IJERI)  
For more information visit [www.ijeri.org](http://www.ijeri.org)
- The Technology Interface International Journal (TIIJ).  
For more information visit [www.tiij.org](http://www.tiij.org)

### IJME SUBMISSIONS:

- Manuscripts should be sent electronically to the manuscript editor, Dr. Philip Weinsier, at [philipw@bgsu.edu](mailto:philipw@bgsu.edu).

For submission guidelines visit  
[www.ijme.us/submissions](http://www.ijme.us/submissions)

### TO JOIN THE REVIEW BOARD:

- Contact the chair of the International Review Board, Dr. Philip Weinsier, at [philipw@bgsu.edu](mailto:philipw@bgsu.edu).

For more information visit  
[www.ijme.us/ijme\\_editorial.htm](http://www.ijme.us/ijme_editorial.htm)

### INDEXING ORGANIZATIONS:

- IJME is currently indexed by 22 agencies.  
For a complete listing, please visit us at [www.ijme.us](http://www.ijme.us).

### Contact us:

**Mark Rajai, Ph.D.**

Editor-in-Chief  
California State University-Northridge  
College of Engineering and Computer Science  
Room: JD 4510  
Northridge, CA 91330  
Office: (818) 677-5003  
Email: [mrajai@csun.edu](mailto:mrajai@csun.edu)



[www.tiij.org](http://www.tiij.org)



[www.ijeri.org](http://www.ijeri.org)

---

# INTERNATIONAL JOURNAL OF MODERN ENGINEERING

The INTERNATIONAL JOURNAL OF MODERN ENGINEERING (IJME) is an independent, not-for-profit publication, which aims to provide the engineering community with a resource and forum for scholarly expression and reflection.

IJME is published twice annually (fall and spring issues) and includes peer-reviewed articles, book and software reviews, editorials, and commentary that contribute to our understanding of the issues, problems, and research associated with engineering and related fields. The journal encourages the submission of manuscripts from private, public, and academic sectors. The views expressed are those of the authors and do not necessarily reflect the opinions of the IJME editors.

## EDITORIAL OFFICE:

Mark Rajai, Ph.D.  
Editor-in-Chief  
Office: (818) 677-2167  
Email: [ijmeeditor@iajc.org](mailto:ijmeeditor@iajc.org)  
Dept. of Manufacturing Systems  
Engineering & Management  
California State University-  
Northridge  
18111 Nordhoff Street  
Northridge, CA 91330-8332

## THE INTERNATIONAL JOURNAL OF MODERN ENGINEERING EDITORS

### *Editor-in-Chief:*

**Mark Rajai**

California State University-Northridge

### *Associate Editor:*

**Li Tan**

Purdue University North Central

### *Production Editor:*

**Philip Weinsier**

Bowling Green State University-Firelands

### *Subscription Editor:*

**Morteza Sadat-Hossieny**

Northern Kentucky University

### *Executive Editor:*

**Paul Wilder**

Vincennes University

### *Publisher:*

**Bowling Green State University-Firelands**

### *Manuscript Editor:*

**Philip Weinsier**

Bowling Green State University-Firelands

### *Copy Editor:*

**Li Tan**

Purdue University North Central

### *Technical Editors:*

**Michelle Brodke**

Bowling Green State University-Firelands

**Paul Akangah**

North Carolina A&T State University

**Marilyn Dyrud**

Oregon Institute of Technology

### *Web Administrator:*

**Saeed Namyar**

Advanced Information Systems

---

# TABLE OF CONTENTS

<i>Editor's Note: Rear Axle Housing Design for a Ford Mustang Shelby GT500</i> .....	3
Philip Weinsier, IJME Manuscript Editor	
<i>High-rise Building Response Comparison: Use of Time Domain Scaling versus Spectral Matching Input Ground Motion</i> .....	5
Mohammad T. Bhuiyan, West Virginia State University	
<i>Design and Test of a High-Speed Actuator for Gas Mixing and Flow-Control Applications</i> .....	16
Todd D. Batzel, Pennsylvania State University, Altoona College; Christopher R. Martin, Pennsylvania State University, Altoona College; Dimitris W. Kiaoulas, Pennsylvania State University, Altoona College; Matthew J. Cowler, Pennsylvania State University, Altoona College	
<i>Footage Estimation of Moving Objects by Multi-Camera Triangulation through Wireless Networks</i> .....	25
Sangho Park, Central Connecticut State University; Xiaobing Hou, Central Connecticut State University	
<i>Numerical Flow Visualization of a Rectangular Shell-and-Tube Thermosyphon Heat Exchanger with Baffled Crossflow</i> .....	34
Mebougna Drabo, Alabama A&M University; He Tao, Stony Brook University; Wei Zhong, Stony Brook University; Jon P. Longtin, Stony Brook University; Thomas Butcher, Brookhaven National Laboratory; Narinder Tutu, Brookhaven National Laboratory; Rebecca Trojanowski, Brookhaven National Laboratory	
<i>Optimal Design of an Automotive Rear Axle Housing</i> .....	42
Diane L. Peters, Kettering University; Yaomin Dong, Kettering University; Vimal Patel, Kettering University	
<i>Stability and Transparency in Bilateral Teleoperation via Continuous Pole Placement</i> .....	49
Theophilus Okore-Hanson, North Carolina A&T State University; Sun Yi, North Carolina A&T State University; Sameer Hamoush, North Carolina A&T State University; Younho Seong, North Carolina A&T State University	
<i>Analysis and Simulation of Networks with Virtual Cut-Through Routing</i> .....	56
Lev B. Levitin, Boston University; Yelena Rykalova, UMass Lowell	
<i>Instructions for Authors: Manuscript Formatting Requirements</i> .....	66

# IN THIS ISSUE (P.42)

## REAR AXLE HOUSING DESIGN FOR A FORD MUSTANG SHELBY GT500

Philip Weinsier, IJME Manuscript Editor

If you drive a car, you are likely aware of gas prices and the fuel economy of your vehicle. You may also understand that decreasing the weight of your vehicle is an integral part of fuel economy. However, you might be a muscle car enthusiast and worry less about your machine's fuel economy and more about its performance. Regardless of your driving choices, vehicle design is constantly in flux, technology improves, and new analysis techniques are developed to improve vehicle performance. In this current article, the authors focus on legacy parts—in this case, the 8.8-inch rear axle center housing from a 2013 Ford Mustang Shelby GT500—which they feel are good candidates for re-design.

In a report by the U.S. DOT National Highway Traffic Safety Administration's Energy Policy and Conservation Act (EPCA), they specifically direct the Department to balance the technological and economic challenges related to fuel economy with the nation's need to conserve energy. Additional notes from this U.S. DOT report tell us what we basically already know: greenhouse gas emissions from the consumption of fossil fuels, specifically CO<sub>2</sub>, are a global problem. "Studies by multiple sources suggest that rising atmospheric concentrations of greenhouse gases will damage human health and welfare. There is a direct linkage between the consumption of fossil energy and emissions of the greenhouse gas carbon dioxide, as essentially all of the carbon in hydrocarbon fuels is oxidized into carbon dioxide when the fuel is combusted."

There are numerous ways to improve vehicle fuel efficiency; many are in the hands of the driver, but others are not—one of which is reducing weight. Sure, leaving a couple friends or family members at home will work, but the authors of this current article focused on reducing the weight of the rear axle housing. The authors were able to reduce the weight of their axle housing by about 90 lbs. According to NHTSA, this would save 0.25 mpg (~1%, similar to estimates from fueleconomy.gov). If the average car is driven 13,476 miles/year (U.S. DOT, Federal Highway Commission) and gets 24.7 mpg (Reuters), that equals 545 gallons/year at \$2.66/gallon (AAA) for \$1451/year. For a similar car weighing 90 lbs. less, it would use 540 gallons/year at a cost of \$1437; a savings of ~\$13.3/year. Not a big deal for an individual driver. However, according to the U.S. DOT Bureau of Transportation Statistics, there are

currently around 200,000,000 light-duty vehicles on the road in the U.S. alone, racking up 2.7 billion miles annually. So now, as a nation, we are looking at consuming 108,216,433 gallons (at 24.95 mpg) versus 109,311,741 gallons (at 24.7 mpg), for a savings of 1,095,308 gallons—or \$2,913,519—annually.



Granted, a few million dollars alone is generally not enough to sway politicians to make policy changes; nor would it even garner a passing glance from auto makers. But add to the calculation the amount of CO<sub>2</sub> emissions and other pollutants belching from our vehicles, and suddenly the problem gets attention. So the fundamental question becomes: why not incorporate a design change that will improve performance—or at least not diminish it—and reduce weight? I just gave you the short answer based on fuel economy and reduced noxious emissions.

For a detailed description of how to achieve weight reduction in the rear axle housing of a 2013 Ford Mustang Shelby GT500, see the article on page 42 in this issue of IJME. In this article, the authors describe the optimization of a Mustang's rear axle housing, which was conducted using the optimization and FEA capabilities of NXTM (Siemens PLM software). Their objective was to minimize the weight of the axle housing, subject to constraints on the maximum stress in the housing. The optimization was conducted twice, once with a single design variable and once with five design variables. In both cases, the optimization problem converged to an optimal design, and the weight was reduced. In the first case, the weight of the housing was reduced by 15%; in the second case, it was reduced by 47%. As noted above, such reductions could be expected to have a large impact on fuel economy and performance of the vehicle.

## Editorial Review Board Members

Mohammed Abdallah	State University of New York (NY)	Troy Ollison	University of Central Missouri (MO)
Paul Akangah	North Carolina A&T State University (NC)	Reynaldo Pablo	Purdue Fort Wayne (IN)
Nasser Alaraje	Michigan Tech (MI)	Basile Panoutsopoulos	Community College of Rhode Island (RI)
Ali Alavizadeh	Purdue University Northwest (IN)	Shahera Patel	Sardar Patel University (INDIA)
Lawal Anka	Zamfara AC Development (NIGERIA)	Thongchai Phairoh	Virginia State University (VA)
Jahangir Ansari	Virginia State University (VA)	Huyu Qu	Broadcom Corporation
Kevin Berisso	Memphis University (TN)	Desire Rasolomampionona	Warsaw University of Tech (POLAND)
Pankaj Bhambri	Guru Nanak Dev Engineering (INDIA)	Michael Reynolds	University of West Florida (FL)
Michelle Brodke	Bowling Green State Univ. Firelands (OH)	Nina Robson	California State University-Fullerton (CA)
Shaobiao Cai	Minnesota State University (MN)	Marla Rogers	Wireless Systems Engineer
Rajab Challoo	Texas A&M University Kingsville (TX)	Dale Rowe	Brigham Young University (UT)
Isaac Chang	Illinois State University (IL)	Karen Ruggles	DeSales University (PA)
Shu-Hui (Susan) Chang	Iowa State University (IA)	Anca Sala	Baker College (MI)
Rigoberto Chinchilla	Eastern Illinois University (IL)	Alex Sergeev	Michigan Technological University (MI)
Phil Cochrane	Indiana State University (IN)	Mehdi Shabaninejad	Zagros Oil & Gas Company (IRAN)
Curtis Cohenour	Ohio University (OH)	Hiral Shah	St. Cloud State University (MN)
Emily Crawford	Claflin University (SC)	Mojtaba Shivaie	Shahrood University of Technology (IRAN)
Dongyang (Sunny) Deng	North Carolina A&T State University (NC)	Musibau Shofoluwe	North Carolina A&T State University (NC)
Z.T. Deng	Alabama A&M University (AL)	Amitkumar B. Solanki	Government Engineering College (INDIA)
Sagar Deshpande	Ferris State University (MI)	Jiahui Song	Wentworth Institute of Technology (MA)
David Domermuth	Appalachian State University (NC)	Carl Spezia	Southern Illinois University (IL)
Marilyn Dyrud	Oregon Institute of Technology (OR)	Michelle Surerus	Ohio University (OH)
Mehran Elahi	Elizabeth City State University (NC)	Harold Terano	Camarines Sur Polytechnic (PHILIPPINES)
Ahmed Elsayy	Tennessee Technological University (TN)	Sanjay Tewari	Missouri University of Science & Tech (MO)
Cindy English	Millersville University (PA)	Vassilios Tzouanas	University of Houston Downtown (TX)
Ignatius Fomunung	University of Tennessee Chattanooga (TN)	Jeff Ulmer	University of Central Missouri (MO)
Ahmed Gawad	Zagazig University EGYPT)	Abraham Walton	University of South Florida Polytechnic (FL)
Mohsen Hamidi	Utah Valley University (UT)	Haoyu Wang	Central Connecticut State University (CT)
Mamoon Hammad	Abu Dhabi University (UAE)	Jyhwen Wang	Texas A&M University (TX)
Gene Harding	Purdue Polytechnic (IN)	Boonsap Witchayangkoon	Thammasat University (THAILAND)
Bernd Haupt	Penn State University (PA)	Shuju Wu	Central Connecticut State University (CT)
Youcef Himri	Safety Engineer in Sonelgaz (ALGERIA)	Baijian (Justin) Yang	Purdue University (IN)
Delowar Hossain	City University of New York (NY)	Eunice Yang	University of Pittsburgh Johnstown (PA)
Xiaobing Hou	Central Connecticut State University (CT)	Xiaoli (Lucy) Yang	Purdue University Calumet (IN)
Shelton Houston	University of Louisiana Lafayette (LA)	Faruk Yildiz	Sam Houston State University (TX)
Ying Huang	North Dakota State University (ND)	Yuqiu You	Ohio University (OH)
Christian Bock-Hyeng	North Carolina A&T University (NC)	Pao-Chiang Yuan	Jackson State University (MS)
Pete Hylton	Indiana University Purdue (IN)	Jinwen Zhu	Missouri Western State University (MO)
John Irwin	Michigan Tech (MI)		
Toqeer Israr	Eastern Illinois University (IL)		
Sudershan Jetley	Bowling Green State University (OH)		
Alex Johnson	Millersville University (PA)		
Rex Kanu	Purdue Polytechnic (IN)		
Reza Karim	North Dakota State University (ND)		
Manish Kewalramani	Abu Dhabi University (UAE)		
Tae-Hoon Kim	Purdue University Calumet (IN)		
Chris Kluse	Bowling Green State University (OH)		
Doug Koch	Southeast Missouri State University (MO)		
Resmi Krishnankuttyrema	Bowling Green State University (OH)		
Zaki Kuruppallil	Ohio University (OH)		
Shiyoung Lee	Penn State University Berks (PA)		
Soo-Yen (Samson) Lee	Central Michigan University (MI)		
Chao Li	Florida A&M University (FL)		
Dale Litwhiler	Penn State University (PA)		
Mani Manivannan	ARUP Corporation		
G.H. Massiha	University of Louisiana (LA)		
Thomas McDonald	University of Southern Indiana (IN)		
David Melton	Eastern Illinois University (IL)		
Shokoufeh Mirzaei	Cal State Poly Pomona (CA)		
Sam Mryyan	Excelsior College (NY)		
Jessica Murphy	Jackson State University (MS)		
Rungun Nathan	Penn State Berks (PA)		
Arun Nambiar	California State University Fresno (CA)		
Aurenice Oliveira	Michigan Tech (MI)		

# HIGH-RISE BUILDING RESPONSE COMPARISON: USE OF TIME DOMAIN SCALING VERSUS SPECTRAL MATCHING INPUT GROUND MOTION

Mohammad T. Bhuiyan, West Virginia State University

## Abstract

When performing non-linear response history analyses of high-rise buildings, designers and researchers come across some crucial modeling questions. Use of appropriately selected and scaled ground motion is one of them. Once appropriate ground motions are selected, the next question is how these ground motion time histories must be modified in order to be compatible with the design target acceleration response spectrum. Modification can be performed in two ways: (a) direct time domain scaling of the acceleration time-histories of the ground motion values; and, (b) transforming the time-acceleration data into the frequency domain, making adjustments (compatible with the target spectrum) and then transforming them back into the time domain. Both methods are mentioned in Guidelines for Performance-based Seismic Design of Tall Buildings (PEER 2010/05) and FEMA P-1050-1/2105 Edition. ASCE 7-10 mentions the direct scaling approach, but does not explicitly mention the other method. The objective of this study, then, was to determine the extent to which the responses of high-rise buildings using both time domain-scaled and frequency domain-adjusted ground motions differed. Several sample structures were selected for analysis: (a) a 42-story concrete dual-core wall-frame structure; (b) a 40-story steel space frame structure; and, (c) a 40-story buckling-restraint-braced frame structure. Detailed non-linear models of these structures were developed in PERFORM-3D. Seven sets of appropriate ground motions were selected for the non-linear time-history analyses. Results from the analyses showed differences (for example, in story acceleration, story shear, story moment, story drift, etc.) in the responses of these buildings using time domain-scaled and spectral matching-input ground motions.

## Introduction

Recent decades have seen a surge in high-rise building construction around the world in high-seismic areas. In the design of such buildings, it is of paramount importance to the designer to select appropriate ground motions and scale those motions for the numerical analysis and evaluation of the design. How to appropriately scale selected ground motions (so as to be compatible with a target spectrum) is an

important decision for the designer. Two methods are: (a) direct time-domain scaling, and (b) transforming the time-acceleration data into the frequency domain, making adjustments (compatible with the target spectrum) and then transforming them back into the time domain. Both methods are mentioned in the building guidelines and codes. The objective of this study, then, was to determine the extent to which the responses of high-rise buildings using both time domain-scaled and frequency domain-adjusted ground motions differed.

## Case Study Buildings

Three structures were selected for this study: (a) a 42-story concrete dual-core wall-frame structure; (b) a 40-story buckling-restraint-braced frame structure; and, (c) a 40-story steel space-frame structure. The first two structures were used by Pacific Earthquake Engineering Research Center's (PEER) Tall Buildings Initiative in their case studies (Moehle et al., 2011). The third structure was used by Hutt (2013) for his case study. Figure 1 shows that the 42-story dual-core wall-frame special-moment building had 42 stories above ground, four stories below ground, and a penthouse. Figures 1 and 2 show that the dual system had a core wall and four-bay special-moment resisting frame at the perimeter of the building. Figure 1 also shows a detailed non-linear model, developed in PERFORM-3D (2011), and a 3D rendering of the structure.

Figure 3 shows the footprint of the above-ground 40-story buckling-restraint-braced (BRB) frame structure was 170 ft. by 107 ft. It also shows the location of buckling-restrained chevron braces. Figure 4 shows that the building consisted of four basement levels. The foot print of the basement level was 227 ft. by 220 ft. Lateral forces were entirely resisted by buckling restraint braces. PERFORM 3D was used to develop a detailed non-linear model for the numerical analyses in this study. The 40-story steel space frame structure consisted of special-moment resisting frames in both directions. Figure 5 shows that this particular structure had three basement levels and a footprint of 120 ft. by 80 ft. Like the other two structures, a detailed non-linear model was developed in PERFORM 3D (see Figure 5).

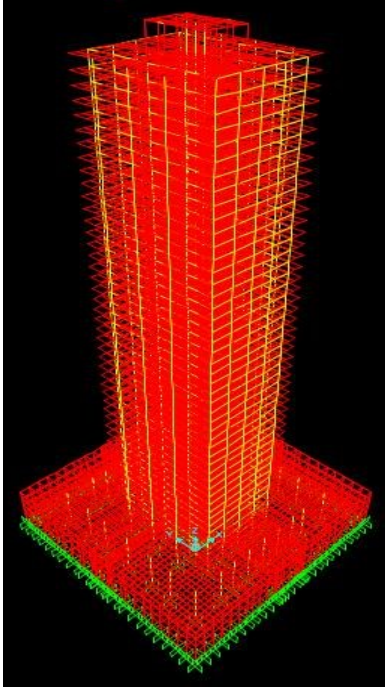


Figure 1. 42-story core wall special moment frame: typical plan view at ground floor and below. Reprinted with Permission.

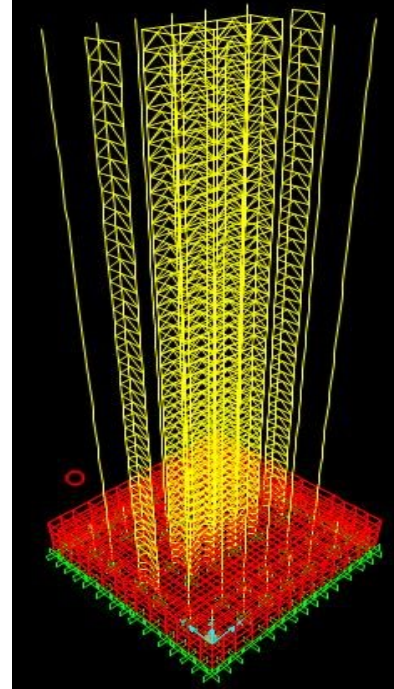


Figure 4. Three-dimensional rendering of the 40-story BRB structure from the PERFORM-3D model.

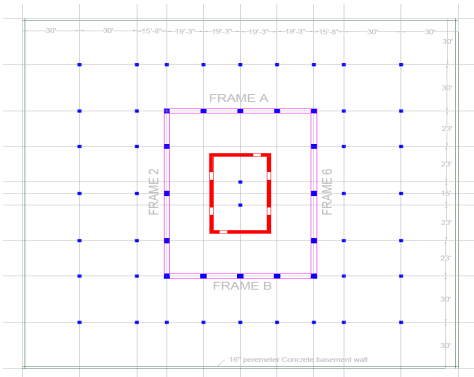


Figure 2. 42-story core wall special moment frame: 3D rendering of structure from PERFORM-3D model. Reprinted with permission.

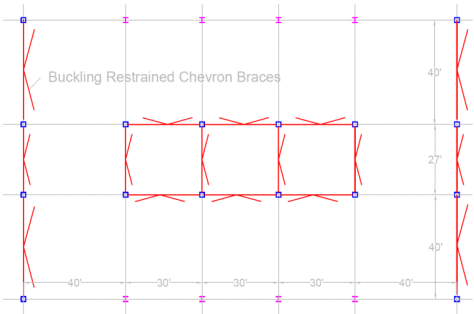


Figure 3. Typical plan view of the BRB building (above ground). Reprinted with Permission.

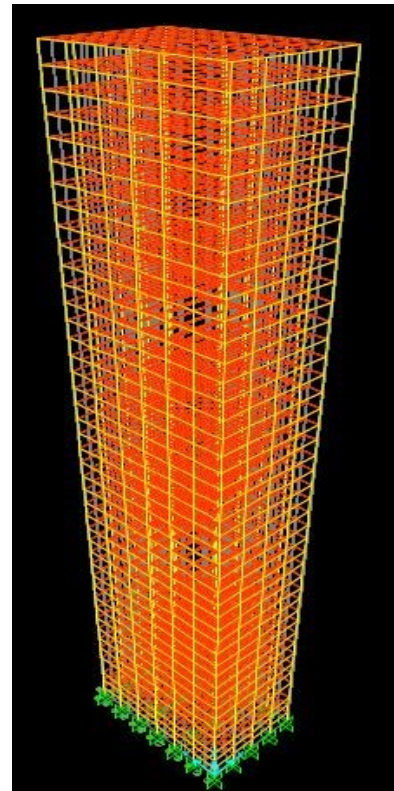


Figure 5. Three-dimensional rendering of the 40-story space-frame structure from the PERFORM-3D model.

## Ground Motions Used in this Study

### Spectral-Matching Ground Motions

All of the case study buildings were located in Los Angeles. Site-specific response spectra and a set of seven pairs of response spectrum-compatible ground motions were provided by a research team from the PEER Center at the University of California Berkeley (Mahin, Yang, & Bozorgnia, 2008). The same spectra and spectrum-compatible ground motions have been used by PEER's Tall Building Initiative for analyzing tall concrete buildings. Figure 6 shows the actual recorded earthquake time histories (listed in Table 1) that were used and modified in the frequency domain to match the target spectrum. These seven pairs of ground motions will be called "frequency modification" motions in this paper.

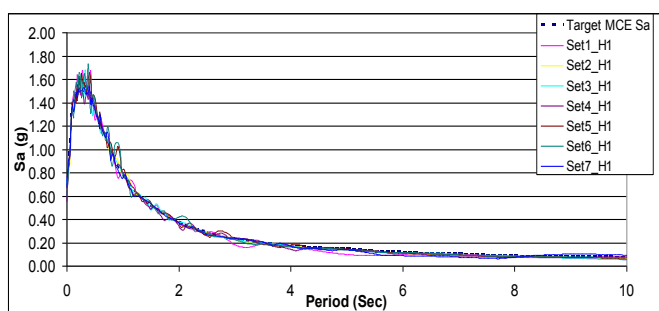


Figure 6. Site-specific response spectrum and seven pairs of spectrum-compatible ground motions.

### Time Domain-Scaled Ground Motions

Time-domain scaling requirements for 3D dynamic analyses are provided in Section 16.1.3.2 of ASCE 7-10. These requirements are provided verbatim as follows:

For each pair of horizontal ground motion components a square root of the sum of the squares (SRSS) spectrum shall be constructed by taking the SRSS of the 5% damped response spectra for the scaled components (where an identical scale factor is applied to both components of a pair). Each pair shall be scaled such that, for each period in the range from  $0.2T$  to  $1.5T$ , the average of the SRSS spectra from all horizontal component pairs does not fall below the corresponding ordinate of the design response spectrum, determined in accordance with Section 11.4.5 or 11.4.7.

The problem with the above requirements is that no guidance is provided on how to deal with different fundamental periods in the two orthogonal directions. There are an infinite number of sets of scale factors that will satisfy the criteria, so different engineers are likely to obtain different sets of scale factors for the same ground motions (Soules, 2013). In this current study, the author used the two-step scaling method followed in FEMA P-751 (National Institute of Building Sciences, 2012). First, scale each SRSS'd pair to the average period ( $T_{avg}$ ), as shown in Figure 7. This factor will be different for each of SRSS spectra, and is denoted by  $S_1$  in Table 1. Also,  $T_{avg}$  is the average of the fundamental periods in each principal direction. Second, the average of the scaled spectra will match the target spectrum at  $T_{avg}$ , as shown in Figure 8. Now, a second factor ( $S_2$  in Table 1) is applied equally to each motion (already scaled once) such that the scaled-average spectrum lies above the target spectrum from  $0.2T_{avg}$  to  $1.5T_{avg}$ .

The final scale factor for each motion is the product of the two scale factors. Detailed calculation steps were provided in Table 1 for the 40-story buckling restraint-braced frame structure. Figure 9 provides a comparison of target spectrum and the average SRSS spectrum of the seven pairs of motions after the scaling factor in Table 1 is applied to the motions. These seven pairs of ground motions will be called "amplitude scaling" motions in this paper.

Table 1. 40-story BRB scaling factor.

Record number	Earthquake Name	SRSS Ordinate at $T=T_{avg}$ (g)	Target Ordinate at $T=T_{avg}$ (g)	$S_1$	$S_2$	$SS = S_1 * S_2$
Set 1	Superstition Hills-02	0.159	0.143	0.90	1.3	1.166
Set 2	Denali, Alaska	0.063	0.143	2.26	1.3	2.942
Set 3	Northridge-01 (Converter Sta)	0.155	0.143	0.92	1.3	1.193
Set 4	Loma Prieta	0.099	0.143	1.44	1.3	1.877
Set 5	Northridge-01 (Olive View Med FF)	0.102	0.143	1.39	1.3	1.812
Set 6	Landers	0.116	0.143	1.23	1.3	1.598
Set 7	Kocaeli, Turkey	0.078	0.143	1.81	1.3	2.357

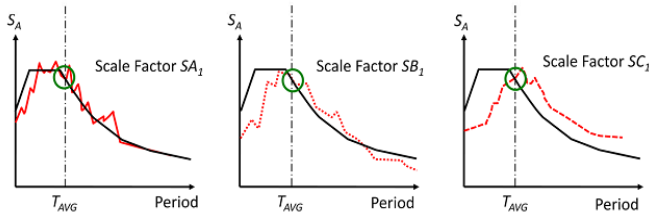


Figure 7. Step 1 of the time-domain scaling (Soules, 2013).

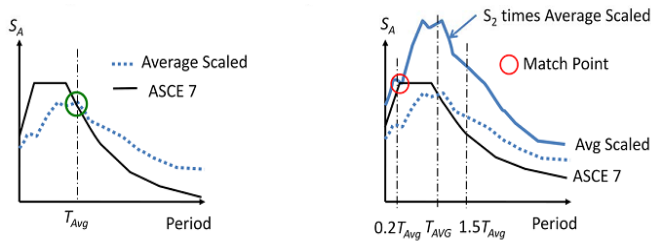


Figure 8. Step 2 of the time-domain scaling (Soules, 2013).

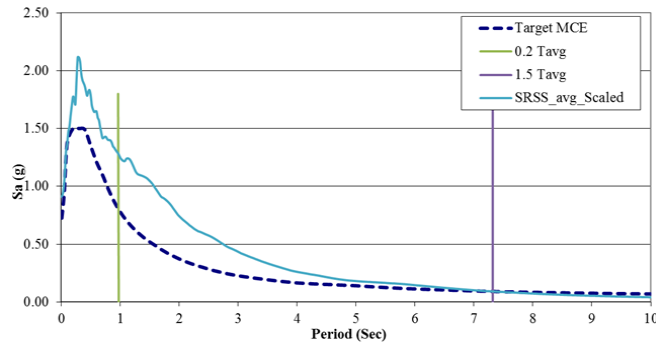
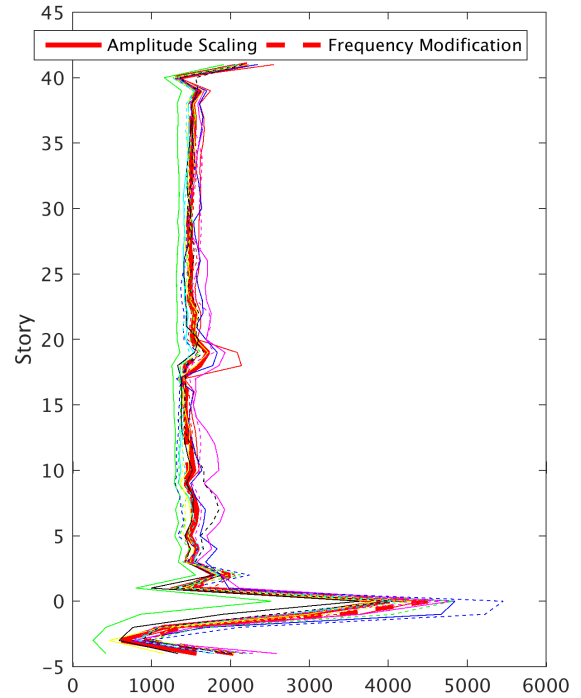


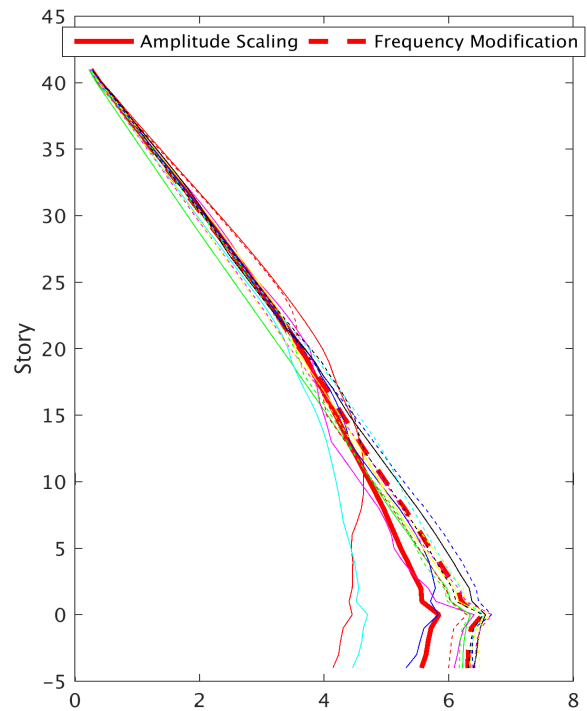
Figure 9. Average SRSS spectrum after the application of scale factors listed in Table 1 for the buckling restraint-braced frame structure.

## Results

As mentioned earlier, detailed three-dimensional non-linear models were developed in PERFORM-3D software for all of the three case study buildings. Each building was subjected to 14 pairs of ground motions—seven pairs from amplitude scaling and seven pairs from frequency modification. All of the figures contained in this section followed the same style: solid lines represents amplitude scaling individual earthquake motion responses, dotted lines represents frequency modification motion responses, and bold lines represents the average of the motions. For the most part, comparisons between amplitude scaling and frequency modification were done by comparing the average response lines. Figures 10-15 summarize the results for and provide comparisons between amplitude scaling and frequency modification for the 42-story dual-core wall-frame special-moment building.

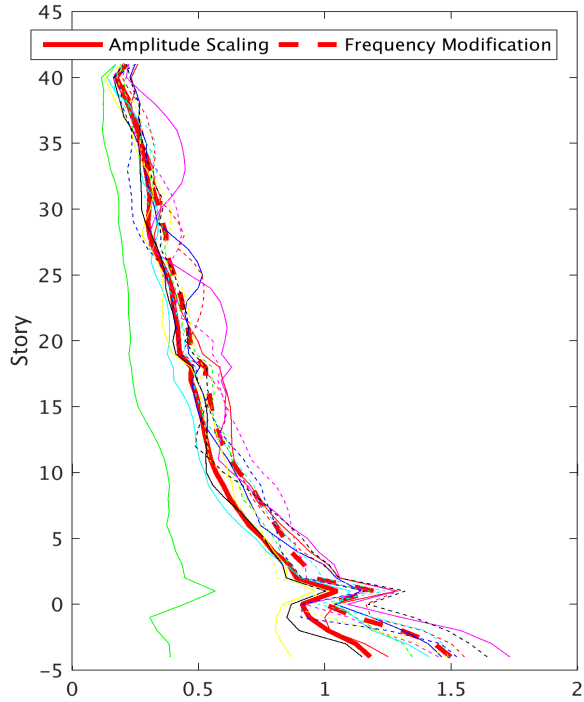


(a) Story shear (kip).

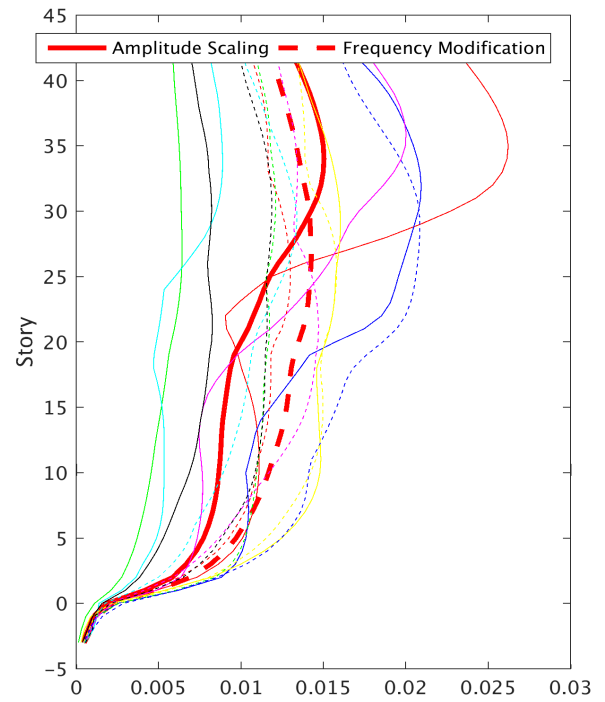


(b) Story moment ( $10^5$  kip-ft.).

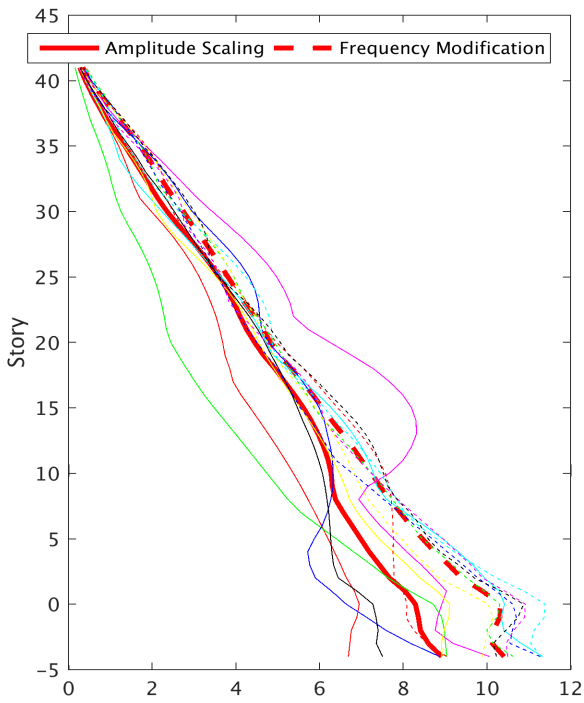
Figure 10. Comparison of forces: Moment frame. Solid lines for amplitude scaling; dotted lines for frequency modification; and, bold lines for average response.



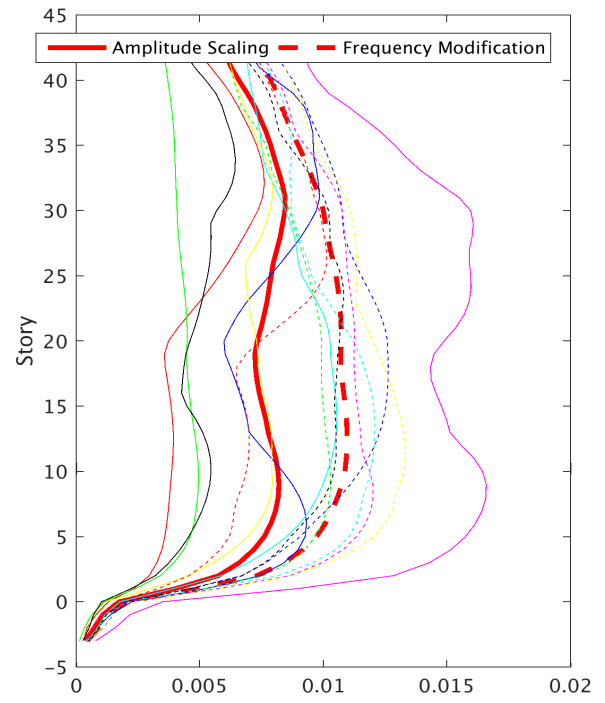
(a) Story shear ( $10^4$  kip).



(a) EW inter-story drift.



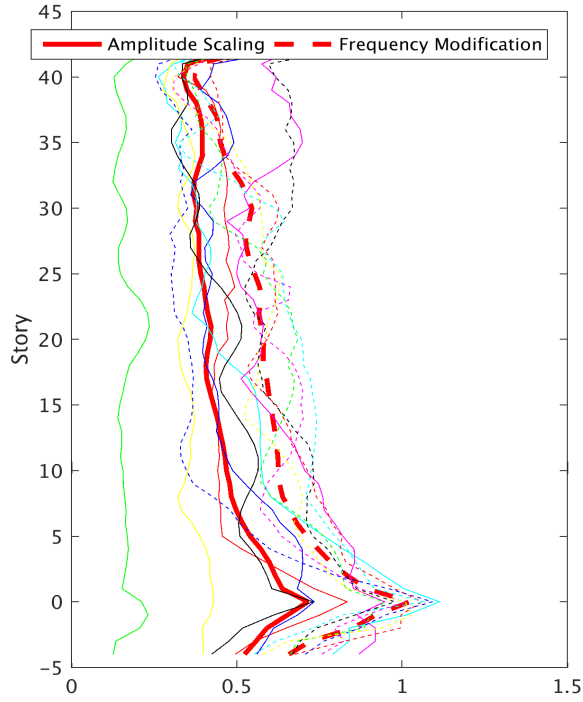
(b) Story moment ( $10^5$  kip-ft.).



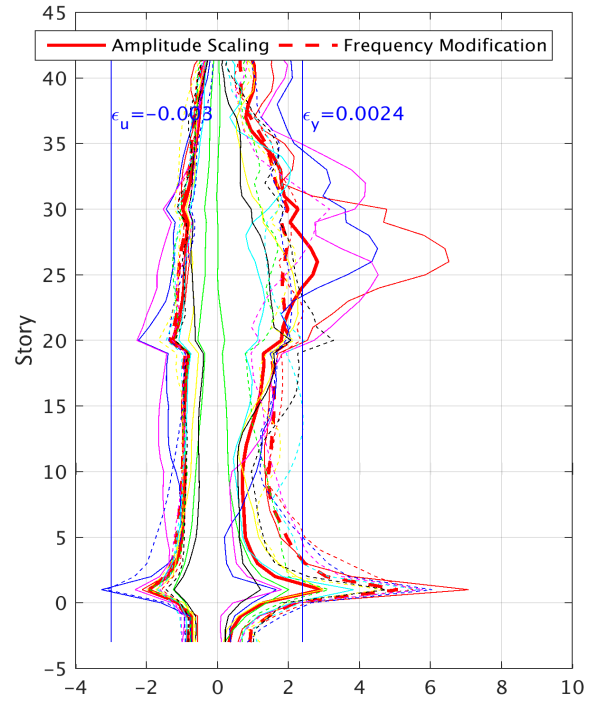
(b) NS inter-story drift.

Figure 11. Comparison of forces: Core wall. Solid lines for amplitude scaling; dotted lines for frequency modification; and, bold lines for average response.

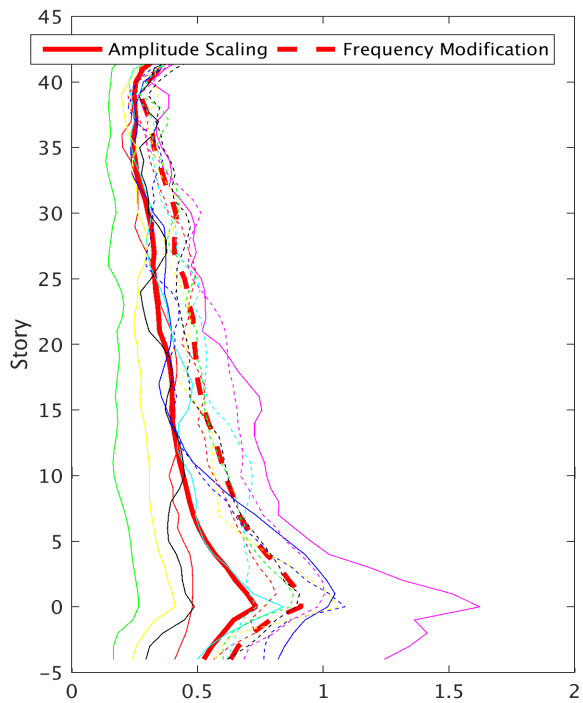
Figure 12. Comparison of inter-story drift. Solid lines for amplitude scaling; dotted lines for frequency modification; and, bold lines for average response.



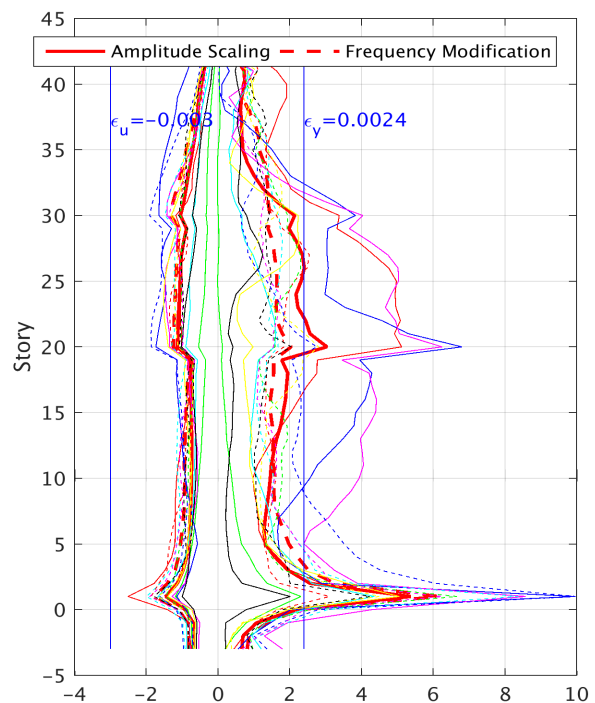
(a) EW floor acceleration (g).



(a) Strain ( $10^{-3}$ ): Pier 2 (P2) location.



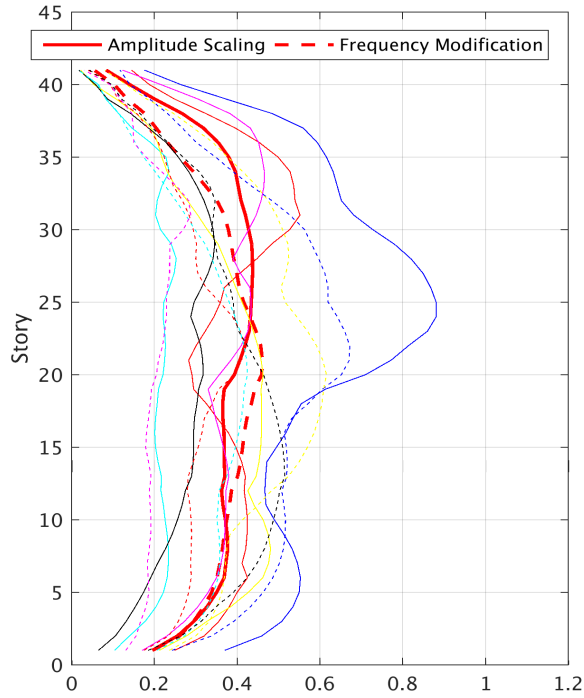
(b) NS floor acceleration (g).



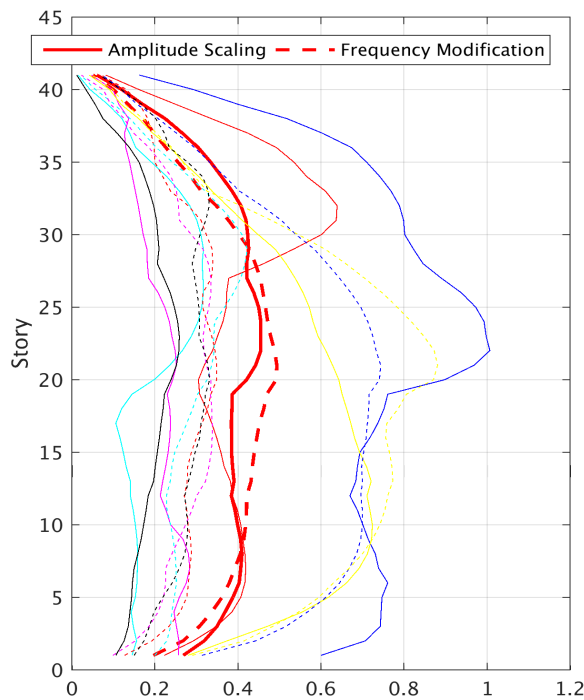
(b) Strain ( $10^{-3}$ ): Pier 10 (P10) location.

Figure 13. Comparison of floor acceleration. Solid lines for amplitude scaling; dotted lines for frequency modification; and, bold lines for average response.

Figure 14. Comparison of axial strain in core wall. Solid lines for amplitude scaling; dotted lines for frequency modification; and, bold lines for average response.



(a) Coupling beam rotation between P3 and P2 (DCR).



(b) Coupling beam rotation between P11 and P10 (DCR).

Figure 15. Comparison of coupling beam (CB) rotation. Solid lines for amplitude scaling; dotted lines for frequency modification; and, bold lines for average response.

Figures 10 and 11 compare the results of story shear and story moment for moment frame and core wall, respectively. Figure 11 shows that higher demands were exhibited by frequency modification motion for story shear and story moment compared to amplitude scaling.

Figures 12 and 13 show that significantly higher levels of responses were observed for inter-story drift and floor acceleration for frequency modification motion. Thus, if acceleration-sensitive equipment is to be placed in the building, it would be wiser to use amplitude scaling motion to evaluate the building's performance.

Figure 14 and 15 show the results of axial strain in core wall and coupling-beam rotation, respectively. As can be seen, differences were not significant; at some story levels, frequency modification showed higher responses, while at other story levels amplitude scaling showed higher responses.

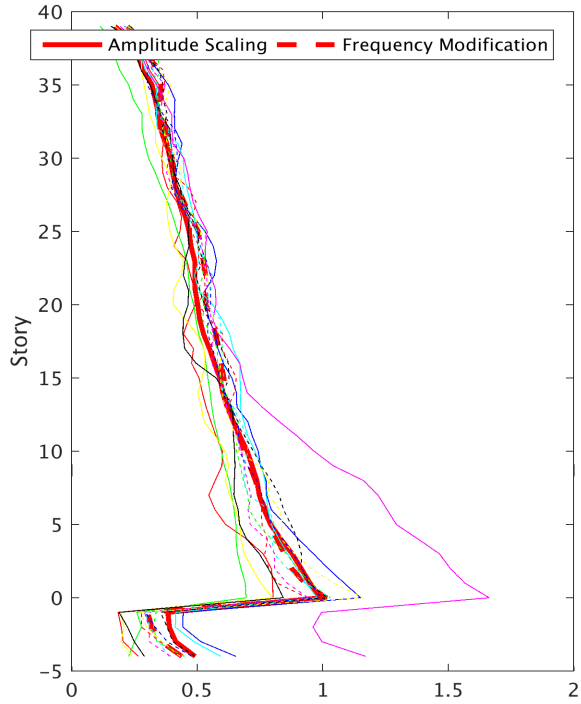
Figures 16 to 18 summarize the results for and comparisons between amplitude scaling and frequency modification for the 40-story buckling-restraint-braced (BRB) frame structure. Figure 16 shows the results of story shear and story moment. Higher demands were exhibited by frequency modification motion for story moment, as can be seen in Figure 16(b).

Figure 17 shows that inter-story drift did not make a significant difference; at some story levels, frequency modification showed higher responses, while at some other story levels amplitude scaling showed higher responses.

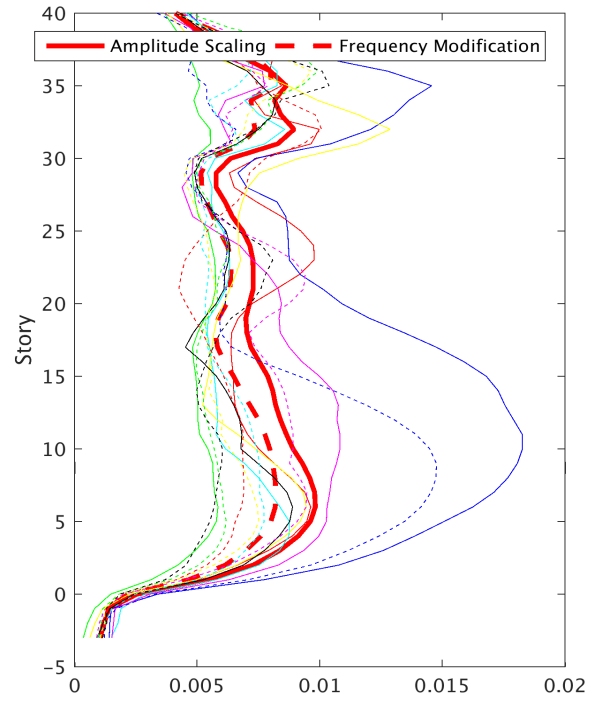
Figure 18 shows that significantly higher responses were observed for floor acceleration for frequency modification motions. Again, if acceleration-sensitive equipment is to be placed in the building, it would be wiser to use amplitude scaling motion to evaluate the building's performance.

Figures 19 and 20 compare the results of story shear, story moment, and inter-story drift for the 40-story steel space-frame structure. The figures do not show any significant differences.

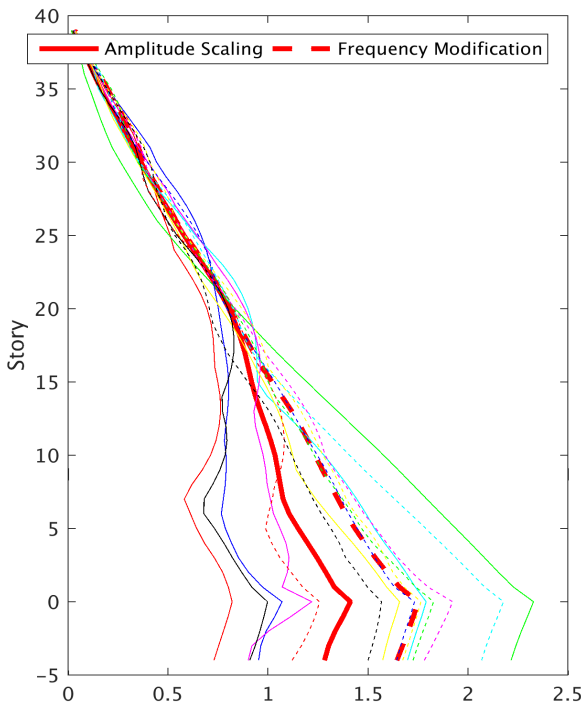
However, Figure 21 shows that much higher responses were observed for floor acceleration for frequency modification motion. Once again, if acceleration-sensitive equipment were to be placed in the building, it would be wiser to use amplitude scaling motion to evaluate the building's performance.



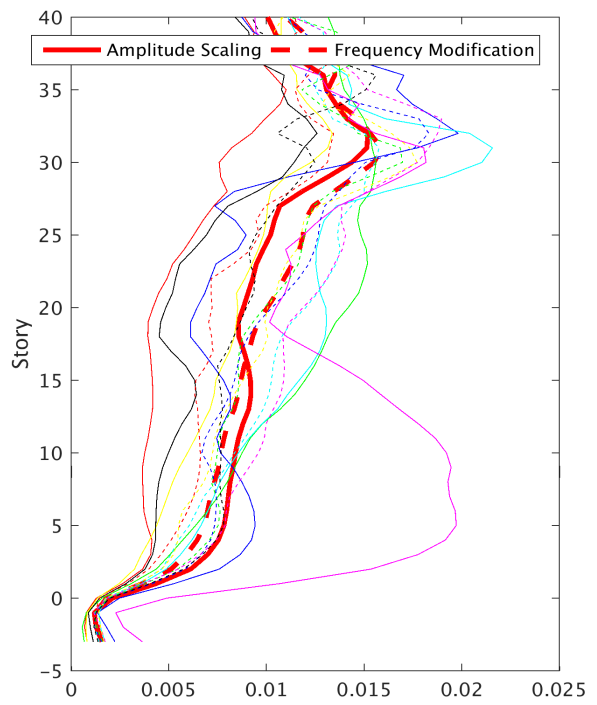
(a) Story shear ( $10^4$  kip).



(a) EW inter-story drift.



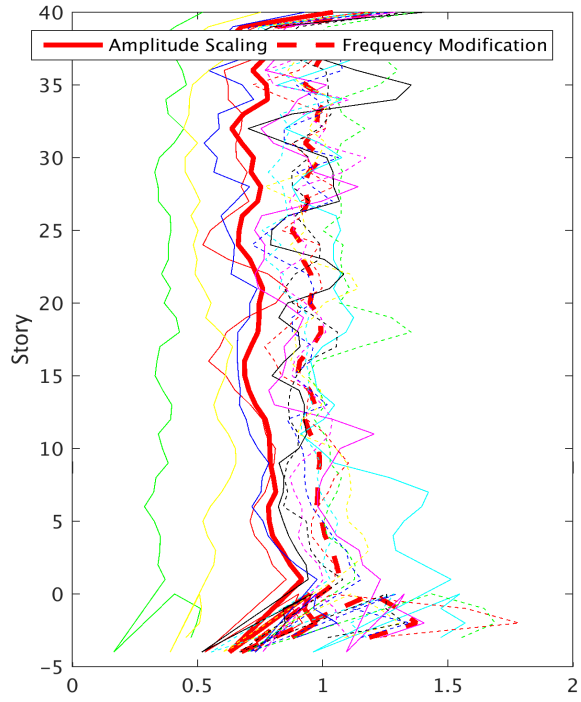
(b) Story moment ( $10^6$  kip-ft.).



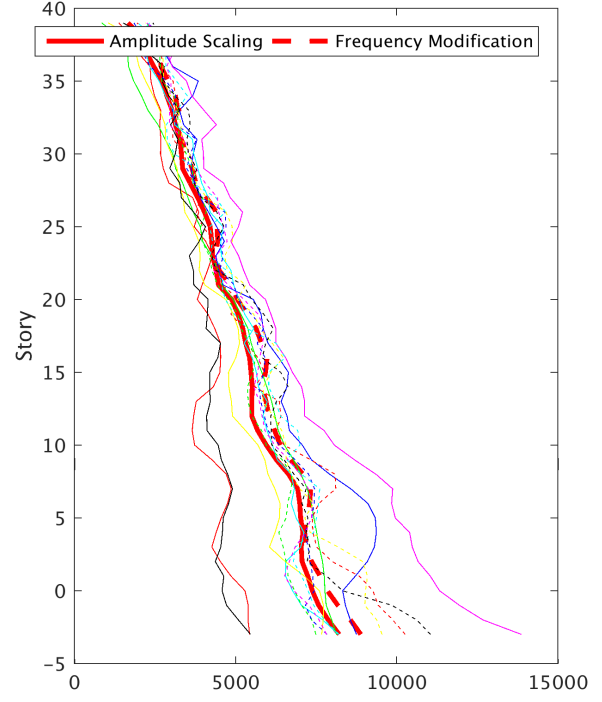
(b) NS inter-story drift.

Figure 16. Comparison of forces. Solid lines for amplitude scaling; dotted lines for frequency modification; and, bold lines for average of response.

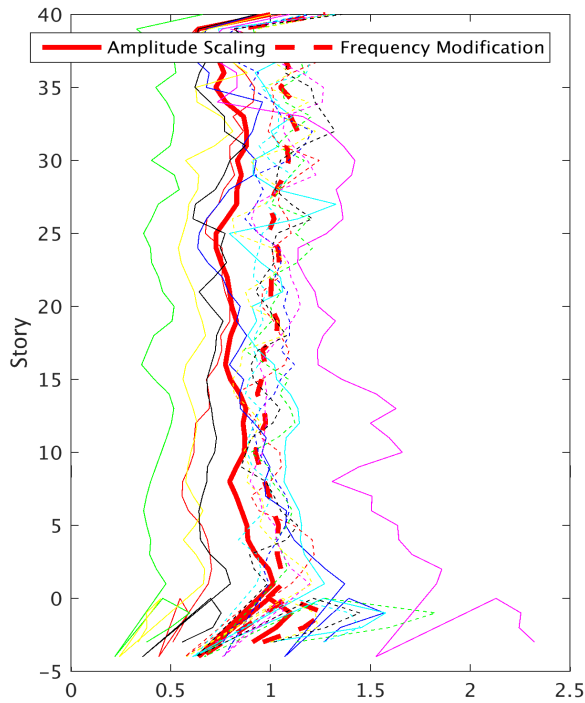
Figure 17. Comparison of inter-story drift. Solid lines for amplitude scaling; dotted lines for frequency modification; and, bold lines for average of response.



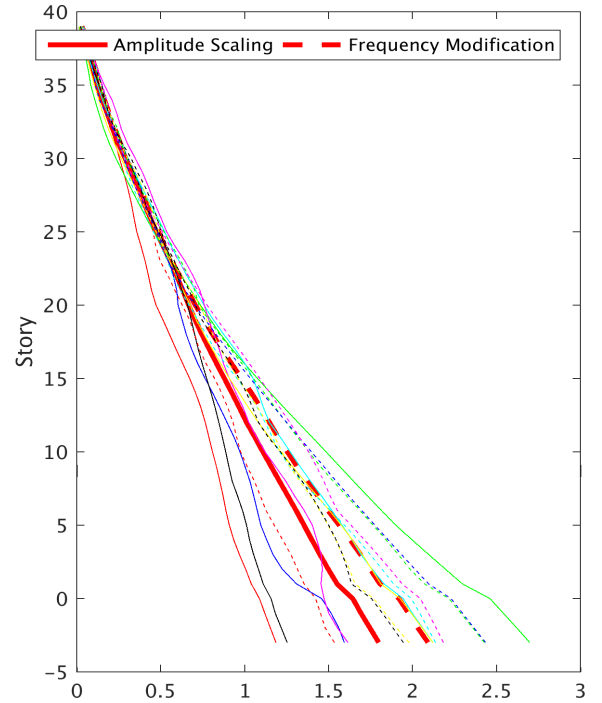
(a) EW floor acceleration (g).



(a) Story shear (kip).



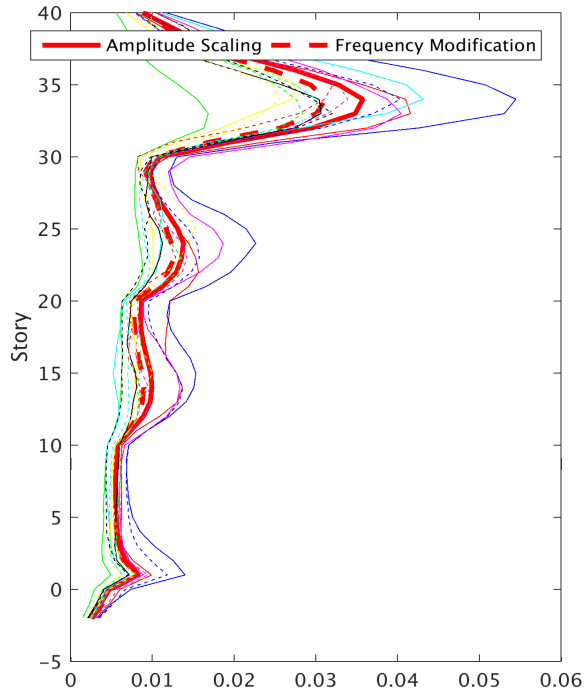
(b) NS floor acceleration (g).



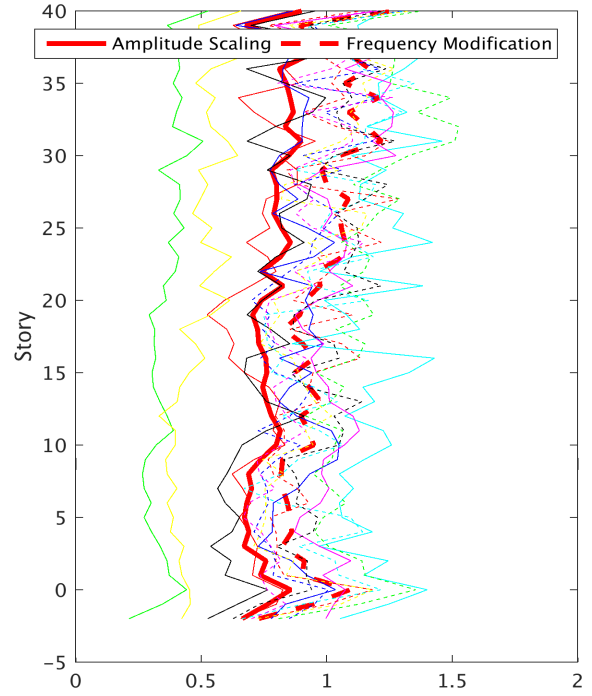
(b) Story moment ( $10^6$  kip-ft.).

Figure 18. Comparison of floor acceleration. Solid lines for amplitude scaling; dotted lines for frequency modification; and, bold lines for average response.

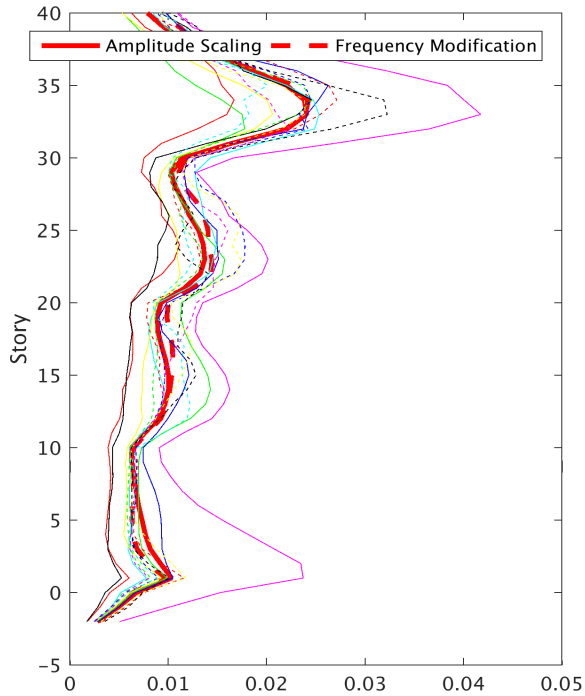
Figure 19. Comparison of forces. Solid lines for amplitude scaling; dotted lines for frequency modification; and, bold lines for average response.



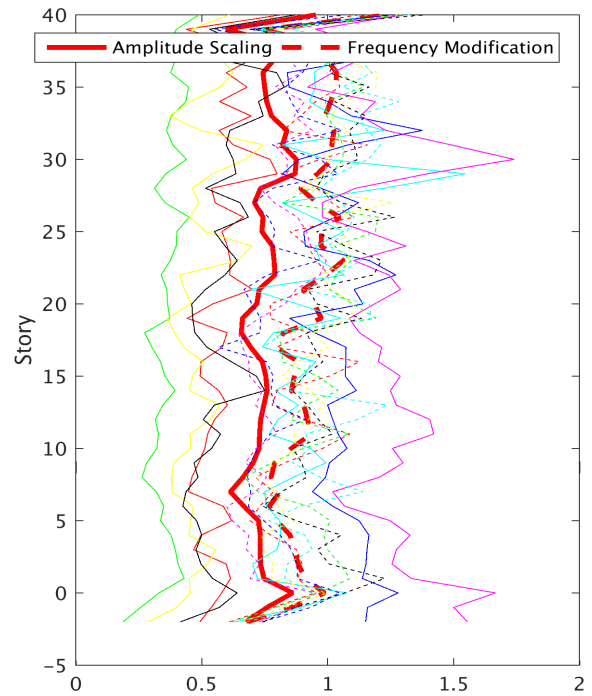
(a) EW inter-story drift.



(a) EW floor acceleration (g).



(b) NS inter-story drift.



(b) NS floor acceleration (g).

Figure 20. Comparison of inter-story drift. Solid lines for amplitude scaling; dotted lines for frequency modification; and, bold lines for average response.

Figure 21. Comparison of floor acceleration. Solid lines for amplitude scaling; dotted lines for frequency modification; and, bold lines for average response.

---

## Conclusions

Three case study buildings were analyzed with seven pairs of amplitude-scaled and seven pairs of spectral-matching ground motions. Comparisons showed that, in general, use of spectral-matching ground motions yielded higher demand. But, use of time domain-scaled ground motions provided comparable structural design of a high-rise building. When spectral-matching ground motions were used, significantly higher floor accelerations were observed. Therefore, if acceleration-sensitive equipment were placed in a high-rise building, it would be advisable to use amplitude-scaled ground motions to evaluate the building's performance.

Comparisons of story shear and story moment indicated higher demand, for all three buildings, from spectral-matching ground motions. Higher demand on inter-story drift was observed for the 42-story dual-core wall-frame building with spectral match motions, but amplitude-scaling motions yielded higher demands for the other two structures. Coupling beams rotations for the 42-story dual-core wall-frame structure were similar for both types of input motions. This study only used three case study structures; one concrete and two steel buildings with similar height, and one single location (Los Angeles). For future studies, the author recommends including more case study structures with different heights, floor plans, structural types, and locations.

## References

- ASCE. (2011). *ASCE 7-10, Minimum design loads for buildings and other structures*. Reston, VA: American Society of Civil Engineers.
- Hutt, C. M. (2013). Non-linear time history analysis of tall steel moment frame buildings in LS-DYNA. *Proceedings of the 9th European LS-DYNA Conference*. Salt Lake City, UT: ARUP.
- Mahin, S., Yang, T., & Bozorgnia, Y. (2008). Personal communication.
- Moehle, J., Bozorgnia, Y., Jayaram, N., Jones, P., Rahnama, M., Shome, N., Tuna, Z. ..., & Zareian, F. (2011, July). *Case studies of the seismic performance of tall buildings designed by alternative means. Task 12: Report for the tall buildings initiative*. Berkeley, CA: Pacific Earthquake Engineering Research Center.
- National Institute of Building Sciences. (2012, September). *2009 NEHRP recommended seismic provisions: Design examples*. Retrieved from [https://www.fema.gov/media-library-data/1393877415270-d563663961c9f40e88ce3ad673377362/FEMA\\_P-751.pdf](https://www.fema.gov/media-library-data/1393877415270-d563663961c9f40e88ce3ad673377362/FEMA_P-751.pdf)
- PERFORM 3D. (2011). *Nonlinear analysis and performance assessment of 3D structures*. Walnut, CA: Computers and Structures, Inc.
- Soules, J. G. (2013, June). *Instructional material complementing FEMA P-751, Design examples*. Retrieved from [https://www.fema.gov/media-library-data/1393890432586-c071850c3050c34da135376baa478a1b/P-752\\_Unit13.pdf](https://www.fema.gov/media-library-data/1393890432586-c071850c3050c34da135376baa478a1b/P-752_Unit13.pdf)

## Biography

**MOHAMMAD T. BHUIYAN** is an assistant professor of civil engineering at West Virginia State University. He earned his BSc in Civil Engineering from Bangladesh University of Engineering and Technology, Dhaka; an MSc in Earthquake Engineering jointly from Universite Joseph Fourier, France, and ROSE School, Italy; and PhD in Earthquake Engineering from ROSE School with joint programs at Georgia Tech. His research interests include tall buildings, earthquake engineering, and soil-structure interaction. Dr. Bhuiyan may be reached at [towhid@wvstateu.edu](mailto:towhid@wvstateu.edu)

# DESIGN AND TEST OF A HIGH-SPEED ACTUATOR FOR GAS MIXING AND FLOW-CONTROL APPLICATIONS

Todd D. Batzel, Pennsylvania State University, Altoona College;  
Christopher R. Martin, Pennsylvania State University, Altoona College;  
Dimitris W. Kiaoulas, Pennsylvania State University, Altoona College;  
Matthew J. Cowler, Pennsylvania State University, Altoona College

## Abstract

In this paper, the authors describe the design, prototyping, and testing of an actuator to be used as a high-speed valve for gas mixing. The function of the actuator is to rapidly switch the flow of gas on and off using pulse width modulation (PWM). Successful implementation of this actuator will allow gas flow regulation without the need for sensor feedback. In the application, the actuator's PWM frequency must be sufficiently high so that pressure ripple is minimal downstream of the valve, and the actuator opening and closing times must be fast relative to the PWM period. Furthermore, the actuator must develop sufficient force to overcome high pressures opposing the opening of the valve. These restrictions imply that some combination of a lightweight operator and a high actuator force are requirements of the design. For this reason, a permanent magnet voice coil arrangement is a leading candidate for the actuator topology.

The electromagnetic actuator design was initially performed using magnetic equivalent circuit analysis and then confirmed by more precise finite element analysis (FEA) computations. The design yielded actuator parameters such as actuator force per unit current, coil inductance, coil resistance, and magnetic flux densities at various locations in the flux path. These parameters were sufficient to allow an estimation of valve switching characteristics. The prototyping and assembly of the actuator is described here. Finally, the gas mixing system's overall performance was tested to validate the effectiveness of the actuator design.

## Introduction

In this paper, the authors present the design, implementation, and test results of an actuator to be operated in a high-speed digital valve for gas mixing applications. The proposed high-speed actuator is a critical component of a novel digital control system for mixing multiple gases without the need for feedback measurements (Martin & Batzel, 2018). In this application, the actuator must rapidly switch the flow of a pressured gas fully on and off at frequencies of at least 50 Hz to minimize ripple in the downstream gas pressure.

In the study, major design factors such as the physical dimensions and the static and dynamic operating requirements were first analyzed so that an appropriate actuator topology could be selected. With the actuator topology identified and static and dynamic force requirements established, the magnetic circuit components, geometry, and materials were initially analyzed using magnetic equivalent circuits. Airgap, permanent magnet, steel yoke dimensions, and magnetic characteristics were used to compute the airgap magnetic flux density. The computed airgap flux density was then used to determine the number of voice coil turns as well as the conductor size required to match the coil to the desired operating voltage. The developed actuator force was computed as well as the electrical time constant of the voice coil. The actuator design was then verified with a more accurate FEA. The construction of the actuator prototype and its integration into the valve assembly will also be presented. Laboratory tests were performed in order to confirm the force production capability of the actuator. Finally, dynamic testing of the prototype assembly as a digital valve was performed to verify the suitability of the actuator in its intended application.

## Actuator Requirements and Constraints

The first step in the actuator design was to identify the requirements, which, coupled with the geometric constraints, would allow selection of the actuator topology. Using this topology, the magnetic and electric loading points could be selected, and electromagnetic computation and analysis performed. This process was iterated as necessary until a satisfactory solution was obtained. Actuator requirements included both static and dynamic force production capability. The actuator had to be able to provide enough static force ( $F_{stat}$ ) to overcome that of the gas pressure. This static force was the product of the gas pressure  $P_{gas}$  and effective cross-sectional area of the valve seat  $A_o$ . Figure 1 shows the nozzle dimensions used to obtain an effective valve seat area. Using a maximum delivery gas pressure of 125 psi yielded a required actuator static force ( $F_{stat}$ ) of 6.8N. During operation, the full 125 psi was not typically across the valve, so this static force computation represented a worst-case analysis.

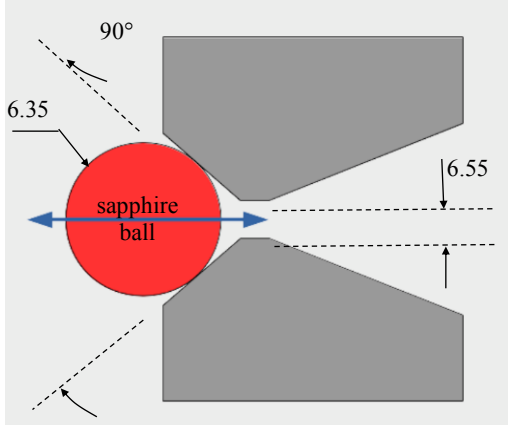


Figure 1. Valve seat (dimensions in mm).

The actuator also had to be capable of opening and closing the valve in 2ms. During valve opening, the actuator had to overcome the static force ( $F_{stat}$ ) as well as provide the required dynamic accelerating force ( $F_{acc}$ ). Figure 2 shows the dynamic motion profile for the valve operator. The maximum stroke length was limited by an adjustment screw nominally set to limit motion to 0.4 mm. The dynamic accelerating force is the product of the operator mass and the required acceleration. Initially assuming a total operator mass of 0.03 kg, a dynamic force of 6N was required. In this case, the actuator had to provide a maximum force of 12.8N to open the valve, where the operator must initially overcome the static force as well as provide the accelerating force. The static force, however, vanishes as the valve opens, so that closing the valve only requires the accelerating force. Clearly, keeping the mass of the operator low is critical in keeping the dynamic forces to an achievable level. This constraint led to the selection of a voice-coil-type actuator topology.

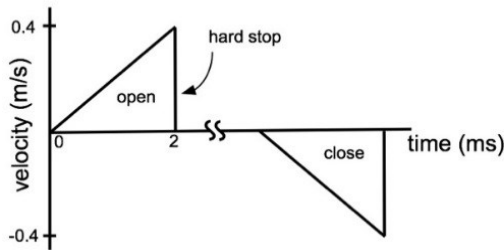


Figure 2. Motion profile of the operator.

## Voice Coil Actuator

Voice coil topology is ideal in applications that require high-frequency operation or fast acceleration, because of its fast electrical and mechanical time constants (Sung & Kim, 2018; Roemer, Bech, Johansen, & Pedersen, 2015). A voice

-coil-type actuator (VCA) uses a permanent magnet, whose field interacts with a coil winding current to produce a force that is proportional to the applied coil current, and generally yields a linear force per unit current characteristic. The direction of the force can be reversed in a voice coil by reversing the direction of the coil current. The developed actuator force can be estimated using Equation 1:

$$F_{act} = Bli \quad (1)$$

where,  $F_{act}$  is the force in Newtons;  $B$  is the magnetic flux density perpendicular to the current;  $l$  is the total length of the wire (the product of the number of turns,  $N$ , and the circumference of the coil); and,  $i$  is the current in the coil.

A voltage  $e$  is also induced in the coil when it is in motion, as given by Equation 2:

$$e = Blu \quad (2)$$

where,  $u$  is the velocity of the coil relative to the magnetic field.

## Design of Voice Coil Actuator

A good starting point in sizing a voice coil actuator is to select an appropriate shear stress target. Air gap shear stress ( $\tau$ ) is often used in electric machine design as a sizing metric, since it is generally similar even for different sizes of machines of the same topology (Beaty & Kirtley, 1998; Batzel, Skraba & Massi, 2014). For the voice coil actuator, shear stress is a measure of the actuator force per unit surface area of the airgap. As a point of reference, common permanent magnet motor designs without special provisions for forced cooling have an airgap shear stress in the range from 3.5 to 14 kPa (Hanselman, 2006). For the permanent magnet actuator design in this study, an airgap shear stress in that same range was selected—10 kPa. The airgap shear stress is represented by Equation 3:

$$\tau = \frac{F_{act}}{A_g} \quad (3)$$

where,  $A_g$  is the airgap surface area, where the coil current interacts with the permanent magnet field.

Using Equation 1 and assuming that the airgap is cylindrical with a radius  $r$  and a height  $h$ , the airgap shear stress can be written as Equation 4:

$$\tau = \frac{Bli}{2\pi rh} = \frac{B(2\pi r)i}{2\pi rh} = BZ \quad (4)$$

where, the linear current density  $Z$  (A/m) is representative of the electrical loading and the flux density  $B$  is the magnetic loading of the actuator.

To achieve the target airgap shear stress of 10 kPa, a magnetic loading  $B$  of 0.4 Tesla was selected. This is a reasonable magnetic loading that is achievable for neodymium type (NdFeB) permanent magnets operating near their point of maximum energy product. To get maximum flux density per unit volume of permanent magnet material, the permanent magnet should be operated near this point of maximum energy product (Boldea & Nasar, 2005). Also, from Equation 4, the target shear stress and magnetic loading parameters will require an electrical loading of 25,000 A/m. The coil dimensions and airgap length could now be computed using the active airgap area  $A_g$ , the linear current sheet density  $Z$ , and a conductor current density  $J$ . Using Equation 3 and an actuator force of  $F_{act} = 15\text{N}$  to provide headroom beyond the required maximum torque of 12.8N, the active airgap area required to achieve the targeted airgap shear stress is  $1.5 \times 10^{-3} \text{m}^2$ . From Figure 3, the active airgap area can be given by Equation 5:

$$A_g = 2\pi rh \quad (5)$$

To achieve the required airgap area  $A_g$ , the coil radius  $r$  was selected to be 0.019m ( $3/4$  in), and the coil height  $h$  was 0.0127m ( $1/2$  in). This choice of dimensions was made in part to keep the overall actuator profile comparable with that of typical gas metering valves.

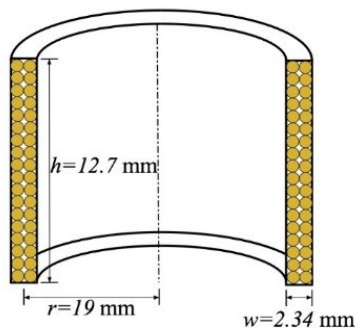


Figure 3. Actuator coil dimensions.

To estimate the coil width  $w$ , shown in Figure 3, a conductor current density  $J$  of  $15 \text{ A/mm}^2$  was selected. This current density is similar to that commonly used in actuators (Yatchev, Hinov, Balabozov, & Krasteva, 2011) and should not result in excessive temperature rise (Soong, 2016) in this application. Considering the copper fill factor  $\sigma$  of the coil, which was estimated to be 0.71 for a multi-layer packed coil, where the insulation added an extra 10% to the conductor's diameter (MS Wire, 2014), the width of the coil can be determined using Equation 6:

$$w = \frac{Z}{J\sigma} \quad (6)$$

This results in a required coil width of 2.34 mm. A clearance of 0.42 mm on each side of the coil gives a total airgap length of 3.18 mm ( $1/8$  in). Using the current density of  $15 \text{ A/mm}^2$ , a 24-gauge wire (0.51 mm diameter), for example, can carry 3.1  $\text{A}_{\text{rms}}$  of current.

## Magnetic Equivalent Circuit Analysis of VCA

Given the computed airgap and coil dimensions from the previous section, a magnetic equivalent circuit (MEC) analysis was then performed to identify dimensions for the permanent magnet and iron yoke. Magnetic equivalent circuit analysis allows for rapid computation of the actuator operational parameters so that the design can be quickly iterated as necessary until satisfactory characteristics are achieved. There are many options for the selection and placement of the VCA permanent magnet. Although an axially magnetized cylindrical permanent magnet in the inner yoke and a radially magnetized ring magnet located at the airgap were considered, the axially magnetized ring magnet type shown in Figure 4 was ultimately selected. This choice was made, because it simplifies assembly and was available off-the-shelf in a variety of dimensions. Figure 4 illustrates the selected voice coil actuator topology, where the airgap and coil dimensions were determined in the previous section, and the magnet dimensions shown were obtained after many iterations of magnetic equivalent circuit analysis.

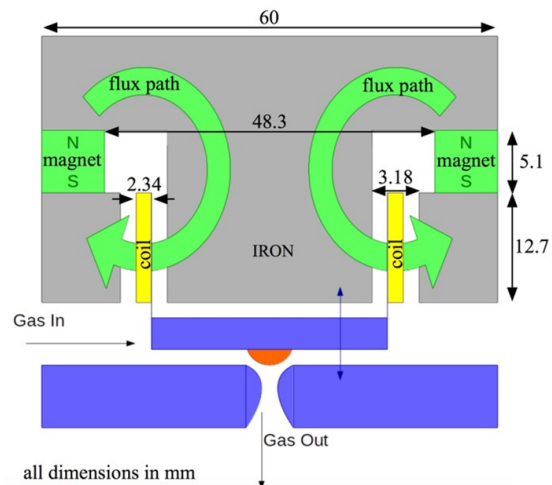


Figure 4. Voice coil actuator sketch.

Using the simplifying assumption that the iron yoke permeability is infinite, the sum of magneto-motive force around any of the flux paths shown in Figure 4 can be determined using Equation 7:

$$H_g = -\frac{l_m}{l_g} H_m \quad (7)$$

where,  $l_m$  and  $l_g$  are the lengths of magnetic flux path in the magnet and airgap, respectively; the field intensity in the magnet and airgap are represented by  $H_m$  and  $H_g$ , respectively; and, the flux density  $B$  in the airgap is  $B_g = \mu_0 H_g$ , where  $\mu_0$  is the magnetic permeability of free space.

Since the magnetic flux  $\phi$  is continuous in the paths shown in Figure 4, it can be determined using Equation 8:

$$\phi = A_m B_m = A_g B_g \quad (8)$$

where,  $A$  is the cross-sectional area in which magnetic flux flows in the magnet and airgap and  $B_m$  is the flux density in the permanent magnet.

Equation 8 then becomes Equation 9:

$$B_g = \frac{A_m}{A_g} B_m \quad (9)$$

Equations 7 and 9 then yield Equation 10:

$$B_m = -\mu_0 \left( \frac{A_g}{A_m} \right) \left( \frac{l_m}{l_g} \right) H_m \quad (10)$$

The intersection of Equation 10 and the load line of the magnet B-H characteristic curve defines the operating point of the permanent magnet. In the case of NdFeB (grade 40) magnets, which are linear in the 2nd quadrant of the B-H curve, the B-H normal curve at 60 degrees Celcius is represented by Equation 11:

$$B_m = 1.09 \mu_0 H_m + 1.2 \quad (11)$$

The solution of Equations 10 and 11, using the gap dimensions computed previously ( $A_g = 1.5 \times 10^{-3} \text{m}^2$  and  $l_g = 0.00318 \text{m}$ ), can be used to determine suitable magnet dimensions. After several iterations, the magnet dimensions given in Table 1 were selected.

Table 1. Ring magnet dimensions.

Parameter	Value
Outer Radius	29.97 mm
Inner Radius	24.13 mm
Material	NdFeB Grade 40
$A_m$	$9.926 \times 10^{-4} \text{m}^2$
$l_m$	0.00508 mm

Using the airgap dimensions determined previously ( $A_g = 1.5 \times 10^{-3} \text{m}^2$  and  $l_g = 0.00318 \text{m}$ ), Equations 10 and 11 can be solved to obtain practicable magnet dimensions. After multiple iterations of this magnetic analysis, a magnet of the dimensions given in Table 1 was selected. The dimensions were selected in part based on off-the-shelf availability of the magnet. For the selected magnet, Equations 10 and 11 yield an operating point of  $B_m = 0.82 \text{T}$  and an airgap magnetic flux density of  $B_g = 0.54 \text{T}$ . This resulting airgap flux density was well above the target magnetic loading of  $0.4 \text{T}$ . It should also be noted that the MEC analysis, though it provided a very quick iterative solution for the magnetic circuit dimensions, ignores flux leakage paths and the iron's finite permeability. Despite the known limitations of MEC, it served as a starting point for an FEA solution that would yield more accurate results.

## Coil Design and Parameters

The target electrical loading of  $Z = 25,000 \text{ A/m}$  and the coil dimensions shown in Figure 3 were used to specify the coil construction and compute its electrical characteristics. The number of ampere-turns,  $\mathcal{F}$ , required of the coil is given by Equation 12:

$$\mathcal{F} = Zh = 317.5 A - T \quad (12)$$

This result suggests that the coil could be constructed with  $N$  turns of conductor designed to carry  $317.5/N$  amperes of current. The trade-off is clearly that of coil current and induced voltage in the coil. Since it is standard for gas metering valves, 24 VDC was selected as the supply voltage for this application. The voltage induced in the moving voice coil, therefore, should be below the supply voltage of 24V by a large enough margin so that the current control can rapidly reverse or change the actuator coil current. The voltage induced in the moving voice coil can be computed using Equation 13:

$$e_{coil} = \frac{d \lambda_{coil}}{dt} \quad (13)$$

where,  $\lambda_{coil}$  is the magnetic flux linking the coil.

The maximum flux linking the coil in the neutral position (see Figure 4) will be  $0.5NB_g A_g = N(4.1 \times 10^{-4})$  webers. Using a slightly overstated stroke length of 1 mm, an overall coil height of 12.7 mm, and neglecting flux fringing as an approximation, the flux linkage was reduced to approximately  $N(3.47 \times 10^{-4})$  webers as coil turns move outside of the airgap (refer to the bottom of Figure 4) and flux flowing near the top of the gap no longer link any turns. If the stroke occurs in 2 ms, the approximate induced coil voltage during the motion can be determined by Equation 14:

$$e_{coil} = \frac{.N (.63 \times 10^{-4} W)}{.002 s} = .032 N V \quad (14)$$

Using Equation 14, a coil with  $N=100$  turns was selected for the design. With 100 turns, the induced coil voltage during voice coil motion would have a peak value of 3.2V, which provides ample voltage headroom for a current controller operating with a 24 VDC supply. To fit 100 conductor turns into the coil dimensions shown in Figure 3, 24-gauge magnet wire with a conductor area of  $A_{wire} = 0.205 \text{ mm}^2$  was selected. For the estimated copper fill factor of 71% and the available cross-sectional area for the conductors of  $29.7 \text{ mm}^2$ , 100 24-gauge conductors would fit into the designated coil cross-section. The resistance of the coil was computed using Equation 15:

$$R_{coil} = \frac{\rho l_{coil}}{A_{wire}} = \frac{(1.68 \times 10^{-8} \Omega \cdot \text{m})(2\pi)(.019 \text{ m})(100)}{.205 \times 10^{-6} \text{ m}^2} = 1 \Omega \quad (15)$$

where,  $\rho$  was the conductivity of copper, and  $l_{coil}$  was the total length of wire in the coil. Similarly, the coil inductance could be computed using Equation 16:

$$L_{coil} = \frac{N^2}{(\mathcal{R}_g + \mathcal{R}_m)} \quad (16)$$

where,  $\mathcal{R}_g$  and  $\mathcal{R}_m$  represent the magnetic reluctance of the airgap and magnet. The reluctances can be determined using Equation 17

$$\mathcal{R}_g = \frac{l_g}{\mu_0 A_g} = 1.69 \times 10^6 H^{-1} \quad (17)$$

and

$$\mathcal{R}_m = \frac{l_m}{1.09 \mu_0 A_m} = 3.74 \times 10^6 H^{-1}$$

giving a coil inductance  $L_{coil} = 1.84 \text{ mH}$ . Finally, the electrical time constant of the coil was determined using Equation 18:

$$\tau = \frac{L_{coil}}{R_{coil}} \quad (18)$$

which was found to be 1.84 ms. Given the considerable voltage headroom, the 24 VDC supply can drive the coil current to rated values in fraction of the electrical time constant. Therefore, the electrical time constant was not expected to limit the dynamic performance requirements of the actuator.

## Finite Element Analysis of Voice Coil Actuator

The analytical MEC method used for initial characterization of the actuator was based on several simplifying assumptions. FEA, though much more time and computationally intensive, provides very accurate results and, therefore, can be used to confirm or modify the initial MEC solution as needed. In this section, FEA tools are used to evaluate and confirm the proposed actuator design. The axisymmetric property of the actuator design was exploited so that a 2D FEA model could be used in the analysis. Figure 5 shows the actuator model as well as the FEA solution for the magnetic flux lines and the magnetic flux density, where low-carbon AISI 1018 steel was used for the yoke. From the previous section, the MEC analysis predicted a flux density,  $B_m$ , in the permanent magnet of 0.82T. This compares rather well with the FEA solution that predicts a permanent magnet operating point,  $B_m$ , of 0.9T.

However, the MEC predicts an airgap flux density,  $B_g$ , of 0.54T, which is significantly higher than the FEA-computed airgap flux density of 0.3T. The difference in predicted airgap flux densities can be explained by the magnetic flux lines shown in Figure 5 that do not take their intended path through the airgap. This so-called flux leakage is not considered by MEC analysis, resulting in a higher value than the airgap flux density prediction. A gauss probe inserted in the airgap of the prototype actuator was later used to confirm that the actual airgap flux was in very close agreement with the FEA result of 0.3T. Figure 5 also demonstrates that the flux density in the steel yoke did not exceed 1T at any location, which was well below its saturation point of about 1.5T.

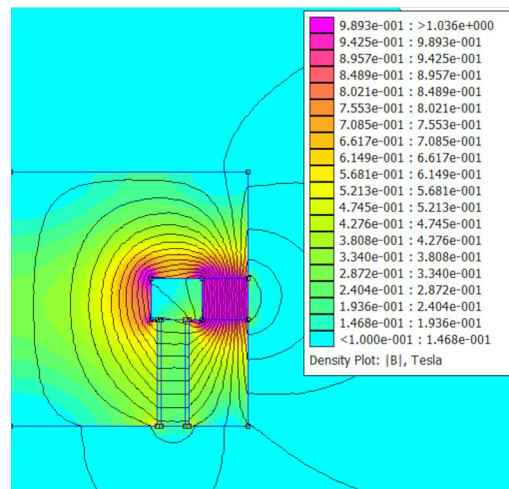


Figure 5. FEA model and magnetic characteristics solution (zero current).

In Figure 6, the airgap flux density is shown along the length of the airgap for various coil currents. When the coil is not energized, the permanent magnet provides a rather uniform magnetic flux density along the length of the gap with the expected reduction near the edges. As seen in the figure, current in the coil produces an armature reaction field that slightly alters the airgap flux density. Positive coil current produces an armature field in the same direction as the permanent magnet, while negative coil current has the opposite effect. Figure 7 shows how this armature reaction effect (Jang & Jeong, 2001) yields a slightly unbalanced force versus current characteristic, which shows that positive current produces a slightly higher force magnitude. Despite the armature reaction effect, the force per current is nearly linear, with a force sensitivity of 3.92 N/A for positive coil current.

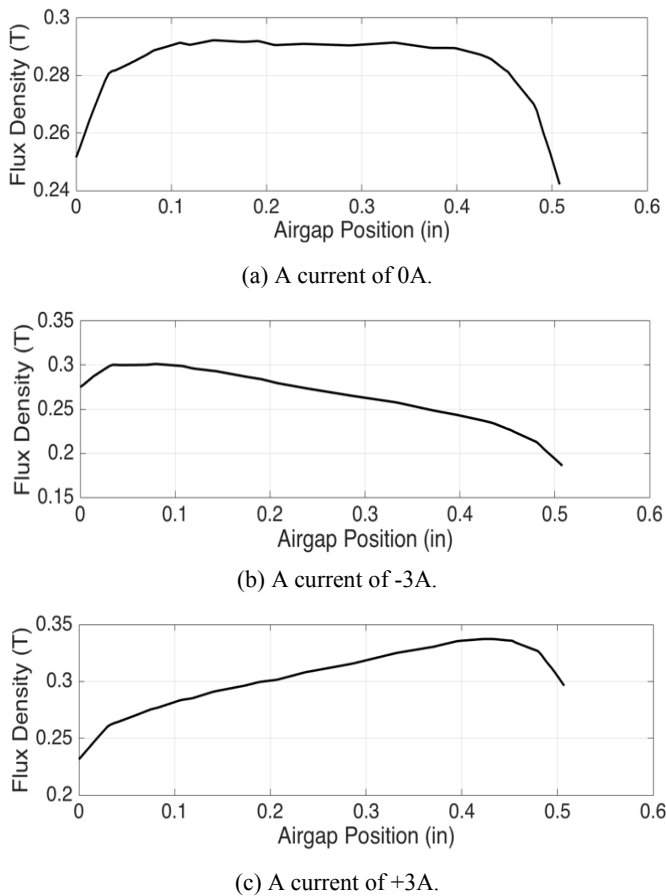


Figure 6. Airgap flux density for different coil currents.

Table 2 shows the results of the voice coil electrical parameters computed using FEA. Note that the FEA-computed parameters are in very close agreement with those obtained with the MEC method.

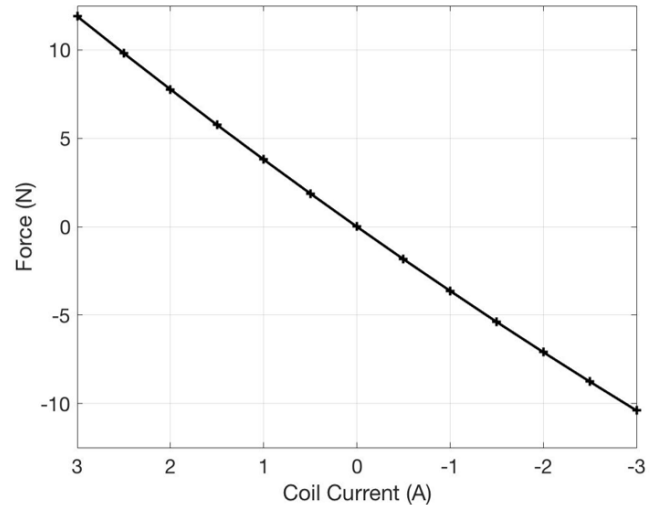


Figure 7. FEA-predicted force versus coil current.

Table 2. FEA-computed electrical parameters.

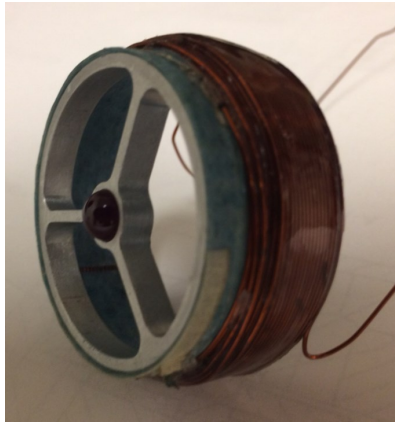
Property	Value
Coil Inductance	2.2 mH
Coil Resistance	1.09 ohms
Coil Power Dissipation	9.81W (at 3 Amps)
Coil Time Constant	2ms

## Fabrication of Actuator Prototype

The coils were wound using AWG 24 magnet wire, and wound on top of a Nomex paper layer on the inner diameter to improve strength. The coil design called for 100 turns, which was implemented by four layers of packed wire with 25 turns per layer. Figure 3 indicates how this coil arrangement was selected to fit into the allotted coil space. The valve operator was then attached to the inner diameter of the Nomex using an epoxy adhesive. Figure 8 shows the constructed voice coil and valve operator.

The yoke of the prototype actuator was constructed with a machined block of AISI 1018 steel that was annealed after machining. Figure 9 shows a sectioned rendering of the prototype actuator. A NdFeB grade 40 ring magnet (rendered in green) magnetized in the axial direction was placed between a T-shaped steel yoke and a steel ring (steel rendered in white//gray), forming an annulus with a radial magnetic field in the airgap. The sapphire ball (red) was pressed into an aluminum yoke (silver), and a coil of 100 turns of AWG 24 magnet wire forms a coil approximately 0.5 inches long. The valve body was machined from three-inch diameter brass (rendered in bronze). The conical valve seat was ma-

chined as a separate part and pressed into the valve body as shown. The total mass of the operator (sapphire ball, aluminum yoke, and copper coil) was 0.03 kg, which was the value used in computing the dynamic force requirements in an earlier section of this paper.



(a) Voice coil and operator.



(b) Voice coil and operator inserted into the outer shell assembly.

Figure 8. Voice coil and outer shell assembly.

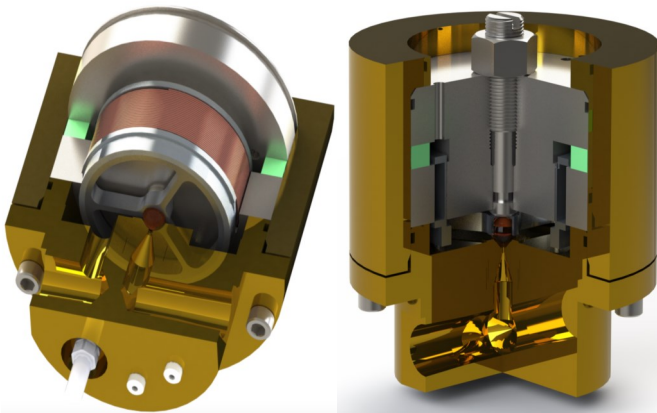


Figure 9. Sectioned renderings of the prototype actuator.

## Actuator and Valve Testing

To confirm the magnetic loading of the prototype actuator, the voice coil was temporarily removed from the yoke so that a gauss probe could be inserted into the airgap. The flux density around the gap was evaluated at the midpoint of the gap length, and along the height of the airgap. Except for near the boundaries of the gap height, the flux density was found to be uniform at a level of approximately 0.3T, which is in good agreement with the FEA prediction shown in Figure 6 (top).

To measure the force produced by the prototype actuator, the voice coil was supplied with a constant current, while a mass attached to the operator was adjusted until the actuator force balanced the gravitational force acting on the mass. Figure 10 shows the results of this test, which includes a linear fit extended to higher A-T than used experimentally. The linear fit indicates that 11.25N force would be produced for a coil current of 3A in a 100-turn coil. This is in close agreement with the FEA prediction of 11.77N (for +3 Amps). The scatter of the data points in Figure 10 is attributed to inaccuracies associated with the simple test set-up—mainly the inconsistent voice coil positioning within the airgap during the tests. Since the voice coil used in this force test did not have the full 100 turns called for in the design, the unit A-T was used so that results could easily be extended to a 100-turn voice coil.

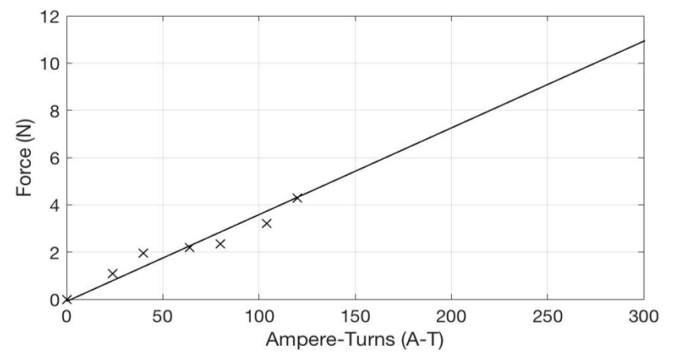


Figure 10. Experimentally determined force versus A-T extrapolated to 300 A-T.

Based on the FEA and test results, the goal of producing a peak actuator force of 12.8N would require peak coil currents of 3.3A (assuming an FEA-computed actuator sensitivity of 3.92 N/A). Although this peak current in the selected magnet wire slightly exceeded the conductor current density of 15 A/mm<sup>2</sup>, the rms conductor current could be kept much lower, considering that the peak current is only required briefly when opening the valve. Finally, the actuator was tested for functionality as a flow valve. For this test, the prototype valve was supplied with 50 psig shop air and used

to fill a 5-gallon (US) pneumatic reservoir. The voice coil of the actuator was driven with a  $\pm 2A$  square wave with duty cycles between 20% and 80% at 100 Hz and below. Flow rate was determined by monitoring the reservoir pressure and temperature over the duration of the test. Figure 11 shows the measured flow rate for various duty cycles applied to the voice coil at a switching frequency of 50 Hz. These tests demonstrate linearity with respect to duty cycle, with a frequency dependent offset due to flow transience (Martin & Batzel, 2018).

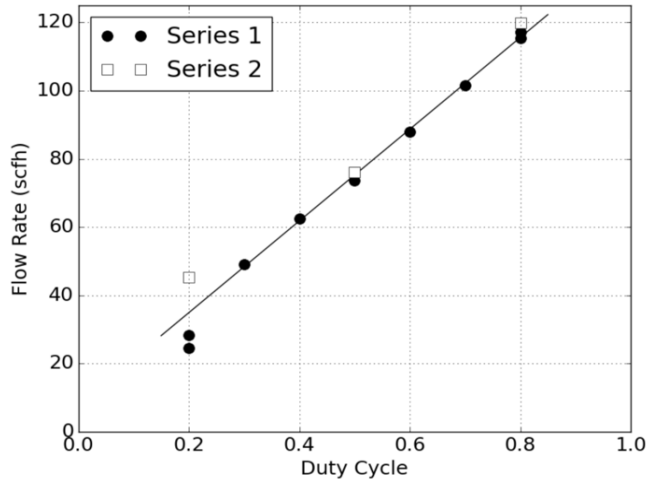


Figure 11. Flow rate versus duty cycle for 50 Hz valve switching.

## Conclusions and Future Work

In this paper, the authors describe the design methodology, construction, and testing of a high-speed actuator to be used in a novel gas mixing application. The gas mixing application requirements were used to identify actuator design, and the electromagnetic components of the actuator were analytically selected to meet these goals. The initial design was carried out using an iterative magnetic circuit analysis. This was followed up with confirmation and fine-tuning using magnetic finite element analysis methods. The analysis showed that the proposed actuator design could meet all of the design goals, including force and dynamic switching. Finally, a prototype actuator was constructed, and a successful demonstration of the switched nozzle approach to flow control was performed. Flow data demonstrated linear behavior with respect to the voice coil duty cycle at switching frequencies up to 100 Hz.

In the future, the actuator performance could be further improved by taking steps to reduce the magnetic flux leakage. This could be accomplished in part by increasing the ratio of the permanent magnet thickness relative to the air-gap length.

## References

- Batzel, T. D., Skraba, A., & Massi, R. (2014). Design and test of an ironless axial flux permanent magnet machine using Halbach array. *International Journal of Modern Engineering*, 15(1), 52-60.
- Beatty, H. W., & Kirtley, J. L. (1998). *Electric motor handbook*. New York: McGraw-Hill.
- Boldea, I. & Nasar, S. A. (2005). *Linear electric actuators and generators*. Cambridge, UK: Cambridge University Press.
- Hanselman, D. (2006). *Brushless permanent magnet motor design*. Lebanon, OH: Magna Physics Publishing.
- Jang, S. M., & Jeong, S. S. (2001). Armature reaction effect and inductance of moving coil linear oscillatory actuator with unbalanced magnetic circuit. *IEEE Transactions on Magnetics*, 37(4), 2847-2850.
- Martin, C. R., & Batzel, T. D. (2018). Digital feed-forward control of gas mixture with high-speed valve switching. *Proceedings of Manufacturing Science and Engineering Conference 2018*. Paris: Atlantis Press.
- MS Wire Industries. (2014). *Bondable magnet wire*. Retrieved from [http://www.mswire.com/pdf\\_files/mws\\_tech\\_book/page8\\_9\\_35.pdf](http://www.mswire.com/pdf_files/mws_tech_book/page8_9_35.pdf)
- Roemer, D. B., Bech, M. M., Johansen, P., & Pedersen, H. C. (2015). Optimum design of a moving coil actuator for fast-switching valves in digital hydraulic pumps and motors. *IEEE/ASME Transactions of Mechatronics*, 20(6), 2761-2770.
- Soong, W. L. (2016). *The art of electric machine research, ch. 2 – Electrical conductors*. Retrieved from <http://www.eleceng.adelaide.edu.au/research/power/pebn/art%20of%20emr%20-%20ch2%20conductors%20sep16.pdf>
- Sung, B. J., & Kim, D. S. (2018). A design method of voice coil type high speed actuator for valve operation. *Proceedings of the 15th International Conference on Electrical Machines and Systems*. Piscataway, NJ: IEEE.
- Yatchev, I., Hinov, K., Balabozov, I., & Krasteva, K. (2011). Static force characteristics of electromagnetic actuators for braille screen. *Facta Univ - Electronics and Energetics*, 24(2), 157-167.

## Biographies

**TODD BATZEL** received his BS and PhD degrees in electrical engineering from Pennsylvania State University in 1984 and 2000, respectively, and MS degree in electrical engineering from the University of Pittsburgh in 1989. Currently, he is a professor of electrical engineering at Penn State University, Altoona College. Dr. Batzel may be reached at [tdb120@psu.edu](mailto:tdb120@psu.edu)

---

**CHRISTOPHER MARTIN** is an assistant professor of mechanical engineering at Penn State University's Altoona College. Dr. Martin received his BS, MS, and PhD degrees in mechanical engineering from Virginia Tech in 2004, 2006, and 2009, respectively. He also holds a certificate in engineering education from Virginia Tech. Dr. Martin may be reached at [crm28@psu.edu](mailto:crm28@psu.edu)

**DIMITRIS KIAOULIAS** is an undergraduate student in the BS in Electromechanical Engineering Technology (BSEMET) program at Penn State Altoona. He may be reached at [dwk5403@psu.edu](mailto:dwk5403@psu.edu)

**MATTHEW COWLER** is an undergraduate student in the BS in Electromechanical Engineering Technology (BSEMET) program at Penn State Altoona. He may be reached at [mjc5921@psu.edu](mailto:mjc5921@psu.edu)

# FOOTAGE ESTIMATION OF MOVING OBJECTS BY MULTI-CAMERA TRIANGULATION THROUGH WIRELESS NETWORKS

---

Sangho Park, Central Connecticut State University; Xiaobing Hou, Central Connecticut State University

## Abstract

In this study, the authors examined the feasibility of mobile multi-camera triangulation via heterogeneous wireless networks. The motivation of this study was to develop a versatile mobile multi-camera system that could capture the object of interest in the scene and estimate the size of the footage of the object in terms of objective measurement. The footage size of object is an important invariant feature useful for computational vision, object recognition, intelligent visual surveillance, traffic monitoring, etc. Even if object appearance varies depending on viewpoints, object footage is invariant and can be estimated in terms of objective measure by using multiple camera views. The multi-camera triangulation process merges multiple view-dependent camera images of the object and transforms them into a view-independent orthographic top-down projection that enables footage estimation. The traditional method of multi-camera triangulation is to use cameras linked through video cables to a computer dispatched on site. This method is cumbersome and can even be unachievable in outdoor environments. The cameras must be physically linked to the cables and the dispatched computer. Monitoring a wide area in a large-scale scene is not possible, due to this limitation.

In this paper, the authors propose an alternative method: mobile multi-camera triangulation via wireless networks. The method uses multiple video feeds simultaneously captured by multiple cameras (called camera modules). Several camera modules can communicate through a wireless network with a remote server that collects the multiple video feeds. The server also maintains time synchronization among the camera modules by sending them a common local time stamp. In this study, the system used two camera video feeds connected to a server via Wi-Fi intranet, using user datagram protocol (UDP), which enabled the footage estimation of moving objects captured in an outdoor environment. Depending on the network bandwidth, the system is scalable to include more camera nodes.

## Introduction

There has been a growing interest in making sensor-based systems to enhance the safety and efficiency of human-

inhabited environments. The camera sensor is one of the most useful sensors for providing rich information about the monitored scene. More cameras can be deployed to cover wider areas—roads, shopping malls, public plazas, etc.—to monitor the activities of both humans and objects. Reviews of general research on vision-based understanding of human motion can be found in studies by Aggarwal & Cai (1999), Gavrilu (1999), and Moeslund & Granum (2001). With advances in camera technology, more video data can be collected and analyzed for situational awareness of the monitored sites. The majority of existing camera systems involve human operators and their manual analysis to achieve meaningful interpretation of the captured videos.

Video data (a sequential collection of image frames) is basically a simplified 2D representation of real-world 3D scenes. The 2D representation results in ambiguity in video analysis. For example, the same object in a scene appears very different in size, depending on the camera perspectives. Automated analysis of video scenes using artificial intelligence or machine learning should be able to deal with the ambiguity. Occlusion between multiple objects is another limiting factor that hinders the proper analysis of video data.

If multiple cameras are used to capture a scene from different perspectives, the ambiguity can be reduced significantly (Park & Trivedi, 2008). Distributed multi-camera systems have been introduced to address such issues. A review of distributed surveillance systems can be found in the work by Valera Espina & Velastin (2005). Using multiple cameras also provides useful ways to obtain invariant features of objects from images such as object size and location. For example, multi-camera triangulation process merges multiple view-dependent camera images of the object and transforms them into a view-independent orthographic top-down projection, which enables footage estimation.

In this paper, the authors propose using mobile multi-camera triangulation via wireless networks. The proposed approach extends traditional methods for triangulation by eliminating physical cable connections between cameras and a computer, which is useful for monitoring a large-scale scene where a cable connection is impossible or impractical.

## Multi-Camera Triangulation

The proposed methodology is based on multi-view geometry (Hartley & Zisserman, 2003; and Ma, Soatto, Kosecka, & Sastry, 2001) in computational vision. The method starts by modeling the process of image formation when a scene is viewed through a camera. Figure 1 shows how a pinhole camera model (Forsyth & Ponce, 2003) was adopted, which assumed that exactly one ray from each point in the scene would pass through the pinhole lens and hit the image plane. Figure 1 further shows the 3-dimensional point  $P$  in the world coordinate system with respect to the  $\{X_1, X_2, X_3\}$  axes with its origin,  $O$ . The origin  $O$  corresponds to the camera aperture. Figure 1 also denotes the corresponding 2-dimensional point  $Q$  on the imaging plane of the camera with respect to the  $\{Y_1, Y_2\}$  axes of the image coordinate system with its origin  $R$ . The origin  $R$  of the image plane corresponds to the image center.

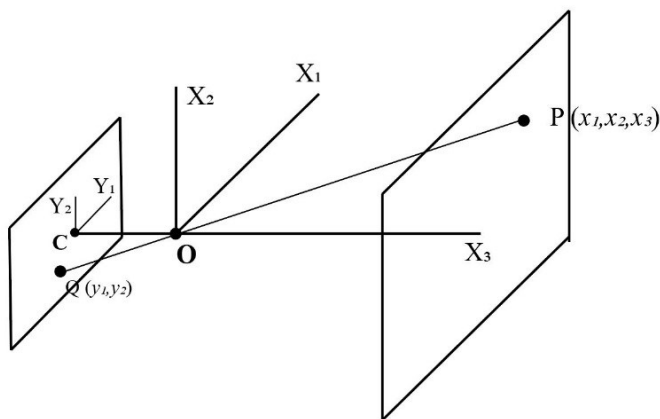


Figure 1. Image projection in a pinhole camera.

The vector pointing from the camera center  $O$  to the world coordinate point  $P$  is represented in lowercase letters  $(x_1, x_2, x_3)$ , and the vector pointing from the camera center  $O$  to the corresponding image coordinate point  $Q$  would be represented in lowercase letters  $(y_1, y_2)$ , respectively. The camera's imaging process is intended to map point  $P$  in the 3D space to point  $Q$  on the 2D image plane. This process is modeled in Equation 1 (Hartley & Zisserman, 2003), where the superscript  $t$  stands for column vector notation. This mapping, from the higher 3D to the lower 2D dimension, typically results in the loss of information (e.g., loss of depth perception) with a single camera.

$$(x_1, x_2, x_3)^t \xrightarrow{\text{Projection}} (y_1, y_2)^t \quad (1)$$

If multiple cameras are used, depth information can be recovered by multiple-view geometry. Figure 2 shows the multiple-view geometry with two cameras for which camera

centers are  $O_1$  and  $O_2$ , respectively. Each of the cameras projects the common 3D world point  $x$  to the corresponding image points  $y_1$  and  $y_2$  on the camera's imaging plane, respectively (Ma et al., 2001). The bold characters  $x$  and  $y$  denote the point vectors, not the single coordinate values. Equation 2 shows how the second camera's relative configuration with respect to the first camera can be defined in terms of the relative rotation matrix  $R$  and translation vector  $T$  (Ma et al., 2001). Standard algorithms for camera calibration (Ma et al., 2001) easily establish the  $R$  and  $T$  parameters. Note that the same point  $x$  in the 3D world appears very different in the two image planes as vectors  $y_1$  and  $y_2$ , respectively, due to the perspective distortion effect.

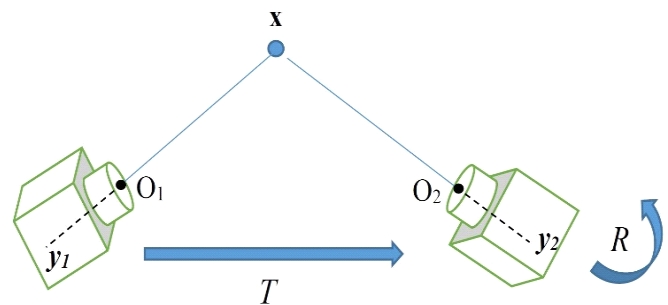


Figure 2. Multiple-view geometry involving two cameras centered on  $O_1$  and  $O_2$ , respectively.

$$y_2 = R y_1 + T \quad (2)$$

Figure 3 shows how image appearance of the same object can vary significantly according to camera perspectives. Reliable analysis of video scenes, such as classification of object types, may benefit from the estimation of the view-invariant size of the object. It was observed that the approximate size of the object's footage area is invariant to translation and rotation, if the camera viewpoint is transformed to the virtual top-down viewpoint.

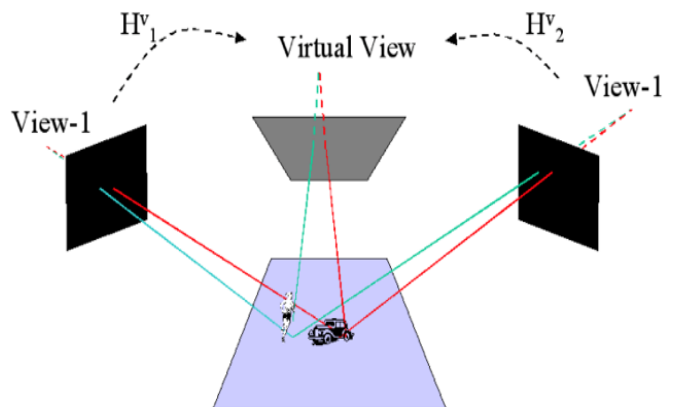


Figure 3. Planar homography mapping for top-down plan-view generation.

Planar homography (Criminisi, Reid, & Zisserman, 1999) can be used to achieve the virtual top-down view and project the object's footage onto the ground plane of the world coordinate system. A homography matrix,  $H$ , maps corresponding points between image coordinate systems. If  $H_m^n$  is denoted as the homography from arbitrary view  $m$  to  $n$ , multiple arbitrary camera views can be registered by the series of concatenated homographies as shown in Equation 3 (Hartley & Zisserman, 2003):

$$H_m^n = H_{n+1}^n H_{n+2}^{n+1} \cdots H_{m-1}^{m-2} H_m^{m-1} \quad (3)$$

The 4-point algorithm (Criminisi et al. 1999) was used to compute the homography matrix  $H$ . The 4 points were selected either from shared image corners or by having a person to walk around the shared region.

Equations 4 and 5 (Criminisi et al. 1999) show how the points in view-1,  $P_1$ , and points in view-2,  $P_2$ , can be mapped to corresponding points in the virtual view,  $P_1^v$  and  $P_2^v$ , by homography matrices  $H_1^v$  and  $H_2^v$ , respectively:

$$P_1^v = H_1^v P_1 \quad (4)$$

$$P_2^v = H_2^v P_2 \quad (5)$$

Figure 4 depicts the process of multi-camera triangulation. The planar homography constraint assumes that all of the pixels lie on the same plane (i.e., the ground plane in 3D world.) Pixels that violate this assumption result in mapping to a skewed location on the projection plane. Multiple views of the same object are transformed by planar homography computation, Figure 4(a); perspective projection is made for triangulation, Figure 4(b); and, the intersection of the projected images are used as the footage region of the object on the ground, Figure 4(c). By intersecting multiple projection maps of the same object, the object's footage area can be estimated, regardless of the original camera perspectives.

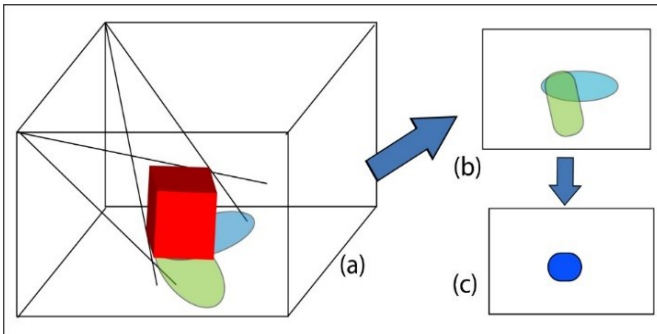


Figure 4. Multi-camera triangulation can be used to estimate object footage area: (a) planar homography computation; (b) perspective projection for triangulation; and, (c) footage area segmentation.

## Video Frame Transmission from Mobile Cameras to Remote Server

The traditional method of multi-camera triangulation is to use cameras linked to a computer through video cables for video-frame transmission and time synchronization. This method is cumbersome and can even be unachievable in outdoor environments, where cameras cannot be physically linked to the cables and the dispatching computer. Monitoring a wide area in a large-scale scene is not possible, due to the limitation. In this paper, the authors propose an alternative method: mobile multi-camera triangulation via wireless networks. In mobile systems, it should be guaranteed to capture the common scene in a synchronous manner and to transmit the video data to the remote server with minimal delay. Modern cameras are reliable for data acquisition over a fixed-frame rate (e.g., 30 frames per second). It is assumed that multiple cameras can capture their videos at the same fixed frame rate, which relaxes the constraint of periodic data capture between multiple cameras. Since the frame rate is fixed, the only remaining factor to consider is synchronization between multiple cameras. It is not practical to use hardware or software triggers to synchronize multiple cameras remotely. Instead, the authors propose sharing the server computer's local clock time with the remote camera modules in order to time-stamp individual video frames.

Individual camera modules capture video frames, time-stamp each frame, and store them in a local queued buffer. The queued frames are individually transmitted to the remote server via an IEEE 802.11 network (Wi-Fi) using the user datagram protocol (UDP.) The remote server receives video frames from the dedicated UDP port, re-aligns the frames with temporally nearest frames of the other streams for synchronization, and reconstructs the videos for all of the camera nodes.

## Design and Implementation

Figure 5 shows a diagram of the overall system. The system starts by establishing the wireless network connection between the remote server and the mobile camera modules. A dedicated port number is assigned to each camera module, and the port is used for time synchronization (dotted double-ended thin arrow in Figure 5) and video frame transmission (dotted single-ended thick arrow in Figure 5). Multi-camera synchronization is achieved by the wireless network server that receives video frames (see Figure 6 for an example of a video-pair frame), as explained in the previous section. Computer-vision algorithms conduct perspective projection and triangulation (see Figure 7). Figure 8 shows how a color-based object detection/tracking algorithm

(Allen, Xu, & Jin, 2004) follows the processing, and the footage estimation is achieved by analyzing the detected footage on the virtual top-down ground plane.

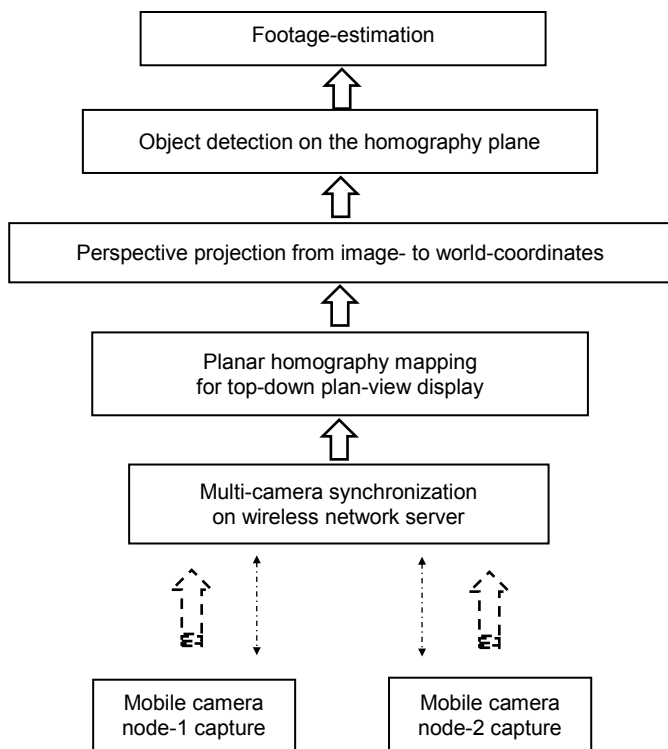


Figure 5. Overall system diagram for mobile multi-camera triangulation via wireless network.



Figure 6. Example of a video-frame pair of a common scene captured from two camera modules.

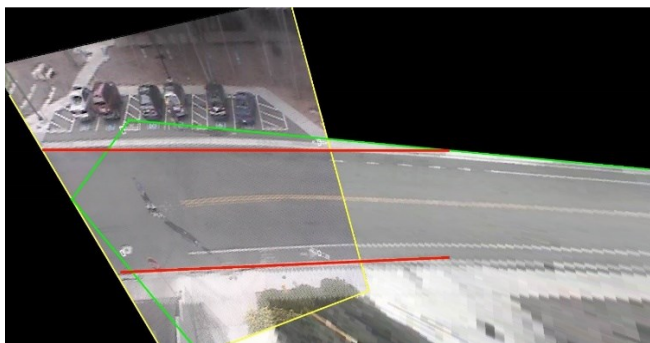


Figure 7. Perspective projection and triangulation of Figure 6 on the virtual top-down view plane.

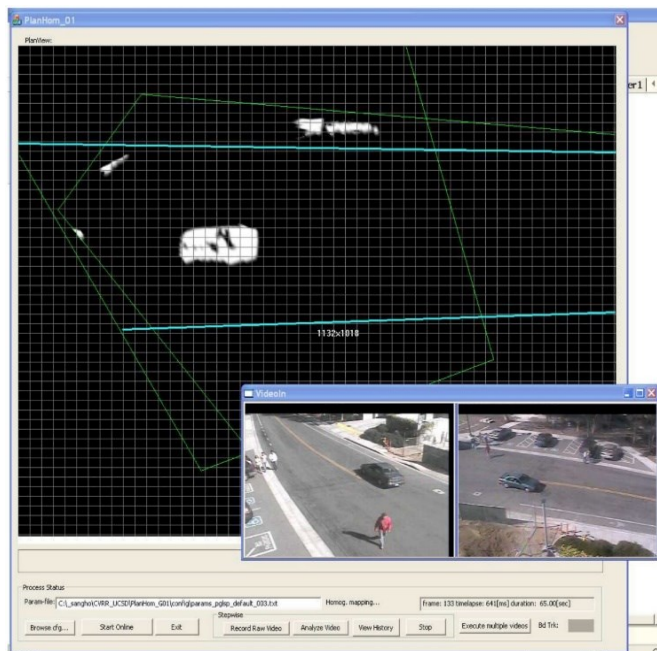


Figure 8. Graphic user interface to estimate footage area of detected objects. Inset: example video frames used to estimate the footage areas in the GUI.

To detect moving objects on the homography plane, a scene model is defined as follows: the paved road and stationary objects (e.g., parked cars) on the ground comprise the background scene, while any moving objects of interest (e.g., passengers, sedans, and buses) comprise the foreground scene. Object detection segments the foreground objects from the background by the following steps.

Pseudocode for object detection:

1. Train a basic model of the background homography scene over several minutes by learning the statistical distribution of the color, saturation, and hue of the scene.
2. Receive a new input homography scene for foreground segmentation.
3. Adjust the thresholds of the statistical parameters to best segment the known foreground.
4. Maintain the overall scene model.
5. Use the learned model to segment the foreground from the background.
6. Periodically update the learned background parameters.

The detected objects at a given video frame need to be tracked over the video sequence. Color-based object detection/tracking algorithm (Allen, Xu, & Jin, 2004) is adopted to track the objects over time as follows.

Pseudocode for object tracking:

1. Apply image processing steps to refine the foreground scene by removing the imaging noise.
2. Generate a profile of each detected object in terms of its color distribution and size.
3. Store the list of profiles for all detected objects in the current video frame.
4. Associate the most similar objects between consecutive video frames by comparing the object profiles.
5. Establish the track of moving objects over time.

To estimate the footage of the detected objects, the following image processing steps are taken.

Pseudocode for footage estimation:

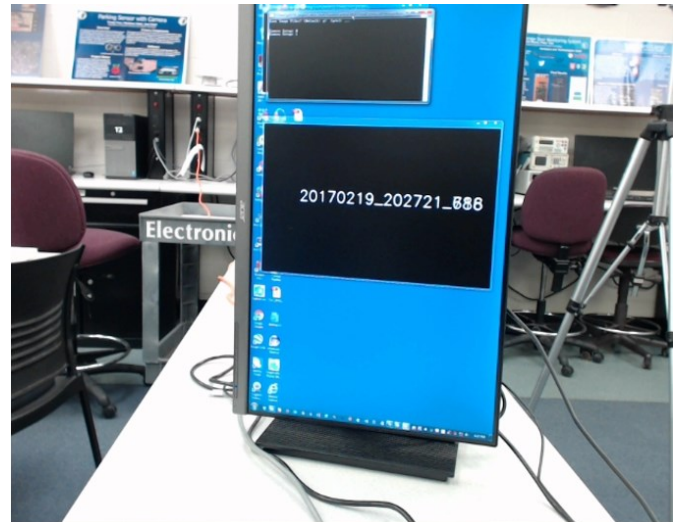
1. Label the track of each object over the video sequence.
2. Calculate the number of foreground pixels in the tracked object on the homography plane.
3. Accumulate training data to learn the footage sizes of objects
4. Classify the objects in terms of their footage.

## Experiments

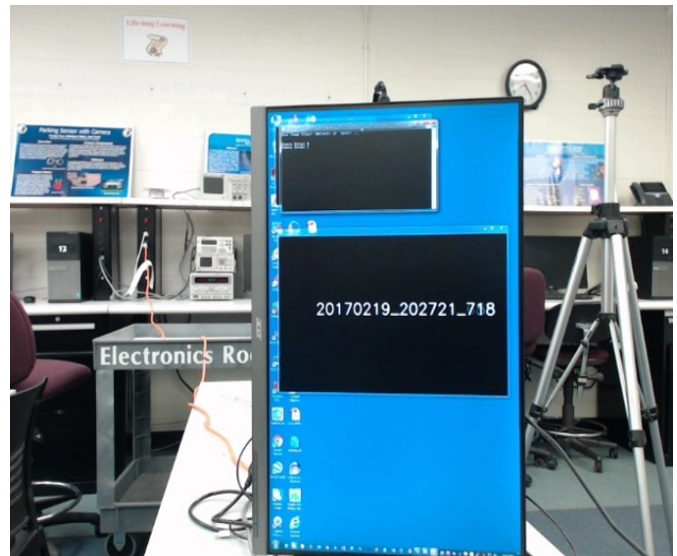
The system prototype was tested using two video feeds transmitted from two camera modules to a remote server. Each camera module was comprised of a USB camera and an independent notebook computer that uses the USB camera. Figure 9 shows an experimental setup to test the concurrent video transmissions from two camera modules to a remote server. Each camera module captures image frames of  $640 \text{ pixels} \times 480 \text{ pixels}$ . The frame rate of the captured videos was 10 frames per second, which indicates a 100-millisecond gap between consecutive frames in a video. Wi-Fi transmission delay due to the server's internal processing steps was approximately 3 milliseconds with 2.4 GHz wireless router. This means that the server's batch processing for video frame collection from two independent remote sources is fast enough to catch all the video-frame UDP packets without any packet loss, since the transmission delay is negligible compared to the frame capture rate. After the batch processing is done to queue the inbound video frames, the server performs the multi-camera synchronization step in Figure 5.

Figure 10 shows an example video feed juxtaposed with two camera views as a pair to monitor a site involving a human crossing the road and a car passing the person. In the current experiment, each camera view was loaded to an independent camera module and sent to a remote server wirelessly. The juxtaposition to make the correct pair is the result of multi-camera synchronization on the wireless net-

work server in Figure 5. The direction of the stream in Figure 10 is downward in the left column and then downward in the right column. Each column shows juxtaposed camera views after synchronization.



(a) Image from camera-1.



(b) Image from camera-2.

Figure 9. Experimental setup to measure wireless transmission of video frames.

Figure 11 shows the results of the perspective projection and triangulation involving the videos in Figure 10. Color-based foreground segmentation segregates the moving targets in the scene (a human and a car.) The elongated shadow-like blobs are not shadows; they are perspective project results of the detected objects.



Figure 10. Example video-frame pairs from two cameras that monitor a site involving a human and a car. The order of the video stream is downward in the left column, (a) through (c), and then downward in the right column, (d) through (f).

Figure 12 shows the detected footage areas corresponding to the car and the person. Note that the blob sizes of the car and the person do not change significantly over time, even if the object appearances in the raw video changes depending on the camera perspective. It means that the proposed system can objectively estimate the footage sizes of detected targets. Footage area is an invariant feature of objects and can be used for classification purposes. For example, Figure 13 shows different categories of the targets: persons as pedestrians, a small vehicle (such as a sedan), and a large vehicle (such as a bus).

A nearest-neighbor classifier is trained based on training data regarding footage area of detected objects. Table 1 shows the classification performance in the form of a confusion matrix, where recall is defined as the fraction of the total number of objects in a particular class that are classified correctly by the system for that class. Precision is defined as the fraction of objects recognized for a particular class that are actually correct. The overall classification performance in terms of the precision and recall is over 90% correct. The incidences of misclassification are mainly due

to image processing noise during the color-based foreground segmentation.

Table 1. Confusion matrix of object classification based on footage size.

Confusion Matrix	Large Vehicle	Small Vehicle	Person	Recall
Large Vehicle	39/41	2/41	0	0.95
Small Vehicle	3/55	52/55	0	0.95
Person	0	4/65	61/65	0.94
Precision	0.93	0.90	1.0	

## Conclusions

The main objective of this study was to establish the feasibility for determining whether future research on mobile multi-camera triangulation is warranted. In this paper, the authors showed how two remote video feeds can seamlessly

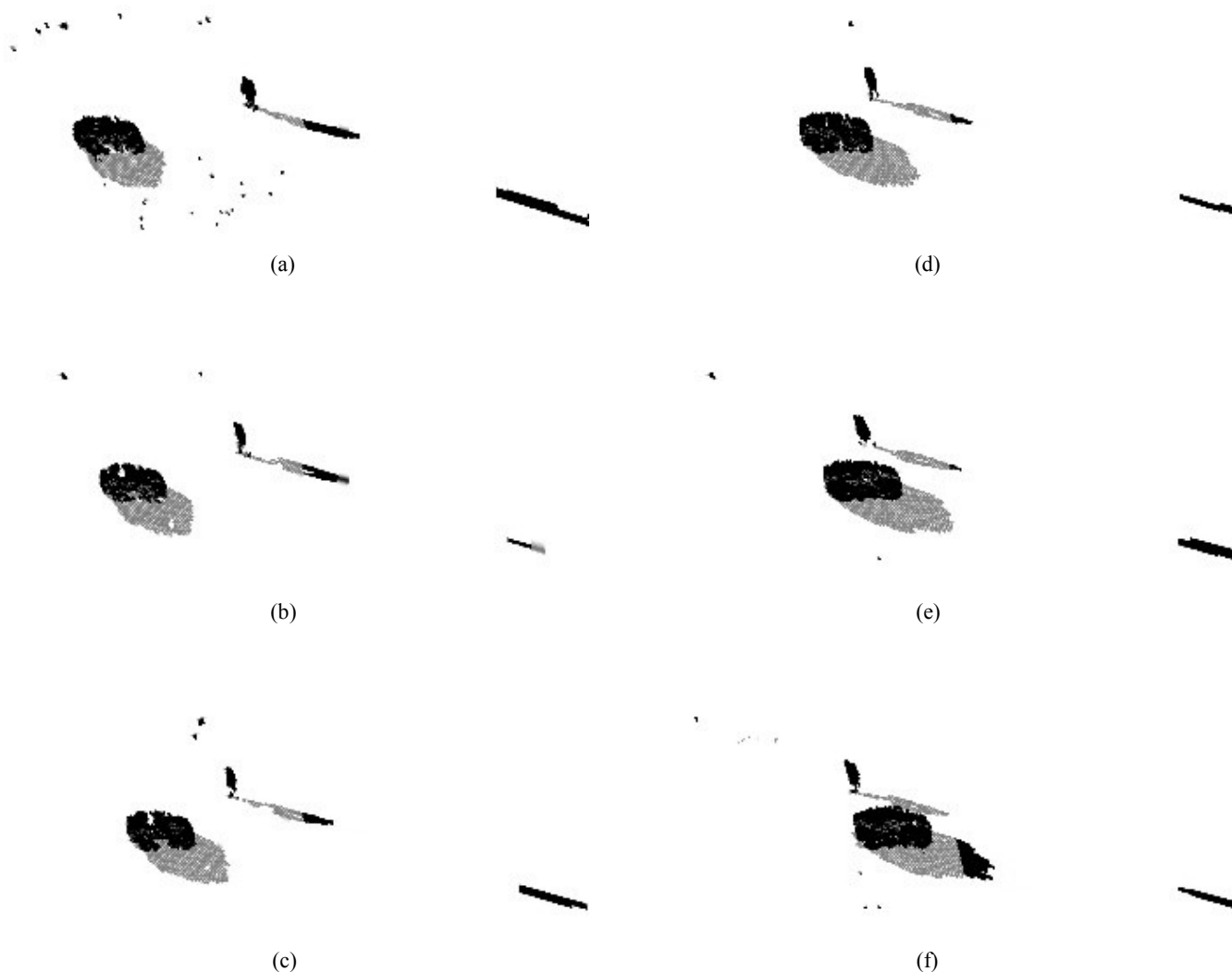


Figure 11. Perspective projection and triangulation of Figure 10 on the virtual top-down view plane. The order of the video stream is downward in left column: (a) through (c) and then downward in right column: (d) through (f).

be triangulated to form a virtual top-down view for the detection of footage areas of objects in the scene. A batch processing approach was adopted to transmit videos in a frame-by-frame manner to a remote server via Wi-Fi network using UDP packets. The server correctly generated video data from multiple streams of input frames and performed object classification tasks at over 90% correctness. In the near future, dedicated mobile embedded systems will be implemented as camera modules for fast processing and versatile deployment. Other future research will include the investigation of reliable color-based foreground image segmentation, which is still an open research question in computer vision.

## Acknowledgments

This research was supported and funded by an AAUP MR&R Research Grant from Central Connecticut State University.

## References

Aggarwal, J. K., & Cai, Q. (1999). Human motion analysis: A review. *Computer Vision and Image Understanding*, 73(3), 295-304.

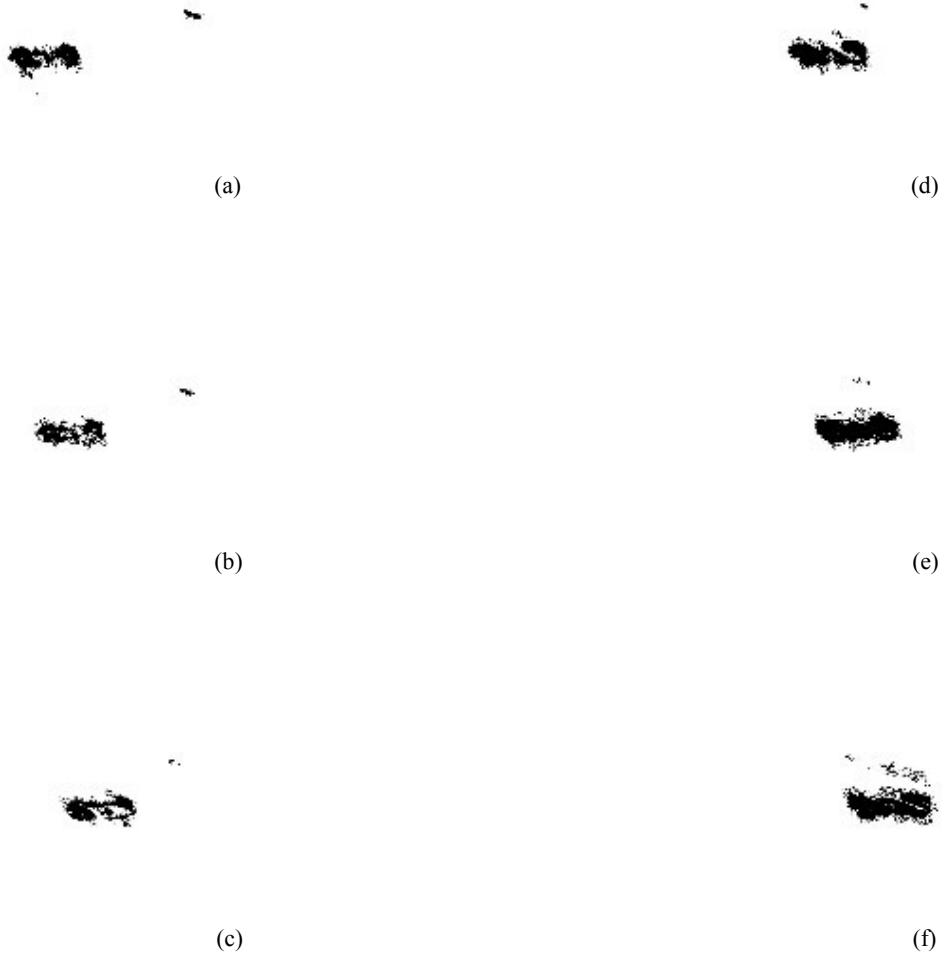


Figure 12. Detected footage areas of the scene in Figure 10, which involves a large footage blob for the car and a small blob for the human in the scene. The order of the video stream is downward in the left column, (a) through (c), and then downward in the right column, (d) through (f).



(a) Video-frame pair involving a person and a small vehicle.



(b) Video-frame pair involving a large vehicle.

Figure 13. Examples of different object categories.

- 
- Allen, J. G., Xu, R. Y. D., & Jin, J. S. (2004). Object tracking using camshift algorithm and multiple quantized feature spaces. *Proceedings of the Pan-Sydney Area Workshop on Visual Information Technology*. Canberra, Australia: Australian Computer Society.
- Criminisi, A., Reid, I., & Zisserman, A. (1999). A plane measuring device. *Image and Vision Computing*, 17(8), 625-634.
- Forsyth, D., & Ponce, J. (2003). *Computer vision: A modern approach*. Upper Saddle River, NJ: Prentice Hall.
- Gavrila, D. (1999). The visual analysis of human movement: A survey. *Computer Vision and Image Understanding*, 73(1), 82-98.
- Hartley, R., & Zisserman, A. (2003). *Multiple view geometry in computer vision*. (2nd ed.). New York: Cambridge University Press.
- Ma, Y., Soatto, S., Kosecka, J., & Sastry, S. (2001). *An invitation to 3-D vision: From images to geometric models*. New York: Springer.
- Moeslund, T. B., & Granum, E. (2001). A survey of computer vision-based human motion capture. *Computer Vision and Image Understanding*, 81(3), 231-268.
- Park, S., & Trivedi, M. (2008). Understanding human interactions with track and body synergies (TBS) captured from multiple views. *Computer Vision and Image Understanding*, 111(1), 2-20.
- Valera Espina, M., & Velastin, S. (2005). Intelligent distributed surveillance systems: A review. *IEE Proceedings—Vision, Image and Signal Processing*, 152(2), 192-204.

## Biographies

**SANGHO PARK** is an assistant professor of computer electronics and graphics technology at Central Connecticut State University, where he teaches courses on circuit analysis, analog electronics, telecommunication systems, and capstone projects. His research interests include sensor-based intelligent systems, computer vision, image processing, and machine learning. Dr. Park may be reached at [spark@ccsu.edu](mailto:spark@ccsu.edu)

**XIAOBING HOU** is an associate professor in the Department of Computer Electronics and Graphics Technology at Central Connecticut State University. He received his PhD in information science from the University of Pittsburgh in 2006. Dr. Hou's teaching and research interests include computer networking and information security. He is a member of IEEE and ACM. Dr. Hou may be reached at [xhou@ccsu.edu](mailto:xhou@ccsu.edu)

# NUMERICAL FLOW VISUALIZATION OF A RECTANGULAR SHELL-AND-TUBE THERMOSYPHON HEAT EXCHANGER WITH BAFFLED CROSSFLOW

Mebougna Drabo, Alabama A&M University; He Tao, Stony Brook University; Wei Zhong, Stony Brook University; Jon P. Longtin, Stony Brook University; Thomas Butcher, Brookhaven National Laboratory; Narinder Tutu, Brookhaven National Laboratory; Rebecca Trojanowski, Brookhaven National Laboratory

## Abstract

The vast majority of baffled shell-and-tube heat exchangers studied in the past are cylindrical in design. Correlations developed for these designs may not always be applicable for a rectangular geometry, since the fluid flow on the shell side can be considerably different than that of a circular geometry. In this paper, the authors present the results of a shell-side flow simulation for a rectangular cross-sectional shell-and tube heat exchanger designed for cooling and condensing the water vapor in the flue gas from a natural-gas-fired power plant. Numerical solutions to the flow system were used to evaluate alternative design parameters, including the number of baffles, baffle dimensions, orientation of baffles, etc., to improve heat exchanger performance. The results show that a substantial fraction of the tubes immediately underneath the baffles were flow starved. As a result, changing the basic design parameters of the heat exchanger does not necessarily improve heat exchanger performance: either the heat transfer may not improve significantly or the pressure drop will become unacceptably high. Thus, in order to obtain optimal heat-transfer performance, a number of ideas for redistribution of flow need to be investigated. It should also be noted that, even if nearly uniform flow distribution is achieved for all regions, heat transfer may not be the highest, because the average flow velocity (and, hence, the heat-transfer coefficient) may not be the highest.

## Introduction

Baffled shell-and-tube heat exchangers are popular heat exchangers used in a wide range of thermal engineering applications. These devices have been studied extensively in the past, including experimental, numerical, and analytical approaches. The vast majority of these devices, however, are cylindrical in design. Far less common is a rectangular geometry. Fluid flow on the shell side of shell-and-tube heat exchangers can be very complicated, depending upon the particular design geometry. As a result, heat transfer and friction drop correlations available in the literature may not always be applicable, if none are to be found for the specific geometry and for the valid range of governing dimension-

less numbers in the correlation. Furthermore, the choice of optimal design parameters (number of baffles, dimensions, orientation of baffles, etc.) may not always be obvious. As a result, numerical flow visualization via computational fluid dynamics (CFD) may provide valuable insight and benefit for design purposes.

In this paper, the authors present the results of a flow simulation for a rectangular cross-sectional shell-and tube heat exchanger designed for cooling and condensing the water vapor in the flue gas from a natural-gas-fired power plant. The tubes in the device are actually two-phase thermosyphons, which provide excellent heat transfer characteristics. In shell-and-tube heat exchangers with baffles, the fluid on the shell side must undergo at least a few 180° changes in flow directions. As a result, it is to be expected that many regions of many tubes may be flow starved. This departure for non-uniformity of flow (velocity) distribution is clearly a function of the particular design geometry. The heat transfer and pressure drop performance of the designed heat exchanger are clearly dependent on flow distribution. Thus, to obtain optimal heat transfer performance, a large number of ideas (for redistribution of flow) need to be investigated. In order to understand the performance for the basic design of the DEWCOOL heat exchanger, and to generate ideas for design improvements, numerical flow visualizations were performed via SOLIDWORKS commercial software.

There are many standard methods for the shell-side design for shell-and-tube heat exchangers, including the Bell-Delaware and Kern methods (1981). Clearly, these would be applicable for the many standard shapes of shell-and-tube heat exchangers upon which these methods are based. For appreciably different design geometries, other numerical computational methods must be used to optimize the heat exchanger design. An extensive review of CFD analyses of heat exchangers for design evaluation is provided by Bhutta et al. (2012), in which the authors document various models and commercial CFD codes used by various investigators along with comments on comparison of CFD predictions with experimental data, where available. A vast majority of such analyses are for circular cross-sectional shells and very specialized novel designs.

In addition to the CFD models that simulate real objects, such as tubes in the shell, there are also numerical methods that are based on a resistance model for the tube bundles. He et al. (2005) used such a numerical computational model that is based on the concept of distributed resistance and a porous medium model (instead of simulating actual tubes) to simulate the flow on the shell side for various baffle configurations. This analysis was also for a circular cross-sectional shell. Ozden and Tari (2010) investigated the shell-side design performance of circular cross-sectional shell-and-tube heat exchangers as a function of baffle spacing, baffle cut, and shell diameter using a commercial CFD code. They compared their predictions to the Bell-Delaware and Kern methods and found that the CFD predictions for total heat exchange rate was in very good agreement with the Bell-Delaware method. They also found large regions of low-velocity recirculation zones between baffles.

The objective of this current investigation was to evaluate the details of the flow pattern (velocity distribution) on the shell side, and the performance (pressure drop and sensible heat removal rate) of the DEWCOOL unit for a few design configurations. Velocity distribution patterns could provide clues to better design configurations, or at least show the reasons why some design modifications do not yield better results. Since the SOLIDWORKS flow module does not include two-phase flow and condensation, it was not expected to provide the correct heat removal rate due to condensation heat transfer. Nevertheless, it was expected to show which design (in terms of number of baffles, their locations, or other flow-diverting obstructions) is better.

## The Heat Exchanger

Figure 1 shows a 3-D drawing of the heat exchanger. It contains 45 1.00-inch (O.D.) tubes arranged in a rectangular pattern. The 1-meter-long tubes are made of high thermal conductivity (15 W/mK) polyphenylene sulfide (PPS) polymer with 70% exfoliated graphite. The tubes are manufactured by Technoform Kunststoffprofile GmbH in Germany. The heat exchanger has several baffles in it that force the flow alternately across the tube bundles, similar to many tube-in-shell heat exchangers. The baffle plates are 1/32"-thick sheet metal, and the number and position of the baffles can be adjusted as desired. The baffles have either 1"x 1" square holes or 1" round holes for polymer tubes to pass through. In practice, the baffles are made from two interlaced metal sheets that form 1"x 1" square holes around the tubes. The corners of the square opening provide a small path for flue gas to flow through. These openings can be covered up with thin washers to seal the corners and effectively produce 1" round holes that completely seal the tubes. The washer material can be thin plastic, felt, or aluminum

foil. Both configurations were explored in this study. A larger number of baffles increases both the heat transfer as well as the pressure drop. For this study, it was desirable to keep the pressure drop through the heat exchanger to no more than 1" of water (250 Pa).

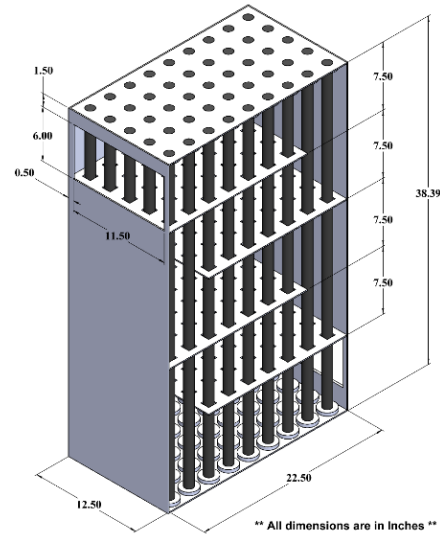


Figure 1. A 3-D rendering of the DEWCOOL shell-and-tube heat exchanger for the 4-baffle base design configuration. The front wall of the shell is transparent for visualization of tubes. The exit duct is not shown.

The tubes were actually configured as thermosyphons, which are two-phase heat exchange devices that provide extremely high heat transfer. The tubes contained a saturated liquid-vapor mixture of water under vacuum. Water was pumped to the top of the tubes to form a thin liquid film on the inside of the tubes. Heat passing into the tube evaporates the liquid film, whose vapor is then carried to a separate external condenser where heat is removed to condense the vapor back to liquid; the process then repeats. Because of the extremely high heat transfer rates inside the thermosyphon, and for the purposes of CFD simulation, it was assumed that the inside surface temperature of the tubes was a constant 30°C. Thus, only the shell-side fluid flow (and heat transfer) and thermal conduction within the tube were simulated.

## CFD Flow Simulation

SOLIDWORKS Premium 2016 with embedded SOLIDWORKS Flow Simulation module was used for all simulations. The mesh sizes for these computations ranged from 3.5 million to 3.8 million. The total central processing unit (CPU) time for the three Baffles-Modified run was 16 hours and 21 minutes. For all other cases, the CPU time was about 4 hours and 16 minutes. The computations were made on a

PC with Intel (R) Core(TM) i7-3770K CPU running at 3.50 GHz. The resulting SOLIDWORKS simulations provided the pressure drop, flow patterns, and convective heat transfer through the system. The SOLIDWORKS flow simulation is incapable of calculating phase change heat transfer; however, the results are still of utility both for the pressure drop and to perform relative comparisons of the designs. Once a particular configuration has been down-selected, a more comprehensive (and much more time consuming) analysis can be performed that includes the phase change heat transfer. This can be done, for example, with FLUENT.

## Inlet and Outlet Boundary Conditions

For these simulations, all shell walls were assumed to be real with friction (zero slip velocity) but adiabatic. Thus, only the heat transfer from the tubes was calculated. This not only saves computational time, but also provides a lower bound for the heat removal rate from the flue gas. The baffle plates were also assumed to be adiabatic but real with friction. To simulate the flue gas, humid air at a temperature of 45°C, a relative humidity of 100%, and a flow rate of 0.218 kg/s was used, since these are the conditions that will be used in experimental validation and are very close to the composition of the actual flue gas. The temperature and relative humidity conditions are required for the flue gas to condense on the thermosyphon tube walls. This temperature is considerably cooler than the exhaust temperature of a traditional power plant, so some upstream cooling is required before delivering the flue gas to the heat exchanger for condensation. At the exit face of the computational domain, the pressure was assumed to be atmospheric minus 1" (250 Pa) of water, or about 101 kPa.

## Setup

Several versions of the 3-D drawing shown in Figure 1 were set up in SOLIDWORKS for flow simulation: two versions each for the 4-baffle design and 3-baffle design with 1" x 1" square holes, and one version of the 3-baffle design with 1" round holes. The version labeled "Base Design" (see Figure 1) includes 4 baffles and 1" square holes. Drawings of other versions are shown in Figure 2 (4-baffles-modified), Figure 3 (3-baffles), and Figure 4 (3-baffles-modified). Only the version labeled 3-baffles-Round Hole has 1" round holes in the baffle plates.

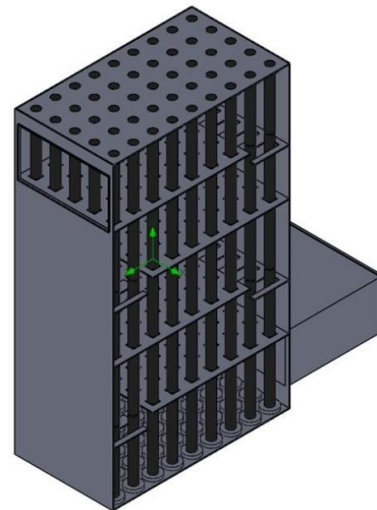
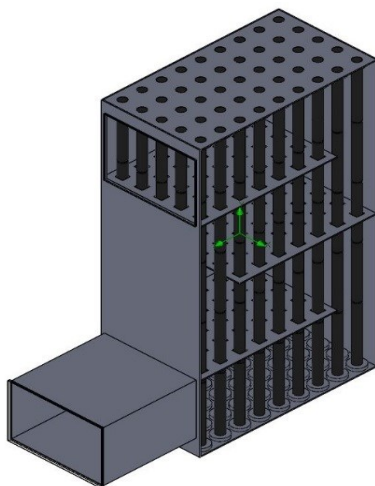
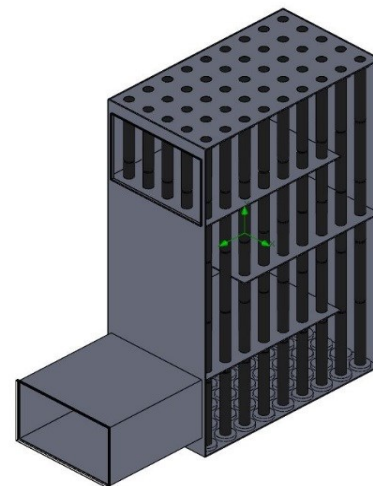


Figure 2. A 3-D rendering of the DEWCOOL shell-and-tube heat exchanger for the 4-baffle modified design configuration.



(a) 3-baffle design with square holes.



(b) 3-baffle design with round holes.

Figure 3. 3-D renderings of the DEWCOOL shell-and-tube heat exchanger for the 3-baffle design.

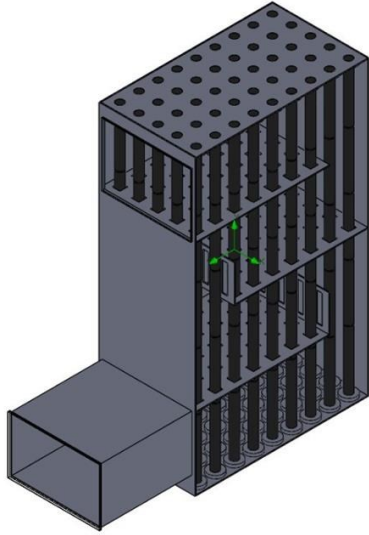


Figure 4. A 3-D rendering of the DEWCOOL shell-and-tube heat exchanger for the 3-baffle modified (with square holes) design configuration.

## Results and Discussion

Table 1 provides a summary of the results for the pressure drop and overall heat removal rate for all of the design options.

### Four-Baffle Designs

Figure 5 and 6 shows the flow trajectories for the 4-baffle base design. The color code indicates the total magnitude of the velocity vector. It should also be noted that, because of 1" square holes in the baffle plates, some of the fluid can be seen crossing the baffle plates directly. As can be clearly seen, the velocity distribution below the baffles is highly non-uniform after the flow undergoes a 180° turn. These figures show that a large fraction of the surface area for

most tubes is only minimally participating in heat transfer, due to very low flow velocities surrounding the tubes in these regions. This can also be seen from the contour plots of velocity at several horizontal planes below and above the baffle plates shown in Figures 7-9.

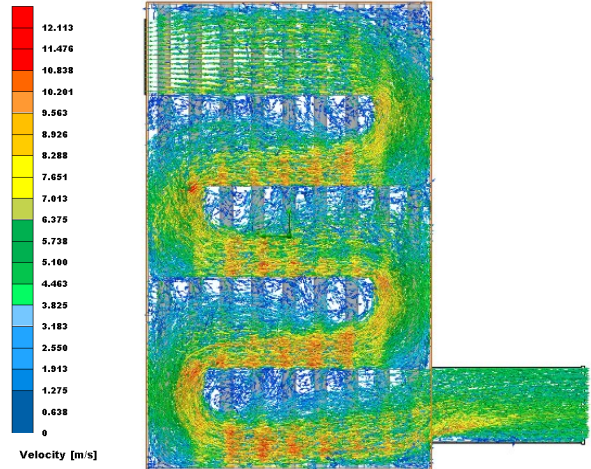


Figure 5. Flow trajectories for the 4-baffle base design.

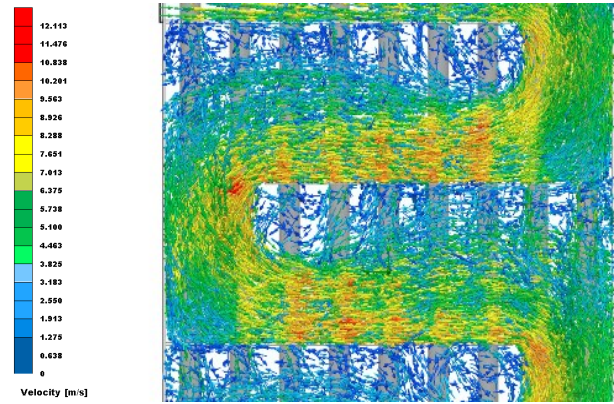


Figure 6. A Close-up of the flow trajectories for the 4-baffle base design.

Table 1. Simulation summary of the overall pressure drop and heat removal rate for various design configurations of the DEWCOOL heat exchanger unit.

Baffle Design	Pressure Drop (Pa)	Heat Removal Rate (W)	Comments
4-Baffle Base Design	254	4030	Base Design
4-baffles Modified Design	475	4230	Undesirable. Pressure drop too large with minimal heat transfer increase.
3-Baffle Design	160	3560	Base Case
3-Baffle Modified Design	162	3230	Undesirable. Lower heat transfer.
3-Baffle Design with Round Holes (no leakage)	195	3790	Higher heat transfer rate with modest increase in pressure drop.

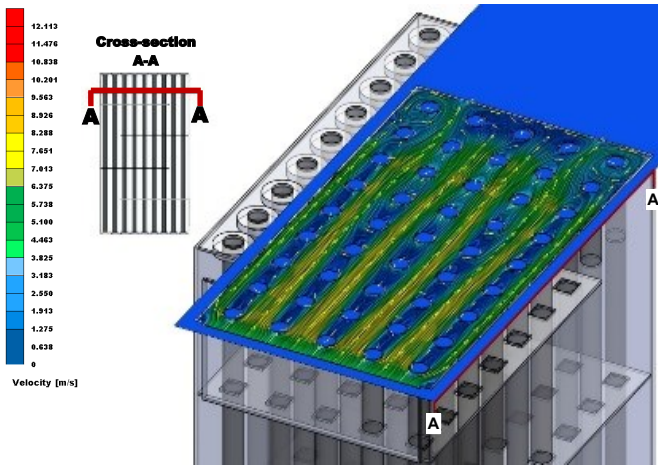


Figure 7. A contour plot of velocity vectors at section A-A above the top baffle adjacent to the inlet.

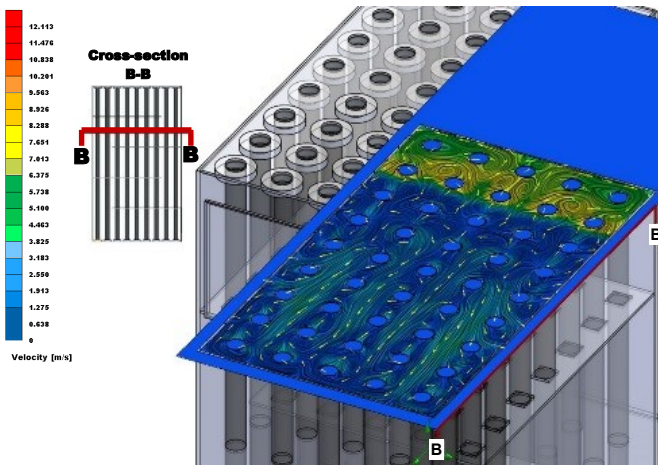


Figure 8. A contour plot of velocity vectors at section B-B below the top baffle.

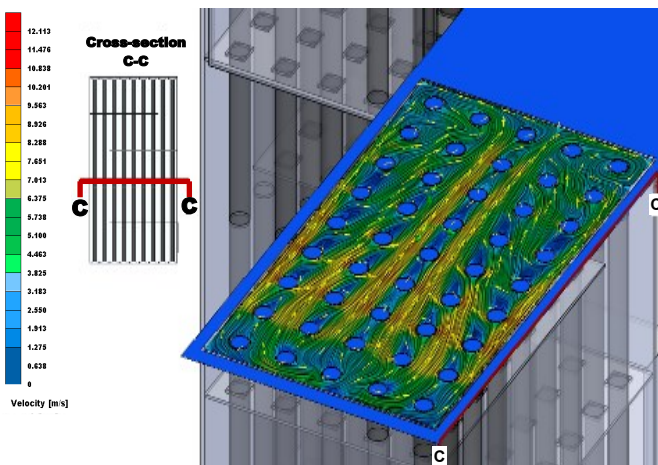


Figure 9. A contour plot of velocity vectors at section C-C above the second baffle from the bottom.

Based upon these results, an attempt was made to improve the heat transfer rate by deflecting some of the air-flow upwards as it is making a U-turn. Figure 2 shows how this was done by adding short baffles in the region just after the flow turns downward for the next section. The intent was that additional baffles would re-direct the flow and produce a jet effect that would force some of the flow to the upper regions of the tube. Figures 10 and 11 shows the flow trajectories for this design. A comparison with Figures 5 and 6 for the base design shows, however, that there is little improvement in the uniformity of flow.

The reason appears to be that the fluid prefers to take the path of least resistance between opposite open ends where the baffles terminate. As can be seen from Table 1, there is only 5% improvement in the heat removal rate, whereas there is a substantially larger (87%) increase in pressure drop. Further exploration of this approach was abandoned. Table 1 also shows the pressure drop and convective heat transfer for both 4-baffle designs. CFD flow-trajectory animations for these designs can be found in the work by Drabo (2018). The predicted pressure drop for the base case 4-baffle design was 254 Pa. While this technically satisfies the pressure drop requirement of 250 Pa, if the actual device as built has a slightly higher pressure drop, this would present a problem. A 3-baffle design was, thus, explored as well, with the intent of reducing the pressure drop. Also, any additional baffle modifications to increase heat transfer would likely not increase the pressure drop above the design limit.

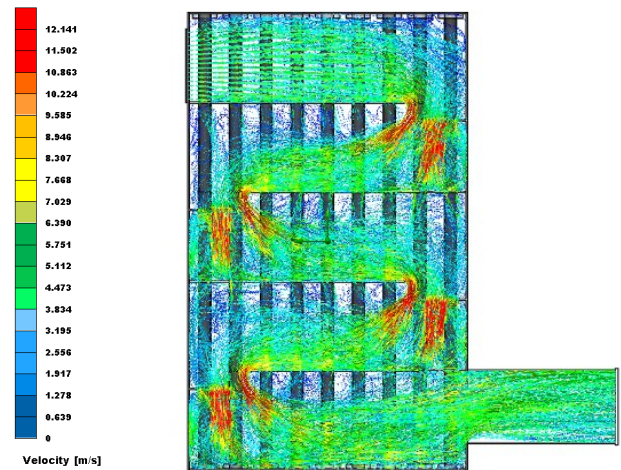


Figure 10. Flow trajectories for the 4-baffle modified design.

### Three-Baffle Designs

With only three baffles, the pressure drop will be reduced. Furthermore, if the pressure drop is reduced enough, it may

be possible to modify the design to yield a better heat removal rate with only a modest increase in pressure drop. The results in Table 2 show that the predicted pressure was only 160 Pa for the 3-baffles design with 1" square holes. However, the heat removal rate dropped to 3560W, as compared to 4030W for the 4-baffles base design.

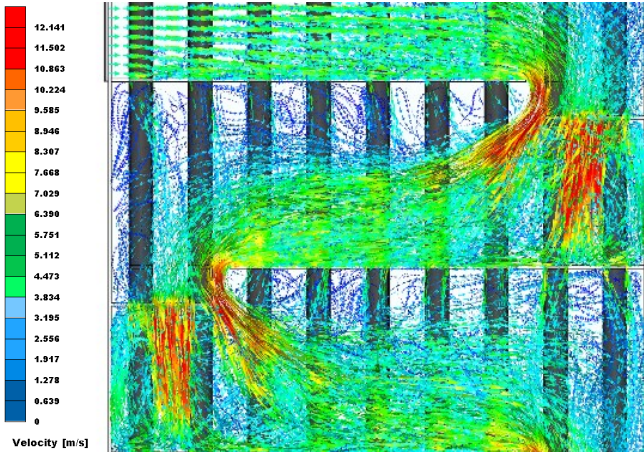


Figure 11. A Close-up of flow trajectories for the 4-baffle modified design.

Figure 12 shows the flow trajectories for the 3-baffle design. Again, as for the 4-baffles design, the flow distribution is highly non-uniform. In an attempt to improve the flow distribution, the bottom two baffles were modified to include a small slotted vertical baffle (see Figure 4) at the end of each baffle. As can be seen from Figure 13, the velocity distribution was more uniform (as compared to Figure 12), but the velocities appear to be lower. However, as seen from Table 2, while the predicted pressure drop was about the same, the heat removal rate was about 9% lower than the 3-baffle base (unmodified) design. This clearly shows the difficulty in improving the design in order to get a better heat transfer rate. With square holes in the baffle plates, fluid leaks from downward and across the baffle plates. This

is likely to result in slightly higher pressure just below the baffles, as compared to the case where baffles had 1" round holes. Therefore, it was suspected that this may be another contributing factor for the lower flow velocities below the baffles. In order to see improvement, if any, by eliminating this cause, the 3-baffle design with 1" round holes was simulated next. Table 2 shows that the heat transfer rate improved by 6.6%. However, this comes at a cost of a 22% increase in pressure drop. Figures 14(a) and (b) show a comparison of flow trajectories for the 3-baffle design with square and round holes. As can be seen from this figure, the flow distribution is a little better and flow velocities are a little higher for the design with round baffle holes. See Drabo (2018) for the CFD animation.

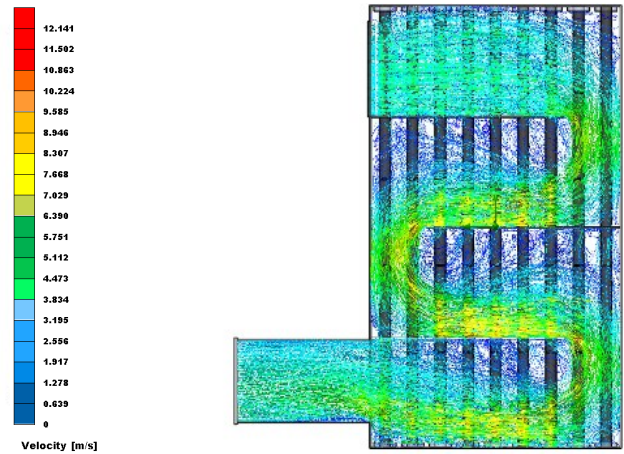


Figure 12. Flow trajectories for the 3-baffle design with 1" square holes in the baffle plates.

## Comparison to Literature Correlations

Interestingly, the CFD analysis showed a significantly lower predicted pressure drop compared to two popular configurations from the literature. Correlations in the literature

Table 2. Simulation summary of overall pressure drop and heat removal rate for various design configurations of the DEWCOOL heat exchanger unit.

Baffle Design	Pressure Drop (Pa)	Heat Removal Rate (W)	Comments
4-Baffle Base Design	254	4030	Base Design
4-Baffle Modified Design	475	4230	Undesirable. Pressure drop too large with minimal heat transfer increase.
3-Baffle Design	160	3560	Base Case
3-Baffle Modified Design	162	3230	Undesirable. Lower heat transfer.
3-Baffle Design with Round Holes (no leakage)	195	3790	Higher heat transfer rate with modest increase in pressure drop.

are almost always in support of the round shell-and-tube heat exchangers. To adapt these correlations to the rectangular geometry used in this current study, the equivalent hydraulic diameter and fraction of exposed baffles were used. Table 3 shows that, for both the 4-baffle and 3-baffle cases, the estimated pressure drop was only 60-80% of that predicted from the correlations. The discrepancy in the results is reasonable, given the approximations made in adapting the round correlations to a rectangular geometry.

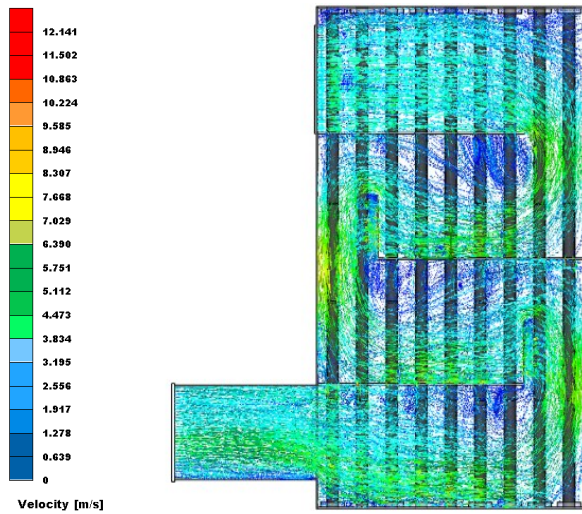


Figure 13. Flow trajectories for the 3-baffle modified design with 1" square holes in the baffle plates.

Table 3. Comparison of CFD predictions and literature correlations for the overall pressure drop for two design configurations of the DEWCOOL heat exchanger unit.

	CFD	CORRELATIONS	
	$\Delta P(\text{Pa})$ CFD	$\Delta P(\text{Pa})^*$	$\Delta P(\text{Pa})^{**}$
4-baffle Original Design	254	315	415
3-baffle Original Design	160	183	236

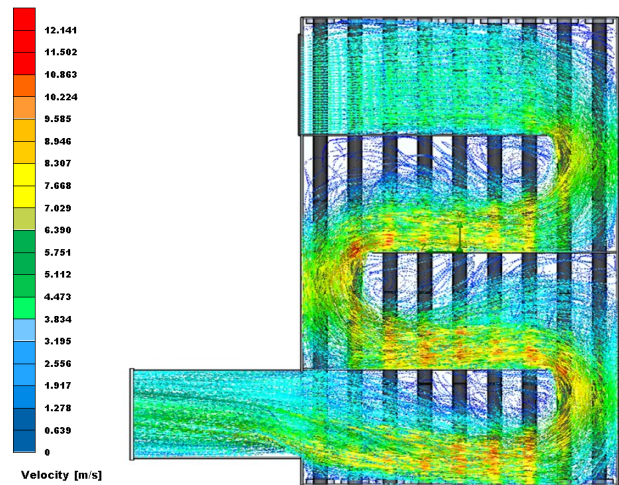
\* Gaddis, & Gnielinski (1997)

\*\* Bell (1981)

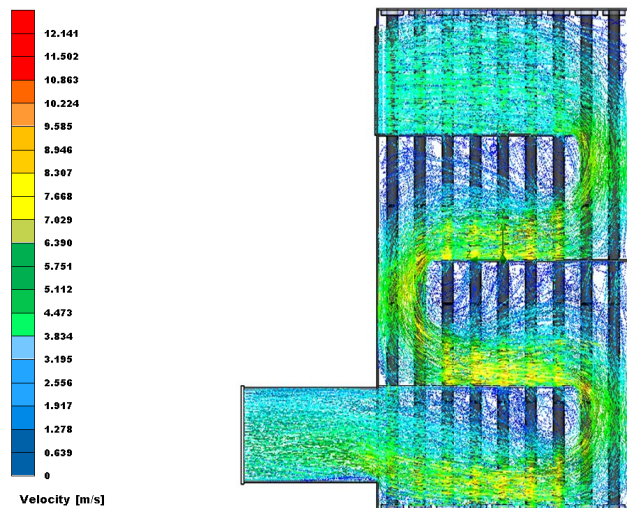
## Conclusions

A CFD simulation of a rectangular baffled, cross-flow heat exchanger was performed in order to simulate sensible heat transfer and pressure drop through the system. The purpose of the heat exchanger was to extract water from the combustion flue gas of a boiler or similar combustion device. The simulations were performed using SOLIDWORKS with embedded SOLIDWORKS Flow Simulation

module. Both 3-baffle and 4-baffle designs were explored, with the tradeoffs between heat transfer and pressure explored. CFD simulations showed that the use of baffles leads to highly non-uniform velocity distribution below the baffles. As a result, significant portions of many tubes experience very low heat transfer rates because of local flow starvation in these regions. The simulations provide insight for design modification purposes. Two baffle modifications were attempted to improve the heat transfer, but the results were inconclusive. Further opportunities for study in this regard include experimental validation of test cases, which are in progress, and the development of correlations for pressure drop and heat transfer for rectangular geometries based on both modeling and empirical measurements.



(a) 3-baffle designs with 1" round holes.



(b) 3-baffle design with 1" x 1" square holes in the baffle plates.

Figure 14. Flow trajectories for the 3-baffle designs.

---

## References

- Bell, K. J. (1981). Delaware method for shell side design. In S. Kakac, A. E. Bergles, & F. Mayinger (Eds.). *Heat exchanger: Thermal-hydraulic fundamentals and design* (pp. 581-618). New York: Hemisphere.
- Bhutta, M. M. A., Hayat, N., Bashir, M. H., Khan, A. R., Ahmad, K. N., & Khan, S. (2012). CFD applications in various heat exchangers design: A review. *Applied Thermal Engineering*, 32, 1-12.
- Gaddis, E. S., & Gnielinski, V. (1997). Pressure drop on the shell side of shell-and-tube heat exchangers with segmental baffles. *Chemical Engineering and Processing*, 36(2), 149-159.
- He, Y. L., Tao, W. Q., Deng, B., Li, X., & Wu, Y. (2005, September). Numerical simulation and experimental study of flow and heat transfer characteristics of shell side fluid in shell-and-tube heat exchangers. *Proceedings of the Fifth International Conference on Enhanced, Compact and Ultra-Compact Heat Exchangers: Science, Engineering and Technology*. Brooklyn, NY: Engineering Conferences International.
- Özden, E., & Tari, I. (2010). Shell side CFD analysis of a small shell-and-tube heat exchanger. *Energy Conversion and Management*, 51(5), 1004-1014.

## Biographies

**MEBOUGNA DRABO** is an associate professor of mechanical engineering at Alabama A&M University. His research interests include advanced flash atomization technology, burner/atomizer integration, material characterization, multi fuel optimization, biofuels, computational fluid dynamics analysis, heat transfer, and advanced combustion IC engine concepts. Dr. Drabo may be reached at [mebougna.drabo@aamu.edu](mailto:mebougna.drabo@aamu.edu)

**TAO HE** is a PhD candidate in mechanical engineering at Stony Brook University. He received his BS degree from Harbin Engineering University, China, in 2010. His research interests include thermosyphons in cooling applications, advanced heat transfer, renewable and clean energy, and computational fluid dynamics and heat transfer. Mr. He may be reached at [heluis880203@hotmail.com](mailto:heluis880203@hotmail.com)

**WEI ZHONG** is a Ph.D student in mechanical engineering at Stony Brook University. He received his BEng degree in thermal energy and power engineering from the Beijing Institute of Technology in 2013. His current research interests include thermosyphons and phase change heat transfer. Mr. Zhong may be reached at [wei.zhong@stonybrook.edu](mailto:wei.zhong@stonybrook.edu)

**JON P. LONGTIN** joined the Mechanical Engineering Faculty at Stony Brook University in 1996. He came to Stony Brook after receiving his PhD degree in 1995 from U.C. Berkeley, followed by a one-year postdoc at the Tokyo Institute of Technology in Japan. His research interests include energy conservation, innovative energy transfer and storage, and energy monitoring and diagnostics, as well as laser materials processing, particularly with ultrafast lasers and the development of sensors for harsh environments. His research has been funded by NSF, DOE, DOD, NASA, NYSERDA, and a variety of industrial sources. He is the author of over 130 technical publications and holds 10 issued and pending patents. He has received the Presidential Early Career Award for Scientists and Engineers, two Excellence in Teaching Awards, and an R&D 100 award. He is a licensed Professional Engineer in New York State and serves as a technical advisor to a variety of companies and non-profit organizations. Dr. Longtin may be reached at [jon.longtin@stonybrook.edu](mailto:jon.longtin@stonybrook.edu)

**THOMAS BUTCHER** is the deputy chair of the Sustainable Energy Technologies Department and leader of the Energy Conversion Group. Work within this group includes liquid fuel combustion and oil-fired heating system efficiency, biofuels applications, polymer composite heat exchangers, solar thermal systems, micro-combined heat and power concepts, absorption heat pumps, wood boiler emissions and efficiency, and advanced materials for geothermal energy applications. Dr. Butcher may be reached at [butcher@bnl.gov](mailto:butcher@bnl.gov)

**NARINDER K. TUTU** is a guest scientist at the Brookhaven National Laboratory (BNL), who retired from the BNL after about 27 years of research. His areas of interest include instrumentation in the fields of fluid dynamics, multiphase flows, heat transfer, two-phase flow and transient heat transfer in porous media, safety studies of severe nuclear reactor accident scenarios, and energy conservation in buildings. Dr. Tutu may be reached at [tutu@bnl.gov](mailto:tutu@bnl.gov)

**REBECCA TROJANOWSKI** received her BS in chemical engineering and MS in mechanical engineering from Worcester Polytechnic Institute and is now working towards her EngScD at Columbia University in the Earth and Environmental Engineering Department. She is an associate staff engineer in the Energy Conversion Group at Brookhaven National Laboratory. Her research interests include technical solutions to advance building energy systems, fossil fuel reduction, and emissions. Some of her research and development areas include advanced HVAC concepts, biofuels, solid fuels, air pollution, and combustion and system concepts. Ms. Trojanowski may be reached at [rtrojanowski@bnl.gov](mailto:rtrojanowski@bnl.gov)

# OPTIMAL DESIGN OF AN AUTOMOTIVE REAR AXLE HOUSING

Diane L. Peters, Kettering University; Yaomin Dong, Kettering University; Vimal Patel, Kettering University

## Abstract

In this paper, the authors describe the optimization of a rear axle housing for a 2013 Ford Mustang Shelby GT500. This optimization was conducted using the optimization and FEA capabilities of NXTM, the product development solution from Siemens PLM software, with the objective of minimizing the weight, subject to constraints on the maximum stress in the housing. The optimization was conducted twice, once with a single design variable and once with five design variables. In both cases, the optimization problem converged to an optimal design, and the weight was reduced. In the first case, the weight of the housing was reduced by 15%; in the second case, it was reduced by 47%. These reductions could be expected to have a large impact on fuel economy and performance of the vehicle.

## Introduction

As fuel economy requirements become more demanding, decreasing the weight of vehicles is critical. However, at the same time, it is necessary to meet performance requirements and manufacturability constraints. The configuration of some components may be the result of past decisions that were appropriate at the time; but, as other aspects of the vehicle change, technology improves, and new analysis techniques are developed, these legacy parts are good candidates for re-design. Axles are critical to a vehicle, as they support its weight, and producing an optimal axle design is important. In this study, a specific axle was considered: the 8.8-inch rear axle center housing from a 2013 Ford Mustang Shelby GT500. This axle was optimized for minimum weight, subject to a set of constraints based on the performance requirements for the axle, with the optimization carried out within the NX software. In this paper, the authors will present the background for this project, including a discussion of the general design of automotive axles as well as some previous design and optimization work regarding axles. Also given will be the specific problem formulation and the results of the optimization.

## Background

Automotive axles are a critical part of vehicles. The axles may be fixed to the wheels and rotating with them (live axle) or fixed to the vehicle with the wheels rotating about the

axle. In a live-axle suspension system, axles both transmit driving torque and maintain the position of the wheels relative to each other and to the body of the vehicle. The axles also bear the weight of the vehicle and cargo. Non-driven axles, in contrast, serve only as a suspension and steering component. Vehicles typically have axles in both the front and rear; in a rear-wheel-drive vehicle, the rear axle assembly is a driven or live axle, while in front-wheel-drive vehicles, the rear axle is a non-driven axle. In the case where a vehicle has a driven rear axle, the housing contains and supports other parts of the axle assembly and forms a reservoir for the lubricant. This housing consists of a central housing with axle tubes and is attached to the vehicle body through a suspension that involves springs, shock absorbers, and control arms (Chris & James, 2010).

There are a number of variations on the basic rear axle housing. The housing may have a removable carrier or an integral carrier and may be semi-floating, three-quarter floating, or full-floating. A typical semi-floating axle has a half shaft connected directly to the wheel hub, with the outer end supported by a bearing inside the axle casing (Kaven, 2015). In the case of the three-quarter floating axle, the wheel hub is supported by a single bearing in the center of the hub, and the wheel hub runs on an axle housing, with the axle shaft keyed to the hub (Kaven, 2015). Finally, the full-floating axle features a wheel hub supported by two bearings, running directly on the axle housing, with the axle shaft fastened to the wheel hub flange through a coupling (Kaven, 2015). In this current study, the axle considered was a full-floating axle, similar to that described in "The Ford Explorer 8.8-Inch Rear Axle" (n.d.).

Optimization has been applied to many different aspects of vehicle design at different scales, including both entire vehicles (Kokkolaras et al., 2004) and components and sub-systems of vehicles. These studies have included powertrains and power management (Filipi et al., 2004), active suspensions (Frühaufl, Kasper, & Lückel, 1986; Fathy, Papalambros, Ulsoy, & Hrovat, 2003), passive suspension systems (Chatillon, Jezequel, Coutant, & Baggio, 2006), and axles (Yimin, Xiangdong, & Qiaoling, 2002; Bin, Qinghong, Rui, & Yanping, 2005). In a study by Bin et al. (2005), a mass reduction of 4.2 kg was achieved, corresponding to a weight reduction of 41.2N. An optimization of the axle could be done in several ways: as sizing, shape, or topology. In this case, the problem is formulated as a

sizing optimization, since this reduces the complexity of the problem. In applying optimization to the automotive axle, a simplified model can be used with analytical equations, or a more complex, “black box” optimization can be performed using FEA software or other complex, higher fidelity models. In this current study, the latter approach was used, similar to the application by Bin et al. (2005).

## Problem Formulation

The optimization of the housing was carried out using the advanced simulation application of Siemens NX 11 with a NASTRAN solver. The rear axle housing was modeled with the material specified as grey cast iron. The material properties, listed in Table 1, were incorporated into NX and used in this study. Figure 1 shows the sequence of processes used for conducting the optimization process.

Table 1. Material properties used for grey cast iron (G60).

Property	Value
Young’s Modulus	158 GPa
Poisson’s Ratio	0.28
Bulk Modulus	83333 MPa
Shear Modulus	42969 MPa
Isotropic Relative Permeability	10000
Compressive Ultimate Strength	382 MPa
Tensile Ultimate Strength	632 MPa

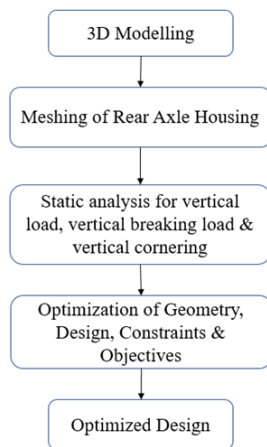


Figure 1. Process methodology for optimization (Patel, 2017). Reprinted with permission.

Figure 2 shows the 3D model of the housing, prior to optimization.

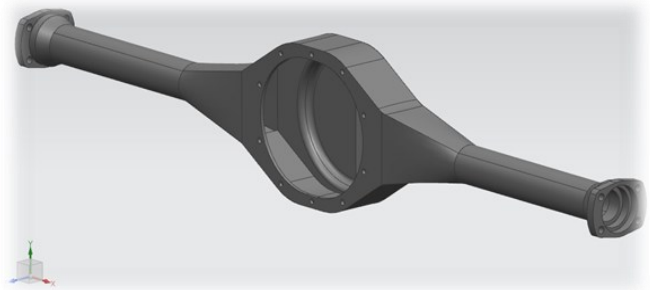


Figure 2. CAD model of the semi-floating solid rear axle housing (Patel, 2017). Reprinted with permission.

The optimization was formulated to minimize weight, subject to constraints on deflection and stress, with the weight, deflection, and stress determined using CAD software and FEA analysis. A single design variable was chosen that would impact the entire design, based on the geometric relationships within the axle housing. Figure 3 shows the control sketch for the optimization.

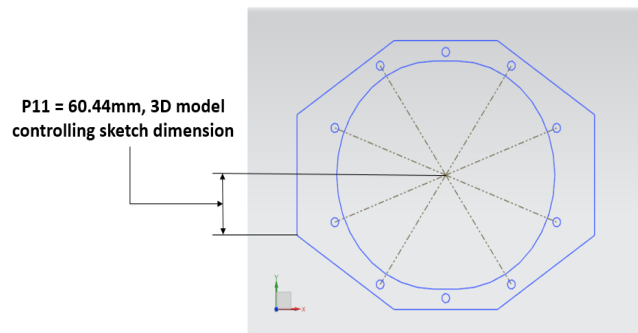


Figure 3. Control sketch for the rear axle housing (Patel, 2017). Reprinted with permission.

In the initial optimization, the sole design variable was the dimension  $p11$ ; the problem, then, can be formulated in standard negative-null form, as given in Equation 1, with the upper and lower limits on  $p11$  chosen based on manufacturing considerations. In a second optimization problem, the shell thickness and the chamfer over the center of the differential housing were also varied. No other changes were made to the optimization problem for the second optimization.

$$\begin{aligned}
 & \min_{p11} \text{AxleWeight} \\
 & p11 \in \{55 \text{ mm} \leq p11 \leq 65 \text{ mm}\} \\
 & \text{subject to:} \\
 & \text{MaxStress} - \text{StressLimit} \leq 0 \\
 & \text{MaxDeflection} - \text{DeflectionLimit} \leq 0
 \end{aligned} \tag{1}$$

In the full range of vehicle operation, the maximum stresses that the housing should withstand include the following (Saxena, 2014):

- Torsional stress due to driving and braking torque
- Shear and bending stresses due to the weight of the vehicle
- Tensile and compressive stresses due to cornering forces

This optimization was carried out as a static optimization, with calculations performed to determine what static loads would correspond to the driving and braking torque, and to the effects of cornering. In calculating the stress and deflection, certain assumptions must be made about the vehicle and its weight distribution. It was assumed that the curb weight of the vehicle was 3850 lb., that the EPA test weight of 300 lb. was used, and that the weight distribution was such that the front axle carried 57% of the total weight and the rear axle carried 43% (Data, 2012). It was further assumed that the full vehicle weight load was applied at the spring seat locations, as shown in Figure 4.

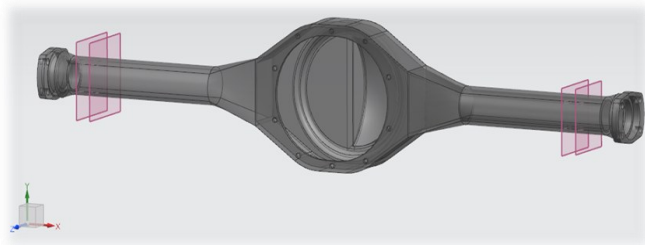


Figure 4. Model of the 8.8-inch rear axle housing showing spring seat location (Patel, 2017). Reprinted with permission.

To determine the effects of driving and braking forces, several intermediate calculations were necessary. The effective radius of the wheel was calculated, based on the work by Mazzei (2012), using Equation 2:

$$r_{eff} = 0.5 \left( \left( 25.4 \frac{\text{mm}}{\text{in}} \right) (20 \text{ in}) + 0.02 (35) (285) \right) - 4 \text{ mm} = 349.75 \text{ mm} \quad (2)$$

The frictional force between the car and the road also had to be calculated. To perform this calculation, it was assumed that, under normal driving conditions, each tire would support half of the load applied to the rear axle. Assuming a coefficient of friction  $\mu = 0.85$  between the road and the tire (Davis & Hoff, 2003), the frictional force on each tire could be calculated using Equation 3:

$$F_{fric} = \mu \left( \frac{0.43W}{2} \right) = 758.4 \text{ lb} \quad (3373.6 \text{ N}) \quad (3)$$

This frictional force produces both a torque about the axle, based on the effective radius of the wheel, and a bending moment at the center of the outboard bearing. The torque is given by Equation 4:

$$\tau = F_{fric} r_{eff} = (3373.6 \text{ N})(349.75 \text{ mm}) = 1179.9 \text{ N}\cdot\text{m} \quad (4)$$

and the bending moment is given by Equation 5:

$$M = F_{fric} l \quad (5)$$

where,  $l$  is the distance between the center planes of the road wheel and the outboard bearing of the axle.

For this particular vehicle, that dimension was 3.86 in. (Chevrolet and Ford, 2012-2013), or 98.044 mm, resulting in a bending moment of 330.8 N-m. These two loads were assumed to be present at all times. During a sudden braking event, additional loads are present. In its top gear, the 2013 Ford Mustang GT500 produces a maximum torque of 855.5 N-m at 4000 rpm (Data, 2012), and the driveline efficiency and clutch efficiency are both assumed to be 90% (Davis & Hoff, 2003). When the vehicle is traveling straight, it is assumed that it will be traveling at 60 mph (26.82 m/s) and will have a stopping distance of 20m. If the acceleration is constant during this braking event, then the stopping time and acceleration can be calculated using basic kinematic equations of Equations 6 and 7:

$$t = \frac{2(x_f - x_0)}{v_f + v_0} = \frac{2(20 \text{ m})}{0 \text{ m/s} + 26.82 \text{ m/s}} = 1.49 \text{ s} \quad (6)$$

$$a = \frac{v_f^2 - v_0^2}{2(x_f - x_0)} = \frac{-(26.82 \text{ m/s})^2}{2(20 \text{ m})} = -17.98 \text{ m/s}^2 \quad (7)$$

The force required to produce this acceleration can be calculated, after which the torque can be found, based on the perpendicular distance from the center of the differential housing to the end of the side flange, using Equations 8 and 9:

$$F_{stop} = (809.44 \text{ kg})(-17.98 \text{ m/s}^2) = -14560 \text{ N} \quad (8)$$

$$\tau_{stop} = (-14560 \text{ N})(0.662 \text{ m}) = -9636 \text{ N}\cdot\text{m} \quad (9)$$

This loading is also considered in the total loading of the axle housing for the optimization. When the vehicle is cornering, it is assumed that the lateral acceleration for the cornering maneuver is 0.95g, and the vertical height of the center of gravity is 24.2 in. The track width, according to Kaven (2015), at the rear end of the vehicle is 62.5. The cornering force is given by Equation 10 (Data, 2012):

$$F_{corner} = 0.43W g_c \left( 0.5 + g_c \frac{h_{vt}}{b_r} \right) \quad (10)$$

where,  $W$  is the total weight, including the EPA standard test weight, as previously specified; 0.43 is the portion of the weight on the rear axle;  $g_c$  is the lateral acceleration for cornering;  $h_{vt}$  is the vertical height of the center of gravity of the vehicle, measured from the ground (24.213 in., or 615 mm); and,  $b_r$  is the track width at the rear end of the vehicle.

The cornering force can then be calculated as 1472 lb. or 6548N. The problem was then solved using the NX NAS-TRAN FEA capabilities integrated into NX, using the standard NX optimizer. As indicated in Figure 3, a mesh had to be generated for the FEA solution. In this problem, a 3D tetrahedral mesh was used, with the element type CTETRA. A standard element size was used for the entire optimization; to ensure that the initial element size selected was sufficiently small, the recommended element size from the software was divided by two, resulting in a mesh element size of 7.25 mm. Figure 5 shows this meshing.

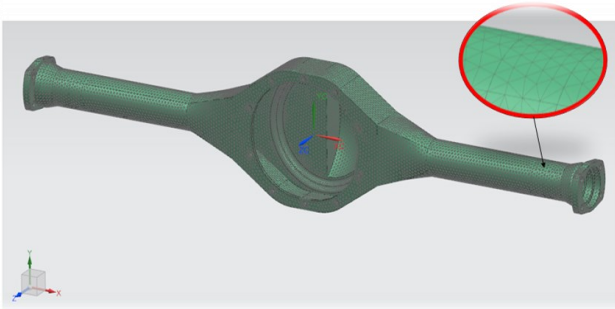


Figure 5. Visualization of 3D tetrahedral mesh size (Patel, 2017). Reprinted with permission.

Prior to performing the optimization, a standard structural analysis was performed to validate the finite element model (mesh type and size, constraints, loads, etc.), and to obtain the baseline results of structural responses (stresses, deformation, etc.). Figures 6 and 7 show the results of this simulation, with Figure 6 showing the displacement and Figure 7 showing the von Mises stress.

## Results

The optimization was then performed using “Advanced Solution Process” based on the aforementioned “baseline” analysis. Both optimization problems did converge to feasible solutions. In the first case, the problem converged quickly, after only three iterations; in the second optimization, the problem took seven iterations to converge.

## First Optimization

When the first optimization was performed, with only  $p11$  as the design variable, the optimization converged after three iterations, as shown in Figure 8, with  $p11$  taking on its minimum value of 55 mm.

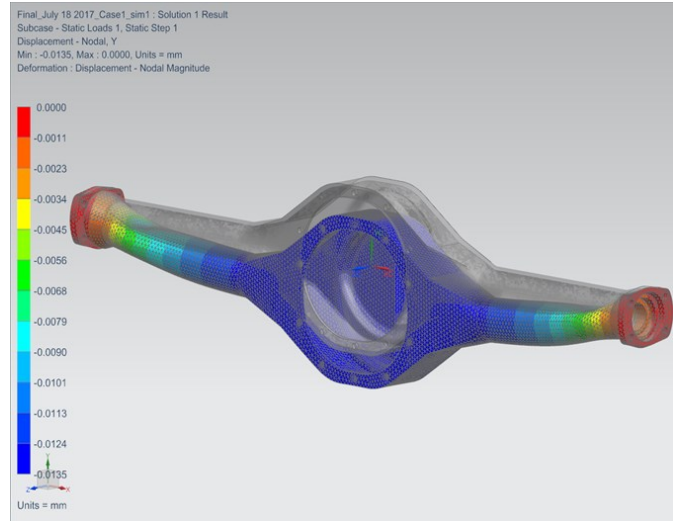


Figure 6. Deflection of the original design (Patel, 2017). Reprinted with permission.

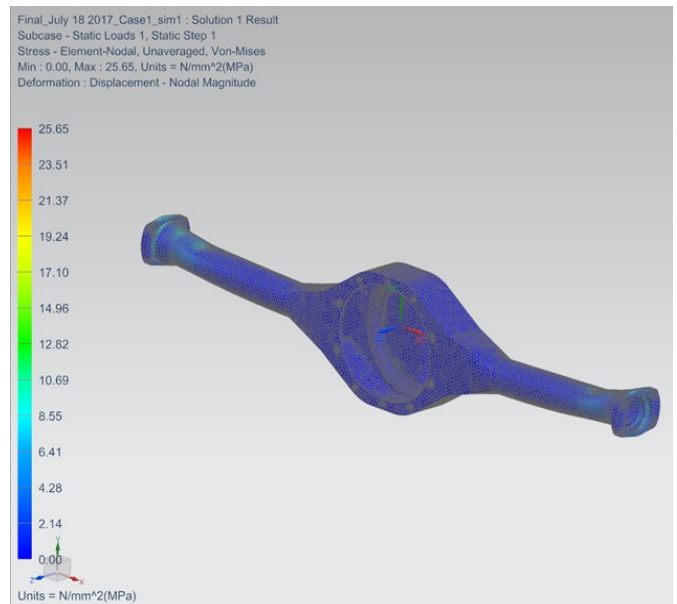


Figure 7. Stress profile of the original design (Patel, 2017). Reprinted with permission.

The initial design was feasible, as the maximum stress of 25.65 MPa was well below the yield stress of the material.

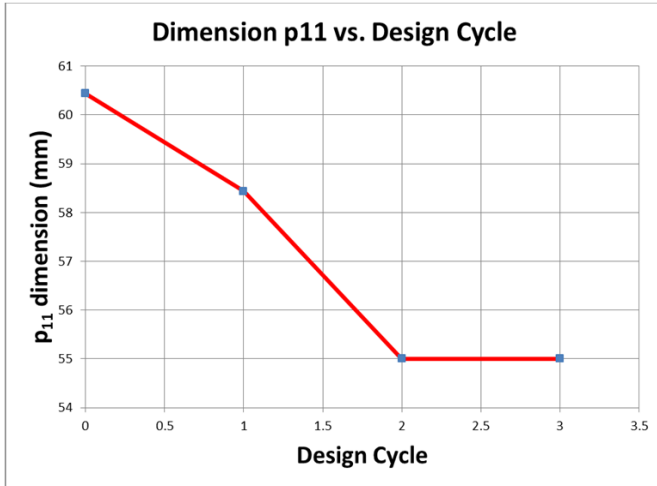


Figure 8. Convergence of the first optimization (Patel, 2017). Reprinted with permission.

The initial weight of the rear axle housing was 187.8N, with the final weight at 160.4N, representing a 15% reduction. Figure 9 shows the new design, while Figure 10 shows the decrease in weight with changes in  $p_{11}$ .

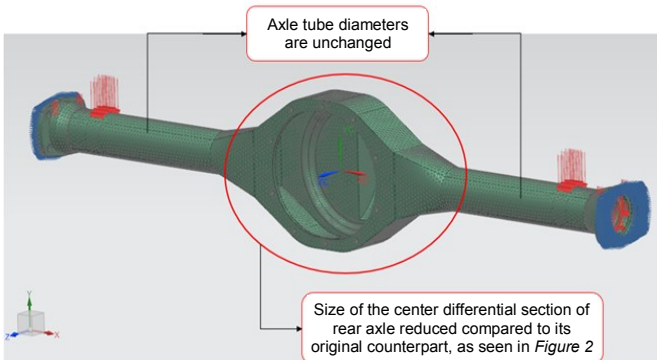


Figure 9. Design resulting from the first optimization (Patel, 2017). Reprinted with permission.

Note that the optimization converged when the dimension  $p_{11}$  was at its lower bound and that none of the stress constraints or deflection constraints were active. This suggests that there is still an opportunity to improve the design further, if doing so would produce a manufacturable design.

## Second Optimization

Figure 11 shows that there were five design variables for the second optimization. The optimization converged after seven iterations, with the final values given in Table 2 and the progress towards optimality shown in Figure 12. The maximum stress constraint was active for this solution.

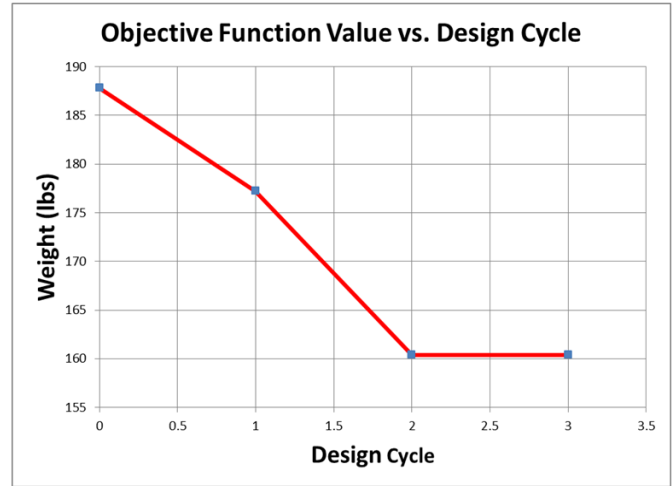


Figure 10. Decrease in weight for the first optimization (Patel, 2017). Reprinted with permission.

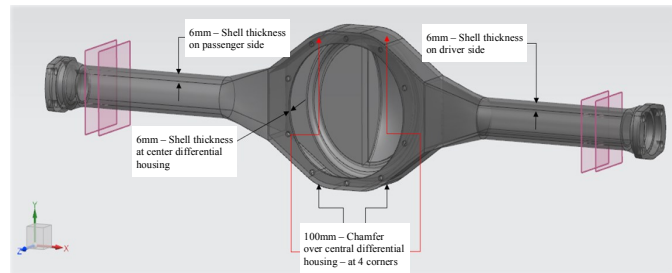


Figure 11. Design variables for the second optimization.

Table 2. Results of the second optimization.

	Initial Value	Final Value
<b>Design Objective Function Results</b>		
Minimum Weight [N]	186.52	98.7
<b>Design Variable Results</b>		
Control sketch dimension, $p_{11}$	60.44	55.03
Shell thickness of the center differential housing	6	3
Shell thickness of the right axle tube	6	3
Shell thickness of the left axle tube	6	3
Chamfer over the center differential housing	100	109.8

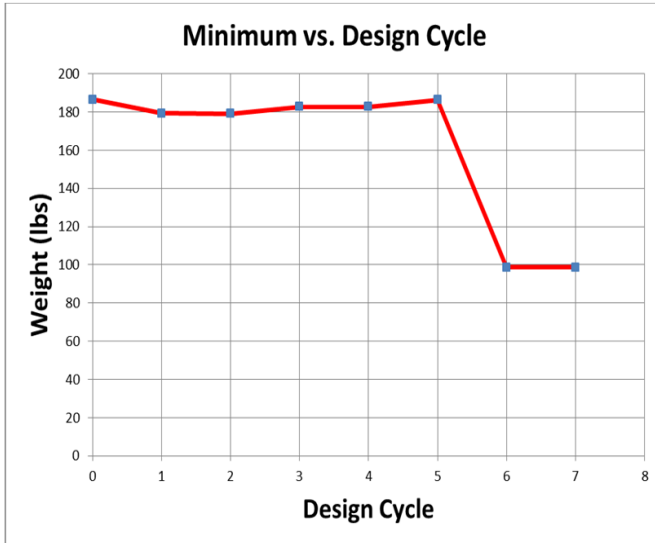


Figure 12. Convergence of the second optimization (Patel, 2017). Reprinted with permission.

Figure 13 shows the new design of the axle. There are noticeable differences between this design and the design of the first optimization (see again Figure 9). The dimension  $p_{11}$  still takes on the value of its lower bound; however, the shell thicknesses were also decreased to their lower bounds, and the chamfer on the housing increased slightly. The chamfer size was not at an upper or lower bound for the problem. Note that the new weight of the housing is 98.7N, as opposed to the weight of 160.4N found in the first optimization. This represents a reduction of 87.8N from the original weight, or 47%. This is a significant reduction, which can be expected to have a large impact on vehicle dynamics and fuel economy.

## Conclusions

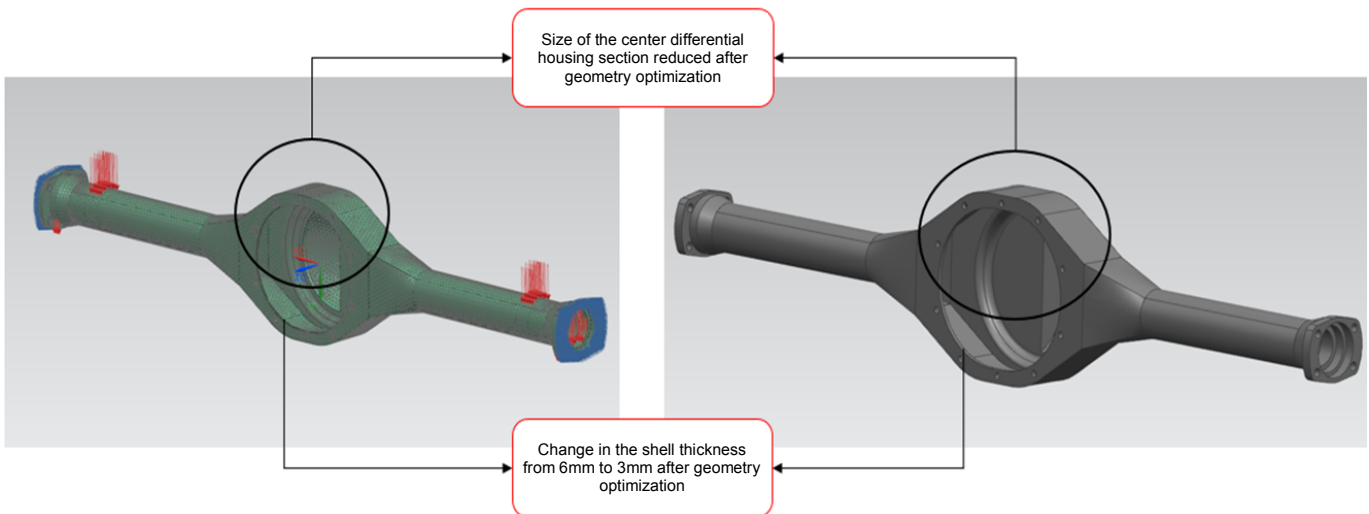
In this study, the authors formulated and solved for the optimization of a rear axle for a 2013 Ford Mustang Shelby GT500. This optimization showed that, by varying a single design variable, a 15% weight reduction could be achieved, while still satisfying constraints on the axle. Increasing the number of design variables allowed for a greater weight reduction (47%) compared to the original weight. This weight reduction can be expected to have a substantial impact on fuel economy; simulations of the vehicle's performance with the reduction in weight were carried out and reported by Patel (2017).

Future work should, at a minimum, include the dynamic conditions of cornering and braking, as they have a substantial impact on the problem. The optimization could also include the use of different materials, such as various steel alloys and composite materials, and could include a non-uniform material composition. Additional work could be done by optimizing the axle along with other components in a system-level problem formulation. Finally, the results of the optimization could be prototyped and physical tests conducted in order to verify that the solution found actually performs as intended.

## Acknowledgments

The authors would like to thank the Graduate School of Kettering University for providing the graduate assistantships during this work, and Dr. Arnaldo Mazzei for serving as a committee member of the graduate student's research.

Figure 13. Optimization results for optimization #2 (Patel, 2017). Reprinted with permission.



---

## References

- Bin, Y., Qinghong, S., Rui, W., & Yanping, Z. (2005). Parameterization-based dynamic optimization design of vehicle drive axle housing. *Automobile Technology*, 5, 6.
- Calculating 9-inch and 8.8-inch axle lengths from a housing. (n.d.). Retrieved from <http://www.hotrodders.com/forum/calculating-9-inch-axle-lengths-housing-141900.html>
- Chatillon, M. M., Jezequel, L., Coutant, P., & Baggio, P. (2006). Hierarchical optimisation of the design parameters of a vehicle suspension system. *Vehicle System Dynamics*, 44(11), 817-839.
- Chevrolet Camaro ZL1 & Ford Mustang Shelby GT500. (2012-2013). *Road and Track*. Retrieved from [http://www.roadandtrack.hearstmobility.com/cm/roadandtrack/data/2012\\_Chevrolet\\_Camaro\\_ZL1\\_vs\\_2013\\_Ford\\_Mustang\\_Shelby\\_GT500\\_data.pdf](http://www.roadandtrack.hearstmobility.com/cm/roadandtrack/data/2012_Chevrolet_Camaro_ZL1_vs_2013_Ford_Mustang_Shelby_GT500_data.pdf)
- Chris, J., & James E, D., (2010). *Manual drivetrains and axles: Rear axle assembly construction and operation*. Tinley Park, IL: The Goodheart-Wilcox Company.
- Data panel archive. (2012). Retrieved from [http://paws.kettering.edu/~amazzei/Road\\_Track.htm](http://paws.kettering.edu/~amazzei/Road_Track.htm)
- Davis, G. & Hoff, C. (2003). *Introduction to automotive powertrain*. Coursepack. Kettering University.
- Fathy, H. K., Papalambros, P. Y., Ulsoy, A. G., & Hrovat, D. (2003). Nested plant/controller optimization with application to combined passive/active automotive suspensions. In *Proceedings of the 2003 American Control Conference*. Piscataway, NJ: IEEE.
- Filipi, Z., Louca, L., Daran, B., Lin, C. C., Yildir, U., Wu, B., Kokkolaras, M., Assanis, D., Peng, H. Papalambros, P. Y., Stein, J., Szubiel, D., & Chapp, R. (2004). Combined optimisation of design and power management of the hydraulic hybrid propulsion system for the 6× 6 medium truck. *International Journal of Heavy Vehicle Systems*, 11(3-4), 372-402.
- The Ford Explorer 8.8-inch rear axle—Swap. (n.d.). Retrieved from [http://www.therangerstation.com/tech\\_library/Explorer8\\_8.shtml](http://www.therangerstation.com/tech_library/Explorer8_8.shtml)
- Frühauf, F., Kasper, R., & Lückel, J. (1986). Design of an active suspension for a passenger vehicle model using input processes with time delays. *Vehicle System Dynamics*, 15(sup1), 126-138.
- Kavin, E. (2015). *Types of live rear axles*. Retrieved from <http://techatmech.blogspot.com/2015/07/types-of-live-rear-axles-semi-floating.html>
- Kokkolaras, M., Louca, L., Delagrammatikas, G., Michelena, N., Filipi, Z., Papalambros, P., Stein, J., & Assanis, D. (2004). Simulation-based optimal design of heavy trucks by model-based decomposition: An extensive analytical target cascading case study. *International Journal of Heavy Vehicle Systems*, 11(3-4), 403-433.
- Mazzei, A. (2012). *Chassis system dynamics, automotive weight distribution*. Lundstorm\_RhoBar\_v15.01. Coursepack. Kettering University.
- Patel, V. B. (2017). *Design, analysis, & optimization of 8.8 inch rear axle differential housing* (Unpublished master's thesis). Kettering University, Flint, MI.
- Saxena, S. (2014, July 29). *Types of axles*. [PowerPoint slides]. Retrieved from <https://www.slideshare.net/sumatisaxena1/types-of-axles>
- Yimin, Z., Xiangdong, H., & Qiaoling, L. (2002). Optimization design of reliability of automobile front-axle. *Automobile Science & Technology*, 166(1), 8-10.

## Biographies

**DIANE L. PETERS** is an assistant professor of mechanical engineering at Kettering University. She is a licensed professional engineer in Illinois and Michigan, a member of ASME and SAE, a senior member of IEEE, and a fellow of SWE. Dr. Peters may be reached at [dpeters@kettering.edu](mailto:dpeters@kettering.edu)

**YAOMIN DONG** is a professor of mechanical engineering at Kettering University. He received his PhD in mechanical engineering at the University of Kentucky in 1998. Dr. Dong has extensive R&D experience in the automotive industry and holds multiple patents. Dr. Dong's areas of expertise include metalforming processes, design with composite materials, computer graphics, computer-aided engineering, and finite element analysis. Dr. Dong may be reached at [ydong@kettering.edu](mailto:ydong@kettering.edu)

**VIMAL PATEL** received his master's degree at Kettering University in 2017. Mr. Patel may be reached at [pate9936@kettering.edu](mailto:pate9936@kettering.edu)

# STABILITY AND TRANSPARENCY IN BILATERAL TELEOPERATION VIA CONTINUOUS POLE PLACEMENT

Theophilus Okore-Hanson, North Carolina A&T State University; Sun Yi, North Carolina A&T State University; Sameer Hamoush, North Carolina A&T State University; Younho Seong, North Carolina A&T State University

## Abstract

Bilateral teleoperation in a remote environment is of great importance in robotics. The desire to reproduce the operator's exact motions at a remote location has been considered by many researchers. It is an area of great interest, as it enables task execution in complex and life-threatening environments. However, transparency and latency remain an open-ended problem. Time delay results in an infinite number of roots with infinite frequencies, making it very complex to design controllers for such systems. Control becomes even more complex when haptic feedback is desired. In this paper, the authors present a method for estimating the parameters of the plant and further designing a controller against disruption, lags, and data losses that deteriorate stability and behavior. They go on to discuss a robust and precise controller design for a bilateral teleoperation system.

## Introduction

Effective teleoperation requires a human to perceive information from a remote Environment, indicating the status of the command that was sent. The techniques in teleoperation involve advanced control and communication knowledge (Tzafestas, Velanas, & Fakiridis, 2008). Areas of teleoperation application include nuclear waste disposal, deep seas, space, surgery, etc. Teleoperation is a human-in-the-loop system, where the human operator conducts tasks in the remote environment using master and slave control. The feedback signal from the slave to the master ensures improved performance in teleoperation as a notification that the command was executed. This can be achieved through visual aids or by reflecting measured force from the slave to the master. Bilateral teleoperation refers to a means of extending human capabilities to remotely manipulate objects, while providing the operator with kinesthetic conditions like those at the remote environment (see Figure 1).

A measured force is reflected from the slave to the master. In previous work, the authors illustrated an adaptive synchronization technique addressing the effects of disturbances and transient responses in a synchronization (Okore-Hanson & Yi, 2016). A method of controller design, robust against the performance-deteriorating effects of the time delay, was presented by Okore-Hanson & Yi (2017). Some

of these techniques were employed in this current study for haptic feedback in teleoperation. The human operator plays a crucial role in teleoperation, having to perceive information from the remote environment through the human-system interface and act accordingly by sending commands to the remote devices. The task of the human-system interface can be summarized as follows.

- To excite the operator's senses, giving an indication of the status of the executed task in the remote environment.
- To process the operator's commands, ensuring proper control of the remote devices.

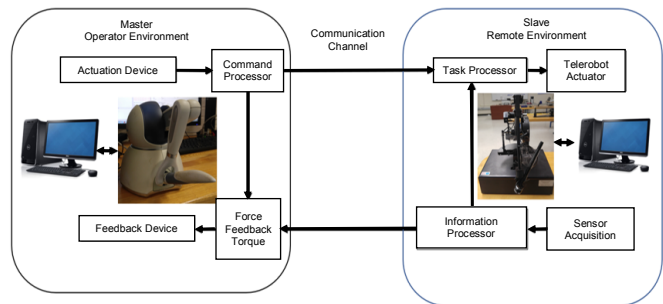


Figure 1. Schematic of the experimental haptic feedback telerobotic system used for this study.

The operator generates command signals at the master site by means of the human-system interface. These commands are transmitted through a communication channel to the telerobot to perform the remote task. Using sensors at the remote site, a measured force is transmitted from the robot back to the operator through the human-system interface and perceived by the operator (Ferre, Buss, Aracil, Melchiorri, & Balaguer, 2007). In this paper, the authors summarize an approach for designing robust synchronized impedance control in haptic teleoperation to enhance transparency under time delay. There are several techniques in the literature on designing controllers for time delay systems, including the Pade' approximation, which is a rational approximation and results in a shortened fraction of the exponential time-delay term in the characteristic equation. This may result in instability (Silva, Datta, & Bhattacharyya, 2001). Prediction-based methods, such as the Smith predictor (Deshpande & Ash, 1983; Bahill, 1983), require precise model calculations, which may result in errors.

---

In this paper, the authors also describe how a PIV controller can be used with the Phantom Omni and Phantom Premium devices with haptic feedback sensations to design a robust controller for a bilateral teleoperation system. Manipulation of the joystick, referred to as the master, by the operator provides motion commands at the remote, slave end. The actual task is performed by the slave. Using a force sensor on the slave, reaction forces can be reflected back from the slave to the master; such a system is said to be bilaterally controlled. Teleoperation is a human-in-the-loop system, where the human operator conducts tasks in the remote environment using master and slave control. The feedback information from the slave to the master ensures improved performance in teleoperation by alerting the operator to changes in the status of the executed task.

Despite the fact that reflecting the encountered forces back to the human operator improves performance by enabling the human to rely on tactile senses, the presence of signal transmission delay may cause instability in the system. This phenomenon is known as delay-induced instability of force reflecting teleoperators. Classification of the telerobotic system's control architecture is based on the coupling characteristics between the human and the remote environment or the respective degree of autonomy in the slave system. The coupling can be realized through the direct exchange of motion and force signals between master and slave devices, as in bilateral control, or several controllers in a loop, as in supervisory or distributed control architectures. Therefore, the command signal is given by the human operator in the form of force to the master device, the human-system interface (HSI), resulting in a displacement. While the teleoperator (slave robot) responds by following the motion of the HSI (master), a display of the force resulting from the interaction of the slave robot with the environment is sent to the human operator via this interface (Ferre et al., 2007)

In position-force architecture (Lawrence, 1993), the idea is also to send master positions as commands for the slave to follow. But the interaction force at the slave is sent back directly as a reaction force to the master. If the slave faithfully reproduces the master motions and the master accurately feels the slave forces, the operator should experience the same interaction with the teleoperated task as does the slave. In this force reflection architecture, stability is often a problem unless the force feedback to the master is significantly attenuated.

The main goals of teleoperation from theoretical control point of view are:

- **Stability:** Ensure stable performance of the closed-loop system, irrespective of the distortions, delay,

and losses that impact stability.

- **Telepresence:** Provide the human operator with a sense of telepresence; this is referred to as transparency of the system between the environment and the operator. This gives the operator kinesthetic feedback as if the operator were physically in touch with the remote environment.

These goals conflict with each other; however, appropriate control system design with an ability to satisfy these requirements enables complex task execution like telesurgery by the human in addition to scaling his/her power to manipulate huge objects. Complications in teleoperated systems arise because the communication medium (wired or wireless) introduces distortion, delays, and losses that impact stability and performance (Hokayem & Spong, 2006). Anderson & Spong (1989) investigated PI controllers and passive transfer lines for stability in a teleoperation system with short time delays.

## Experimental Setup

The bilateral teleoperation system (see Figure 1) also contains the following:

1. A Phantom Omni with 3° of freedom force feedback sensation
2. A feedback controller implemented on a PC using MATLAB/Simulink
3. A Phantom Premium with 3° of freedom force feedback

## Frequency Response Modeling

Since the manufacturer does not provide parameters for the Phantom Premium device, experimental modeling was used to determine them. From this modeling, a linear model of the system could be determined. The principle is based on observing how the system reacts to different inputs, and from these input-output relations, a reasonable fit is obtained from which the parameters can be determined. By varying the frequency of the input and recording the resulting output, a Bode plot of the system is obtained. Table 1 presents data from a frequency response test on the Phantom Premium.

Figure 2 shows the Bode plot. From the Bode plot, the steady-state gain and the time constant of the system were obtained. The cutoff frequency can be found from the plot as  $\omega_c = 7.5 \text{ rad/s}$ . The time constant was found to be  $\tau = 0.0212 \text{ sec}$ . The steady-state gain, which is the gain at frequency  $f = 0$ , was found to be  $K = 3.6$ . The transfer function of the Phantom Premium can, then, be given by Equation 1:

Table 1. Frequency response data.

f(Hz)	Amplitude (V)	Maximum axial speed (rad/s)	Gain: G(w) (rad/s/V)	Gain: G(w) (rad/s/V, dB)
0.0	0.05	0.18	3.6	
1.0	0.05	0.7	14	22.93
2.0	0.05	0.18	3.6	11.13
3.0	0.05	0.15	3.0	9.5
4.0	0.05	0.0425	0.85	-1.42
5.0	0.05	0.0265	0.53	-5.51
6.0	0.05	0.0185	0.37	-8.64
7.0	0.05	0.0130	0.26	-11.7
8.0	0.05	0.0095	0.19	-14.42

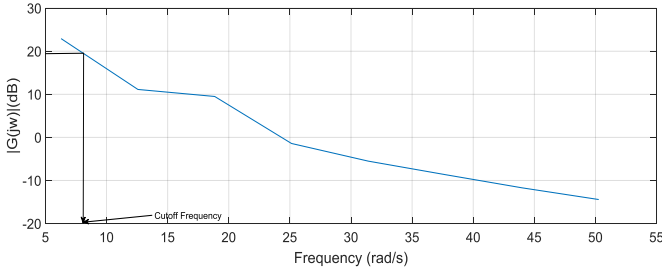


Figure 2. Bode plot of the Phantom Premium device.

$$P(s) = \frac{\text{Position (rad)}}{\text{Torque (N * rad)}} = \frac{K}{\tau s^2 + s} = \frac{3.6}{0.0212s^2 + s} \quad (1)$$

where, steady-state gain is  $K = 3.6$  and the time constant is  $\tau = 0.0212$  seconds.

## Modeling and Controller Design

With regards to the modeling and design of a PIV controller for the haptic feedback system considering time delay, DDEBIFTOOL was used to locate the dominant eigenvalues and design controller gains to continually shift the unstable eigenvalues in the right-half region of the s-plane to the stable left half of the s-plane. Figure 3 shows the block diagram for the haptic feedback system. The proportional-integral-velocity controller used to regulate the haptic feedback set to the master is shown in Equation 2:

$$V_m = K_i \int_0^t \dot{X}_a dt - K_p \theta_{2(t-h)} + K_v \dot{\theta}_{2(t-h)} \quad (2)$$

where, the slave position error is  $X_a = \theta_d - \theta_{2(t-h)}$ ;  $K_i$  is integral gain;  $K_p$  is proportional gain; and,  $K_v$  is velocity gain.

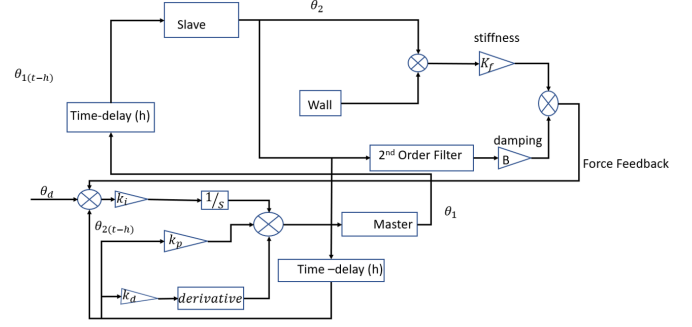


Figure 3. Block diagram of the haptic feedback system.

The force feedback from the slave agent is given by Equation 3:

$$F_f = K_f (\theta_2 - \theta_{wall}) - B \dot{\theta}_2 \quad (3)$$

where,  $F_f$  is force feedback;  $K_f$  is stiffness; and,  $B$  is the damping coefficient.

Table 2 provides a summary of the list of symbols used in the schematic diagram of Figure 3.

Table 2. List of parameters.

Symbol		Symbol	
$V_m$	Master controller voltage	$F_f$	Force feedback
$K_i$	Integral gain	$E$	
$K_p$	Proportional gain	$\theta_d$	Desired position
$K_v$	Velocity gain	$\theta_{2(t-h)}$	Delayed slave position
$K_f$	Stiffness	$\theta_{1(t-h)}$	Delayed master position
$B$	Damping coefficient		
$V_s$	Slave controller voltage		

The delay differential equation (DDE) for the haptic feedback control with time delay in matrix-vector form is given by Equation 4:

$$\dot{x}(t) = Ax(t) + A_d x(t-h), \quad t > 0 \quad (4)$$

$$\begin{bmatrix} \dot{x}(t) \end{bmatrix} = \begin{bmatrix} 0 & 1 & 0 \\ 0 & 0 & 1 \\ 0 & 0 & -\frac{1}{\tau} \end{bmatrix} x(t) + \begin{bmatrix} 0 & 0 & 0 \\ 0 & 0 & 0 \\ -\frac{KK_i}{\tau} & -\frac{KK_p}{\tau} & -\frac{KK_v}{\tau} \end{bmatrix} x(t-h)$$

where,

$$A = \begin{bmatrix} 0 & 1 & 0 \\ 0 & 0 & 1 \\ 0 & 0 & -\frac{1}{\tau} \end{bmatrix} \text{ and } A_d = \begin{bmatrix} 0 & 0 & 0 \\ 0 & 0 & 0 \\ -\frac{KK_i}{\tau} & -\frac{KK_p}{\tau} & -\frac{KK_v}{\tau} \end{bmatrix}$$

The solution for the system of delay differential equations DDEs is given by Equation 5:

$$SI - A - A_d e^{-sh} = 0 \quad (5)$$

where,  $e^{-sh}$  is the infinite spectrum;  $A$  and  $A_d$  are the  $nxn$  matrices; and,  $x(t)$  is the  $nx1$  state vector.

## Simulation and Experimental Results

The DDEBIFTOOL is MATLAB-based software for numerical bifurcation and stability analysis of delay differential equations with multiple fixed discrete and/or state-dependent delays. It enables the determination of dominant eigenvalues, enabling appropriate controller design to counteract the destabilizing effect of signal delay in the control system. By computing approximations and correction of dominant eigenvalues, stability analysis of steady-state solutions is achieved. Azorín et al. (2004) introduced a more generalized method by state convergence for teleoperated systems with time delay. Yoon et al. (2001) considered a different master device in model-based teleoperation. The authors of this current study, however, used the continuous pole placement method of addressing the time delay problem. The principle behind this approach is that even though time delay systems have infinite roots, the number of unstable eigenvalues is always finite (Hale & Lunel, 2013). The approach consists of moving the identified unstable eigenvalues to the stable left half plane by applying sensitivity-based changes to the controller gain  $K$ , while ensuring that the sub-dominant eigenvalues with large absolute real parts are monitored. Figure 4 shows how the rightmost characteristic root is computed and displayed.

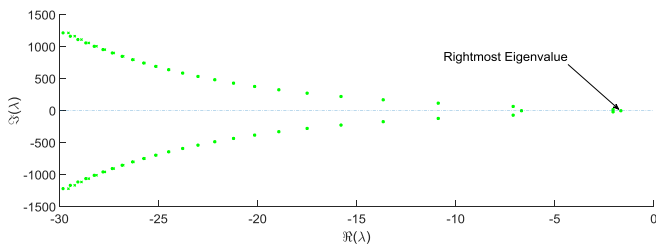


Figure 4. Characteristic roots spectrum of Phantom Premium showing dominant eigenvalue.

Using sensitivity analysis, the controller is tuned. Table 3 presents various combinations of gains  $K_p$ ,  $K_v$ , and  $K_i$  and the resulting dominant eigenvalues.

Table 3. Gains  $K_p$ ,  $K_v$ , and  $K_i$  from the PIV controller obtained by using the DDEBIFTOOL in MATLAB.

Real part of rightmost eigenvalue $\Re(\lambda_d)$	Gains			Time-delay, $h$
	$K_p$	$K_v$	$K_i$	
-1.88	1.5	0.01	2	0.1
-1.5	2.5	0.01	3	0.1
-1.68	2.5	0.01	5	0.1
-1	2.5	0.01	3	0.12
-0.54	2.5	0.01	5	0.12
-1.25	1.5	0.01	5	0.12
-1.85	1.5	0.01	2	0.12
-1.8	1.5	0.001	2	0.12

Figures 5-7 show the effects of time delay on controlled systems as well as simulated and experimental responses of a perfectly designed controller, without consideration of time delay. Figure 5 shows the results from a simulation of a stable response with the artificial delay block set to  $h = 0$ s. However, as artificial delay ( $h = 0.12$ s) is introduced in the feedback loop of the previously stable system, the simulated output shows an unstable response with a rightmost eigenvalue of  $+1.919 \pm i$  (see Figure 6). This is confirmed in the experimental response in Figure 7. In the experimental setup, delay in signal transmission results in an unstable system. Delay is a natural phenomenon; humans, for example, have various degrees of response to situations. In controls design, specialized techniques are used to design against the performance deteriorating effects of time delay. Figure 7 shows the previously stable system from Figure 5 becoming unstable when tested in an environment with time delay.

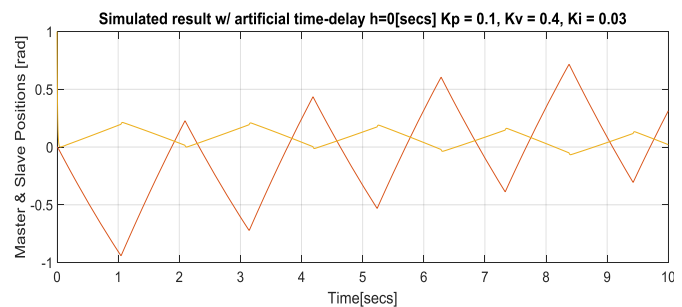


Figure 5. Simulated response of gains calculated w/o consideration of time delay and the artificial delay block set to  $h = 0$ .

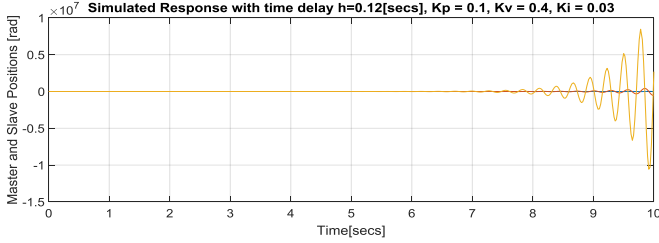


Figure 6. Simulated response of gains calculated w/o consideration of time delay and the artificial delay block set to ( $h = 0.12s$ ).

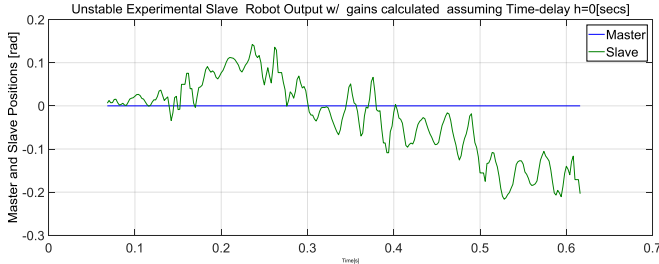


Figure 7. Experimental response is unstable due to delays of  $K_p = 0.1$ ,  $K_v = 0.4$ , and  $K_i = 0.03$ .

These results confirm the importance of taking time delay into consideration when designing controllers. Figure 8 shows the experimental results of the P IV master and slave positions with responses from various combinations of controller gains. Using sensitivity analysis, the response of the controller can be improved, thereby reducing noise and sluggish performance (see Figure 9). Figure 10 shows a perfectly synchronized bilateral teleoperated system. The effect of time delay can be seen in the overlapped response plot. The result shows that, with proper techniques and appropriate controller design, near perfect outputs can be obtained from the master and slave positions.

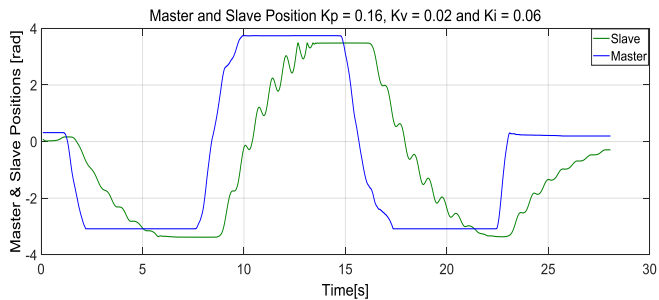


Figure 8. Experimental master and slave positions with an eigenvalue of  $-0.2745$ ,  $K_p = 0.16$ ,  $K_v = 0.02$ , and  $K_i = 0.06$ .

Figure 11 shows the system response with haptic feedback resulting from differences in angular position in master and slave as the master arm is moved to the right. This is very useful in teleoperation; for example, when the robot hits an obstacle while maneuvering in an inaccessible area.

Force feedback in telesurgery gives the operator a kinesthetic feel as to how much force is applied to/against an organ. In situations where the slave is interacting with the environment, the slave exerts a higher force on the environment as the position error increases. This results in a higher force feedback to the master.

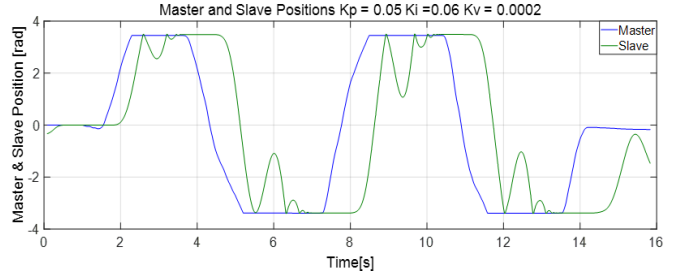


Figure 9. Experimental master and slave positions with an eigenvalue of  $-0.0764$ ,  $K_p = 0.05$ ,  $K_v = 0.0002$ , and  $K_i = 0.06$ .

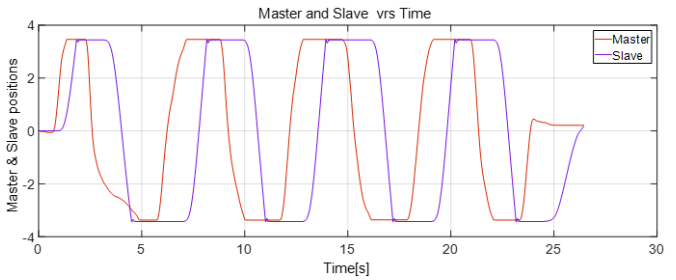


Figure 10. Measured angular position with a rightmost eigenvalue of  $-0.0764$ ,  $K_p = 0.05$ ,  $K_v = 0.02$ , and  $K_i = 0.06$ .

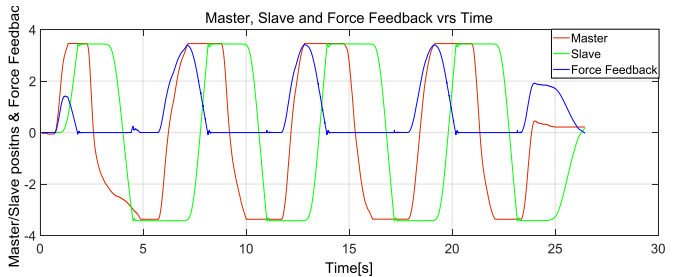


Figure 11. Master and slave positions showing force feedback each time there is a difference in angular positions to the right.

## Conclusions

In this paper, the authors presented an approach for designing an effective controller for a teleoperated system with haptic feedback. The authors first used the frequency response test to determine the parameters of the Phantom Premium, as the parameters are not provided by the manufacturer. Using DDEBIFTOOL, appropriate controller gains were determined for assigning the rightmost eigenvalues to the stable region of the  $s$ -plane. This is necessary because in

---

sending force feedback to the human-system interface HSI, the performance deteriorating effect of time delay arises making it imperative to design a controller with the capability of ensuring a robust and stable output under all conditions. To this end, the authors successfully demonstrated a way to model a teleoperated system with haptic feedback considering time delay.

Additionally, human factors are important in designing controllers for telerobotic systems. For example, delay in human response time can deteriorate transparency in teleoperation. The continuous pole placement method has many advantages, since it considers only the dominant eigenvalues and is not heavily reliant on solvers. Reflecting forces from the slave to the master enables the operator to perceive the remote environment through haptic feedback. This provides some form of communication with the operator and ensures better transparency. In the model, significant force feedback is transferred from the slave to the master when there is angular position difference in the master and slave. This property can be used to determine the state of the slave in the environment.

## Acknowledgments

This work was supported by the Department of Energy Minority Serving Institution Partnership Program managed by the Savannah River National Laboratory under SRNS contract DE-AC09-08SR22470.

## References

- Anderson, R. J., & Spong, M. W. (1989). Bilateral control of teleoperators with time delay. *IEEE Transactions on Automatic Control*, 34(5), 494-501.
- Azorín, J. M., Reinoso, O., Aracil, R., & Ferre, M. (2004). Generalized control method by state convergence for teleoperation systems with time delay. *Automatica*, 40(9), 1575-1582.
- Bahill, A. (1983). A simple adaptive smith-predictor for controlling time-delay systems: A tutorial. *Control Systems Magazine*, 3(2), 16-22.
- Deshpande, P. B., & Ash, R. H. (1983). *Elements of computer process control, with advanced control applications*. Research Triangle, NC: Instrument Society of America.
- Ferre, M., Buss, M., Aracil, R., Melchiorri, C., & Balaguer, C. (2007) Introduction to advances in telerobotics. In M. Ferre, M. Buss, R. Aracil, C., Melchiorri C., & Balaguer C. (eds.). *Advances in telerobotics*. Berlin: Springer.

- Hale, J. K., & Lunel, S. M. V. (2013). *Introduction to functional differential equations*. New York: Springer.
- Hokayem, P. F., & Spong, M. W. (2006). Bilateral teleoperation: An historical survey. *Automatica*, 42(12), 2035-2057.
- Lawrence, D. A. (1993). Stability and transparency in bilateral teleoperation. *IEEE Transactions on Robotics and Automation*, 9(5), 624-637.
- Okore-Hanson, T., & Yi, S. (2016). Adaptive synchronization of networked multi-agent systems considering transient responses and disturbances. *Proceedings of the International Symposium on Flexible Automation*. Piscataway, NJ: IEEE.
- Okore-Hanson, T., & Yi, S. (2017). Internet-based teleoperation of carts considering time delay via continuous pole placement. *American Journal of Engineering and Applied Sciences*, 10(2), 327-333.
- Silva, G. J., Datta, A., & Bhattacharyya, S. (2001) Controller design via Padé approximation can lead to instability. *Proceedings of the 40th IEEE Conference on Decision and Control*. Piscataway, NJ: IEEE.
- Tzafestas, C., Velanas, S., & Fakiridis, G. (2008). Adaptive impedance control in haptic teleoperation to improve transparency under time-delay. *Proceedings of the IEEE International Conference on Robotics and Automation*. Piscataway, NJ: IEEE.
- Yoon, W.-K., Tachihara, S., Tsumaki, Y., & Uchiyama, M. (2001). Evaluation of the different master device approaches for a model-based space teleoperation system. *Proceedings of the 10th International Conference on Advanced Robotics*. Piscataway, NJ: IEEE.

## Biographies

**THEOPHILUS OKORE-HANSON** is a postdoctoral researcher at North Carolina A&T State University. He received his PhD in mechanical engineering from North Carolina A&T State University (2017), MS in automotive engineering (2006) from the University of Applied Science, Offenburg, Germany, and BS in mechanical engineering (2000) from the Kwame Nkrumah University of Science and Technology, Ghana. His research interests include mechanical control design, robotic teleoperation, and design of controls for harnessing energy for renewable resources. Dr. Okore-Hanson may be reached at [tokoreha@aggies.ncat.edu](mailto:tokoreha@aggies.ncat.edu)

**SUN YI** is an associate professor in the Department of Mechanical Engineering at NCA&T. His research interests include the development of methods for analysis and control algorithms of dynamic systems. He has managed research projects in various areas, including networked autonomous vehicle systems and adaptive control of robot systems. Dr. Yi may be reached at [syi@ncat.edu](mailto:syi@ncat.edu)

---

**SAMEER A. HAMOUSH** is a professor of structural engineering. He received his PhD in structural engineering/mechanics from North Carolina State University (1988), MS from the University of Nebraska, and BS from Damascus University. His research interests include damage assessment and structural repair, NDT of concrete structures, fracture mechanics, composite materials, and modeling and simulation of metal powder for additive manufacturing. Dr. Hamoush may be reached at [sameer@ncat.edu](mailto:sameer@ncat.edu)

**YOUNHO SEONG** is an associate professor of industrial and systems engineering at North Carolina A&T State University. His series of work on human judgment and decision-making and trust in autonomous decision aids has been widely cited by the human cognition community as a way to improve human performance by making decision aids “more transparent.” Dr. Seong may be reached at [yseong@ncat.edu](mailto:yseong@ncat.edu)

# ANALYSIS AND SIMULATION OF NETWORKS WITH VIRTUAL CUT-THROUGH ROUTING

Lev B. Levitin, Boston University; Yelena Rykalova, UMass Lowell

## Abstract

In this study, the authors considered a model of a toroidal computer interconnection network with a virtual cut-through routing. The interrelationships between network parameters, load, and performance were analyzed. An exact analytical expression for the saturation point and expressions for network latency as a function of the message generation rate under the mean field theory approximation were obtained. The theoretical results were corroborated with the results of simulation experiments for various values of network parameters. The network behavior was found not to be dependent on the linear dimensions of the torus, provided that they are at least twice as large as the message path length. The saturation point was found to be inversely proportional to the message length, and in good agreement with the analytical results. A good agreement with Little's theorem was also found, if the network remained in the steady state during the experiment.

## Introduction

Modern approaches to supercomputer design rely on massively parallel computers (MPCs) and characterized by scalable architecture. As a result, these computers offer corresponding gains in performance as the number of processors is increased. Parallel code execution in such systems requires extensive communications between otherwise independent nodes. Since memory is not shared between node processors, inter-processor communications are achieved by passing messages between nodes through a communications network. This communications network is implemented as a network of interconnected routers, each having its own local processor (see reference list). Many commercially available parallel computers use a hypercube or mesh network configuration. The same principles are observed in popular network-on-chip (NoC) architecture and routing techniques. These network configurations provide convenient modularization and required scalability.

Various routing techniques are used in interconnection networks (Nikitin, & Cortadella, 2009; Kiasari, Lu, & Jantsch, 2013; Dabrowski, 2015; Li, Bashan, Buldyrev, Stanley, & Havlin, 2012; Chen et al., 2011; Liu & Carothers, 2011; Minkenberg, 2013; McCarthy, Isaacs, Bhatele, Bremer, & Hamann, 2014; Kermani & Kleinrock, 1979;

Duato, Robles, Silla, & Beivide, 2001; Kaushal & Singh, 2014; Domkondwar & Chaudhari, 2012; Lekariy & Gaikwad, 2013; Wang, Ma, Lu, & Wang, 2014; Choudhary & Qureshi, 2012; Levitin, Karpovsky, Mustafa, 2009; Levitin, Karpovsky, & Mustafa, 2006; Levitin, Karpovsky, & Mustafa, 2013; Karpovsky, Levitin, Mustafa, 2014; Sadawarte, Gaikwad, & Patrikar, 2011; Rexford & Shin, 1996; Hag, Hafizur Rahman, Nor, Sembok, Miura, & Inoguchi, 2015; Opoku Agyeman, Zong, Yakolev, Tong, & Mak, 2017; and Daf & Saynkar, 2014). The store-and-forward approach is based on the assumption that an entire message must be received at any intermediate node before it can be forwarded to the next node. Obviously, for a long message, the total delivery time may turn out to be quite large.

On the contrary, in wormhole routing, each message is divided into small packets or flits. The header flit contains information about source and destination, and is routed through the network according to this information and the routing algorithm. Other flits of the message follow the header flit. When the header flit of the message is blocked at an intermediate node, because the requested link is occupied by another message, the flits are buffered at each node along the path up to the current node. This forms a long "worm" that remains in the network and blocks other messages, thereby increasing their delivery time. Also, the problem of deadlocks emerges in this approach and should be dealt with (Levitin, Karpovsky, & Mustafa, 2009; Levitin, Karpovsky, & Mustafa, 2006; Levitin, Karpovsky, & Mustafa, 2013; and Karpovsky, Levitin, & Mustafa, 2014).

The virtual cut-through (VCT) routing algorithm is supposed to mitigate the drawbacks of both the aforementioned techniques (Chen et al., 2011; Minkenberg, 2013; Kermani & Kleinrock, 1979; Duato, Robles, Silla, & Beivide, 2001; Kaushal & Singh, 2014; Domkondwar & Chaudhari, 2012; Wang, Ma, Lu, & Wang, 2014; Sadawarte, Gaikwad & Patrikar, 2011; Rexford & Shin, 1996; and Hag et al., 2015). Unlike the wormhole approach, in VCT routing, if the next node cannot accept the message, the current node must still be able to buffer the rest of the incoming message from previous nodes. Thus the VCT algorithm achieves a much higher throughput and avoids deadlocks at the expense of increased buffer capacity. Several papers were devoted to the comparison between different routing techniques (Duato, Robles, Silla, & Beivide, 2001; Wang, Ma, Lu, & Wang, 2014). Analytical models of interconnection net-

---

works were considered in Nikitin & Cortadella, 2009; Kiasari, Lu & Jantsch, 2013; Rexford & Shin, 1996; and Kodgire & Shiurkar, 2015. Certain practical implementations were described in Chen et al., 2011; Liu & Carothers, 2011; Choudhary & Qureshi, 2012; Sadawarte, Gaikwad, & Patrikar, 2011; and Haag et al., 2015. Network latency in VCT networks is defined as the average time from the moment a message is generated by the source processor to the moment when the last flit of the message enters the consumption channel of the destination processor. The network latency consists of propagation delay, router delay, and contention (blockage) delay.

In this study, then, the authors looked at network latency and saturation using the VCT routing policy. Each network node included unlimited storage buffers. The “unlimited” buffer model means, in practice, that the network throughput is limited by the link occupancy (utilization), rather than by the buffer capacity. So, after the header is blocked, the “worm” collapses (condenses) into the storage buffer. This method prevents deadlocks and improves network performance (increases bandwidth, decreases latency, and delays saturation).

## Communication Network Model

The following assumptions were made for the network model implementation.

- The storage buffers are unlimited and use a FIFO (first-in, first-out) policy.
- The same clock is used for all network nodes.
- When a message is generated, it takes one time unit for its header (if not blocked) to appear at the router’s internal input port.
- It takes two time units (a time unit can include one or more clock cycles) to move a header flit from a router input port to its output port.
- It takes one time unit to move a flit (except the header) from a router input port to its output port.
- It takes one time unit to move a flit from the router output port to the input port of the next node (to go through the link).

## Network Topology Model

In many systems, where VCT routing may be used, the physical distance between communication nodes is small and, thus, unimportant. In such systems, real network topology can be abstracted without loss of generality as easily constructed lower-dimension meshes and tori. In this paper, the authors present a discussion of two-dimensional torus networks. The symmetry of toroidal networks leads to a more balanced utilization of communication links than

“open” mesh topologies and improves scalability. Each node in such a network consists of a router and a local processor. Each router has four external input/output (I/O) channels, and one internal input/output channel to the local processor. All I/O channels are bidirectional so that two messages may travel simultaneously in opposite directions between the nodes.

## Routing

Each I/O port of the router contains three buffers: input buffer, output buffer, and output storage buffer. These input and output buffers can hold only one flit at a time. In this current model, the storage buffer (which is an extension of the output buffer) was assumed to be unlimited. This means that it can hold as many messages as needed at any given moment in time. The local processor has the same one-flit-sized input and output buffers. Suppose that the local processor generates message M1 at time  $t_1$ , and another message M2 at time  $t_2$  ( $t_2 > t_1$ ). It is possible that at time  $t_2$  the router is still processing message M1 and that the link from the local processor to the router is busy. To handle this situation, an unlimited storage buffer, like the one at the external port, is introduced so that the local processor can store message M2 in its output storage buffer until the link is free. As a result, external and internal ports have the same three-buffer architecture. This allows for the use of the same software implementation for external and internal ports.

The authors believe that, in real-life implementation, the router processor needs more time (more time units) to route the header flit (to decode the destination, look up the routing table, and decide on which output port to send) then to route the remaining flits. This asymmetry is modeled by assigning two time units in the router for routing the header flit. Because all other flits of the message just follow the header, it takes one time unit in the router to send them to the correct output port. Network contention occurs if two messages compete for the same channel.

VCT networks generally outperform store-and-forward networks when the traffic patterns are sparse, but suffer substantial contention (leading to performance degradation) when the traffic is heavy. One way to address the issue of contention is to use adaptive routing, which allows a message to take an alternative path when the primary path (defined in the routing table) is blocked by another message.

The deadlock-free adaptive unicast VCT routing algorithm is described as follows:

- Every router has a (static) two-dimensional routing table relating minimum path length from each of the router’s four output ports to each network node.

- The routing table is used to perform dynamic routing based on the following set of rules:
- If the current node (at which the message header has arrived) is the destination, the header is routed to the internal port connecting to the local processor.
- If the current node is not the destination, the header of the message is sent from the input port to the output port, whichever has the shortest path to the destination node.
- In general, more than one output port may have the minimum distance to the destination; thus, the header is routed to the first available (free) port, where “first” refers to the port with the smallest number.
- If all ports with the minimum distance to the destination are busy, the router sends the header to the storage buffer of the one port whose number is the largest.
- If multiple headers arrive simultaneously, they should be routed to the same output port based on the rules described above, the header of the message with the smallest identification number will be processed first, and the header(s) of message(s) with larger identification number(s) will remain in the output storage buffer.
- Flits follow the header. If header motion is blocked, the header is routed to the storage buffer; all flits follow the header and accumulate (condense) in the storage buffer.

This routing algorithm assures that every link in the message path is occupied no longer than an amount of time equal to the message length.

## Message Generation

Assume that at each time unit, every node in the network can generate a message with probability  $\lambda$  independently of all other nodes. Destination nodes for generated messages are selected randomly among nodes having the specified distance  $l$  from the source node. Obviously, increasing  $\lambda$  increases the network load (the number of messages simultaneously traveling in the network), which, in turn, leads to latency growth until network saturation is reached.

## Theoretical Considerations

### Network States

Consider three different network states: startup, steady state, and saturation.

Initially, when network simulation starts up, there are no messages in the system. Then, new messages start appearing in the network. Even in the absence of other messages, a certain amount of time,  $\tau_{min}$ , is required for a message to reach its destination. During this time, more messages can be generated; so, after startup, the number of messages in the network increases. When network reaches its steady state, the average number of messages generated during time  $\Delta t$  equals the average number of messages delivered during the same time such that the number of messages in the system (in transit from source to destination) becomes virtually constant over time. For a meaningful evaluation of network latency, the network must reach its steady state before data on network behavior should be collected.

The network load increases with the number of messages present in the network and with the message length, since longer messages occupy links for longer periods of time. As a result, for each message length, the network can accommodate only a limited range of message generation rates. If the message generation rate is too high, the number of messages generated during time  $\Delta t$  exceeds the number of messages that can be delivered during this time, and the number of messages in the system increases unbounded. Thus, latency approaches infinity and the network becomes dysfunctional. This is the state of saturation. The rigorous theoretical analysis of network performance with the VCT routing is a challenging problem that, as far as the authors know, has not yet been done even under the conditions of Jackson’s theorem (1963). In this current study, the task was restricted to deriving an expression for the saturation point (message generation rate at which network saturation occurs) and approximate expressions for latency.

### Latency and Saturation Point

Let  $m$  be the length (the number of flits) of a message;  $n$  – the number of nodes;  $N$  – the number of messages in the network at a given moment of time;  $\tau$  – the network latency, as defined earlier; and,  $\rho$  – the link utilization (the probability that a link is occupied during a unit time interval). Also, let  $\tau_{min}$  be the minimum time required for a message to reach its destination (so-called base latency). Consider the case in which  $\lambda$  is very small (no blockages). A header needs one time unit to move from the output port of a router to the input port of the next one, two time units to move from the input port to the output port in the same router, and  $m$  time units to move all  $m$  flits through the consumption channel into the local processor at the destination node. It follows, then, that  $\tau_{min} = 3(l + 1) + m$ . Obviously, in the case of contention,  $\tau \geq \tau_{min}$ .

Denote by  $L$  the total average number of links occupied by a message during its average lifetime,  $\tau$ . Then, in the steady state,  $N^{l/\tau} = 4n\rho$ , where  $4n$  is the number of links (in both directions) in a 2-dimensional toroidal mesh. By Little's theorem,  $N = \lambda n \tau$ . Equation 1, then, is:

$$\frac{\lambda L}{4} = \rho \quad (1)$$

Equation 1 is exact in that it follows directly from the basic model. It is fulfilled for the entire range of values of  $\lambda$ , provided the network is in the steady state. In general, both  $L$  and  $\rho$  are functions of  $\lambda$ . Consider the case when  $\lambda$  is close to the critical value,  $\lambda_{cr}$ , that corresponds to saturation. Then  $\rho \rightarrow 1$ , which means that almost no free links exist in the system. As a result, the delay at every router becomes very long, such that all flits of a message get condensed into the output buffer of the router after which they do not occupy any links. It follows that, at any time interval, at most one link is occupied by a message. Because of the "condensation," the total number of links occupied by a message during all the time the header spends in one router is  $3 + (m - 3) = m$ . This yields Equation 2:

$$\lim_{\rho \rightarrow 1} L = L_{lim} = lm \quad (2)$$

Equations 1 and 2 yield an expression for the critical value,  $\lambda_{cr}$ , given by Equation 3:

$$\lambda_{cr} = \frac{4}{lm} \quad (3)$$

In the spirit of Jackson's theorem (1963), assume that all events, when a link is free or occupied, are independent. (This assumption is analogous to the "mean field theory" in statistical physics). Then the probability  $p(i)$  of delay  $i$  due to blockage can be determined using Equation 4:

$$p(i) = (1 - \rho) \rho^i, \text{ where } i = 0, 1, 2, \dots \quad (4)$$

The average time delay  $d(\rho)$  in a router due to contention can be determined using Equation 5:

$$d = d(\rho) = (1 - \rho) \sum_{i=0}^{\infty} i \rho^i = \frac{\rho}{1 - \rho} \quad (5)$$

An approximation for network latency  $\tau$  as a function of the generation rate  $\lambda$  can be obtained based on following analysis. Let message length  $m$  satisfy inequality  $m \geq 2l + 2$ . Let us assume for the moment that  $d$  is the exact value of the blocking delay at every router  $k$ , where  $k$  is the number of links from the source to the router. Then the general expression for the latency can be determined using Equation 6:

$$\tau = (l + 1)(d + 3) + m \quad (6)$$

The details of the propagation of the message along its path are different for three different ranges of values of  $d$ .

1. Small  $d$ :  $d \leq \frac{m+1}{l+1} - 3$
2. Intermediate  $d$ :  $\frac{m+1}{l+1} - 3 < d < m - 2$
3. Large  $d$ :  $d \geq m - 2$

Consider these three cases separately.

1. In the first case, small  $d$ , the end of the period of  $d + 3$  time units occurs when the header remains in router  $k$  and the message occupies all  $k$  links. Because of condensation, there are  $d + 2$  flits in router  $k$  and  $d + 3$  flits in routers 0 through  $k - 1$ . The number of flits remaining in the local processor of the source is  $m - (k + 1)(d + 3) + 1$ . It is readily seen that the total number of links,  $L$ , occupied by the message during its lifetime is given by Equation 7:

$$L = (d + 3) \sum_{k=1}^{k_d} k + l [(m - (l + 1)(d + 3) + 1) + (d + 3) \sum_{k=1}^{k_d} k - l] = lm \quad (7)$$

2. In the second case, intermediate  $d$ , the dynamics of propagation is different. Let  $k_d$  be the number of the router for which  $k_d = \frac{m - d - 2}{d + 3}$ . Then, the message always occupies  $k$  links when the header is in router  $k$  if  $k \leq k_d$ . The message occupies  $k_d + 1$  links during  $d + 2$  time units and  $k_d$  links during one time unit, when the header is in router  $k$ ,  $k_d + 1 \leq k \leq l$ . It follows that the total number of occupied links,  $L$ , can be determined by Equation 8:

$$L = (d + 3) \sum_{k=1}^{k_d} k + (d + 2)(l - k_d) + (l - k_d)k_d + (d + 3) \sum_{k=1}^{k_d} k - k_d = lm \quad (8)$$

3. In the third case, large  $d$ , all flits condense into one router before the header propagates to the next router. As discussed earlier, the total number of occupied links is the same, as was the case for the other two cases:  $L = lm$ .

In general, then, the total number of links occupied by a message over its average lifetime,  $\tau$ , does not depend on  $\lambda$ , as indicated by Equation 9:

$$L = lm \quad (9)$$

In fact, the blockage delay is not a constant, but a random variable,  $i$ , distributed according to Equation 4 with the expected value given by Equation 5. Hence, the average delivery time (the latency),  $\tau$ , being a linear function of the delay can be expressed by Equation 10:

$$\tau = (l + 1)(d + 3) + m = (l + 1) \left( \frac{\rho}{1 - \rho} + 3 \right) + m \quad (10)$$

Substituting  $L = lm$  into Equation 1, yields an expression for utilization given by Equation 11:

$$\rho = \frac{\lambda lm}{4} = \frac{\lambda}{\lambda_{cr}} \quad (11)$$

Equations 10 and 11 yield Equation 12:

$$\tau = (l + 1) \left( \frac{\lambda lm}{4 - \lambda lm} + 3 \right) + m \quad (12)$$

Equation 12 shows that the transition to saturation is a second-order (continuous) phase transition with a critical exponent equal to 1, which is in agreement with the mean field theory. Note that for small values of  $\lambda$  ( $\lambda \ll \frac{4}{lm}$ ), latency is a linear function of  $\lambda$  and depends linearly on the length of message  $m$ , while the dependence on distance  $l$  has a small quadratic term. For illustration purposes, it is convenient to use Equation 10 that yields latency in terms of utilization  $\rho$ . The plots of  $\tau$  as function of  $\rho$  with  $m$  and  $l$  as parameters are given in Figure 1.

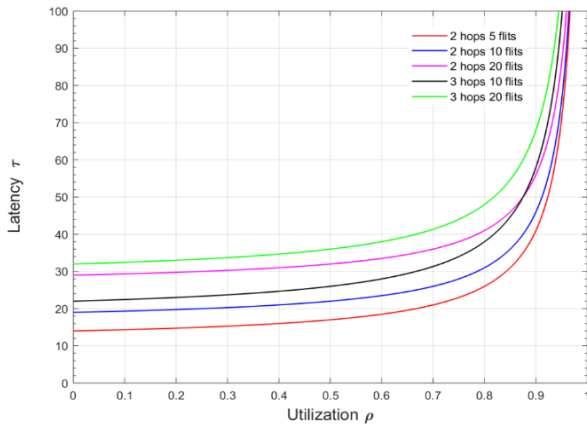


Figure 1. Theoretical approximation of latency,  $\tau$ , as a function of utilization  $\rho$ ;  $l = 2$ ; 3 hops;  $m = 5, 10, 20$  flits.

Consider now which buffer capacity is sufficient to justify the idealization of unlimited buffers. According to Little's theorem (Kleinrock, 1975), the average number of messages in the system under the steady-state condition is  $N = \lambda n \tau$ . Assuming the worst case scenario, when all messages are collapsed into storage buffers, the average number of flits per buffer  $\frac{1}{4} m \lambda \tau$ . Therefore, the required buffer size is critically dependent on how close the working range of  $\lambda$  is to  $\lambda_{cr}$ , as given by Equation 13:

$$B \approx \frac{1}{4} m \lambda \tau = \frac{\lambda}{\lambda_{cr}} \left[ \left( 1 - \frac{1}{l} \right) \left[ \frac{\lambda / \lambda_{cr}}{1 - \lambda / \lambda_{cr}} \right] + \frac{m}{l} \right] \quad (13)$$

If, for example,  $\lambda \leq 0.9 \lambda_{cr} = \frac{3.6}{lm}$ , then buffer capacity,  $B$ , should be on the order of  $B \approx 10.8 \left( 1 + \frac{1}{l} \right) + 0.9 \frac{m}{l}$ . If  $\lambda \leq 0.99 \lambda_{cr}$ , then  $\approx 50 \left( 1 + \frac{1}{l} \right) + \frac{m}{l}$ .

## Simulation Procedure and Results

Relatively small network sizes were chosen in order to reduce simulation time. The distances from source to destination and the message lengths varied for different experiments, but were assigned prior to the simulation and kept constant during simulation runs. Network performance is characterized by latency (average delivery time) as a function of the network load and by its saturation load, which describes maximum network capacity. Latency is obtained by averaging delivery times for all messages generated during time  $T$ . Time  $T$  was selected according to the value of  $l$  so that the total number of messages generated in the system during time  $T$  per each destination node would be about the same for all values of  $l$  (this number was about 120 in this current experiment). Since the average number of messages generated per unit of time is proportional to  $l$ , the following empirical formula was used to estimate  $T$ :  $T \approx 10 \times 4l / \lambda$ .

To ensure that the network was in its steady state during the data collection period, the delivery time was recorded for messages generated within the time interval of  $t_{min}, t_{min} + T$ , where  $t_{min}$  was sufficiently large. In each simulation run, the number of messages in the network was evaluated as a function of time in order to determine the network state and ensure that network latency was computed using data collected during the steady state. Message latency was calculated as a function of generation rate,  $\lambda$ , using message lengths of 5, 10, and 20 flits for mesh sizes ranging from  $n = 4 \times 4$  to  $n = 12 \times 12$  (for network linear sizes of  $s = 4, 6, 8, \text{ and } 12$ ). To ensure a steady state,  $t_{min} = 50,000$  was used.

Figure 2 shows latency for a small message length of  $m = 5$ . The results demonstrate latency dependence on path length  $l$ .

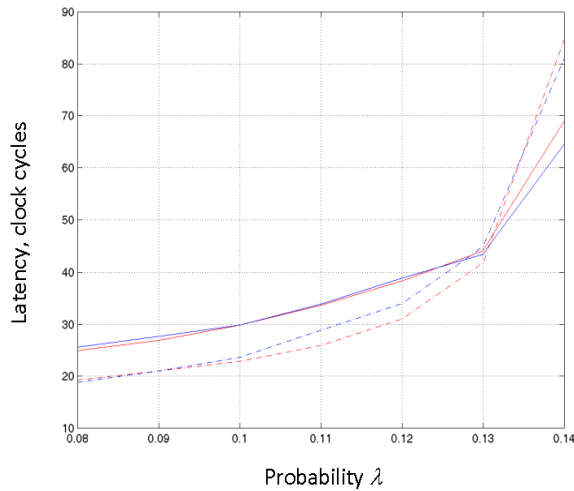


Figure 2. This graph shows latency for a message length of  $m = 5$  flits with mesh sizes of  $6 \times 6$  (blue lines) and  $8 \times 8$  (red lines), solid lines for  $l = 3$ , and dashed lines for  $l = 2$ .

Simulations were performed using  $l = 2$  and  $l = 3$  with longer messages. Figure 3 shows the results for  $l = 2$  with a message length of  $m = 10$  flits. Figure 4 shows the results for  $l = 2$  with a message length of  $m = 20$ . Since  $s \geq 2l$  for  $s = 6, 8, 12$ , and  $l = 2$ , similar network behavior was expected, while the results for  $d = 2$  were atypical ( $s < 2l$ ) and demonstrated early saturation.

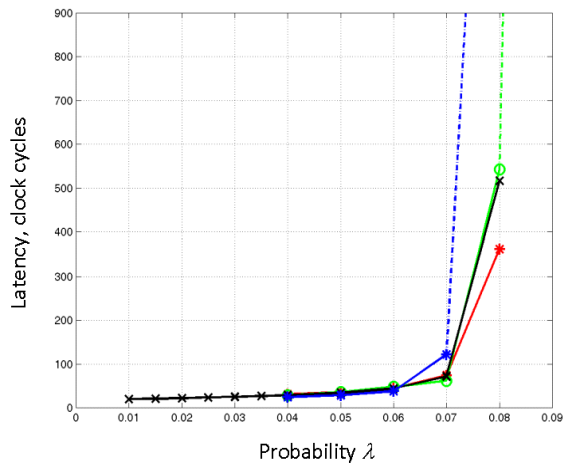


Figure 3. This graph shows latency for a message length of  $m = 10$  flits with a path length of  $l = 2$  hops, a solid line for steady state, a dashed line for where a steady state could not be reached, and mesh sizes of  $2 \times 2$  (blue line),  $4 \times 4$  (red line),  $6 \times 6$  (green line), and  $8 \times 8$  (black line).

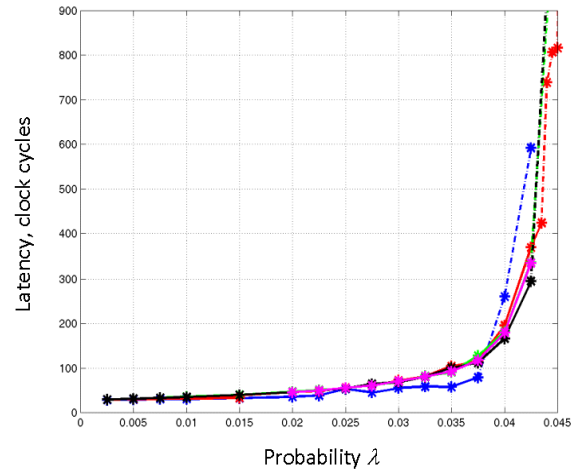


Figure 4. This graph shows latency for a message length of  $m = 20$  flits with a path length of  $l = 2$  hops, a solid line for steady state, a dashed line for where a steady state could not be reached, and mesh sizes of  $2 \times 2$  (blue line),  $4 \times 4$  (red line),  $6 \times 6$  (green line),  $8 \times 8$  (black line), and  $12 \times 12$  (magenta line).

Simulation results for  $l = 3$  are shown in Figures 5 and 6 for message lengths  $m = 10$  and  $20$ , respectively. Again, similar network behavior was observed when the condition  $s \geq 2l$  was satisfied. These results indicate that network behavior (latency and saturation point) does not depend on the mesh size if the mesh linear dimension,  $s$ , is at least twice the message path length,  $s \geq 2l$ . Results for latency dependence on the network load look somewhat paradoxical. It can be seen that if  $\lambda$  is small, latency is larger for longer paths. However, when  $m = 5$ , latency for the shorter path becomes larger for large values of  $\lambda$ , and saturation occurs earlier for the shorter path. This behavior is possibly related to the fact that the message length of  $m = 5$  is commensurate with the distance from the source to the destination. Seemingly, this effect disappears if the length of the message is large enough ( $m = 20$ ).

## Dependence of Message Latency and Saturation on Message Length

For the same message generation rate,  $\lambda$ , longer messages result in higher network loads. Thus, larger latencies and earlier saturation for longer messages are expected. Figure 7 shows message latencies for the 2-hop path in  $4 \times 4$ ,  $6 \times 6$ , and  $8 \times 8$  meshes for message lengths of  $m = 5$  (blue),  $m = 10$  (red), and  $m = 20$  (green). Results are shown using star symbols ( $*$  for  $4 \times 4$  the mesh, circles ( $\circ$ ) for the  $6 \times 6$  mesh, and crosses ( $\times$ ) for the  $8 \times 8$  mesh). Figure 8 shows similar results for 3-hop paths.

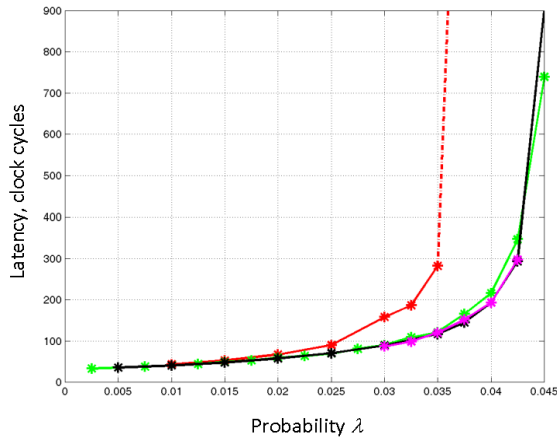


Figure 5. This graph shows latency for a message length of  $m = 10$  flits with a path length of  $l = 3$  hops, a solid line for steady state, a dashed line for where a steady state could not be reached, and mesh sizes of  $4 \times 4$  (red line),  $6 \times 6$  (green line), and  $8 \times 8$  (black line).

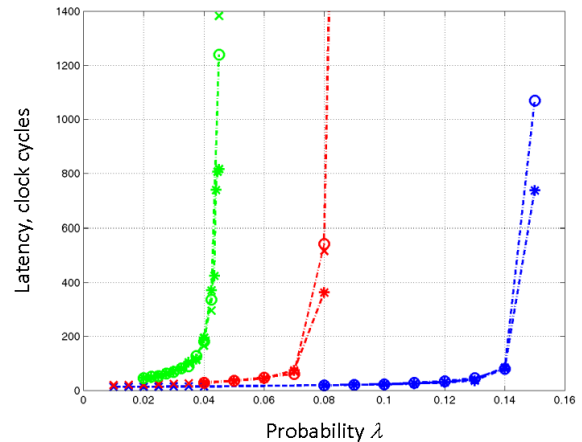


Figure 7. This graph shows latency as a function of  $\lambda$  for  $l = 2$  hops with message lengths of  $m = 5$  (blue lines),  $m = 10$  (red lines),  $m = 20$  (green lines), and mesh sizes of  $4 \times 4$  (•),  $6 \times 6$  (◦), and  $8 \times 8$  (×).

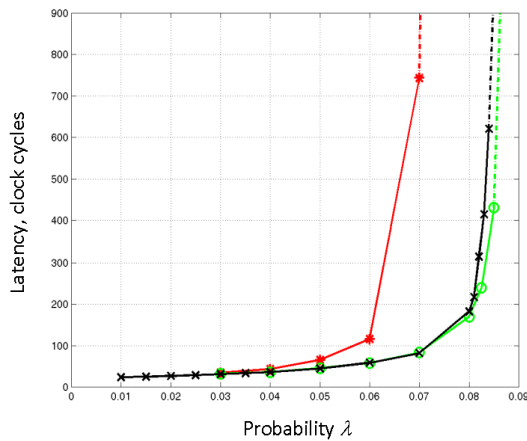


Figure 6. This graph shows latency for a message length of  $m = 20$  flits with a path length of  $l = 3$  hops, a solid line for steady state, a dashed line for where a steady state could not be reached, and mesh sizes of  $2 \times 2$  (blue line),  $4 \times 4$  (red line),  $6 \times 6$  (green line),  $8 \times 8$  (black line), and  $12 \times 12$  (magenta line).

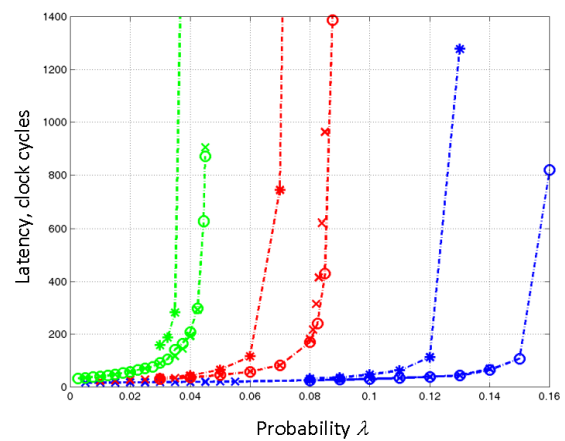


Figure 8. This graph shows latency as a function of  $\lambda$  for  $l = 3$  hops with message lengths of  $m = 5$  (blue lines),  $m = 10$  (red lines),  $m = 20$  (green lines), and mesh sizes of  $4 \times 4$  (•),  $6 \times 6$  (◦), and  $8 \times 8$  (×).

Obviously, network load increases with message length. Assuming that the network load is proportional to the product of the message length,  $m$ , and the message generation rate,  $\lambda$ , then one can expect that the message generation rate at which network saturation occurs ( $\lambda_{cr}$ ) is inversely proportional to message length  $m$ . The theoretical foundation for the hypothesis was presented earlier. The results of the numerical experiments were in a good agreement with this hypothesis (see Figure 9). It can be seen that for, all cases when  $s \geq 2l$ , the dependence of  $\lambda_{cr}$  of message length  $m$  can be closely approximated as  $\lambda_{cr} = 0.8/m$  (see the solid red line in Figure 9).

## Number of Messages as a Function of Message Load

In the steady state, the relationship between the average number of messages in the system and the latency is given by Little's theorem (Kleinrock, 1975):  $N = \lambda n \tau$ . Here,  $N$  and  $\tau$  are expected values of two random variables: number of messages in the network,  $N_s$ , sampled over the total period of observation, and the sample delivery time,  $\tau_s$ . Therefore, the values of  $N_s$  and  $\tau_s$  fluctuate with time and the relationship between  $N_s$  and  $\tau_s$  satisfies Little's theorem only approximately.

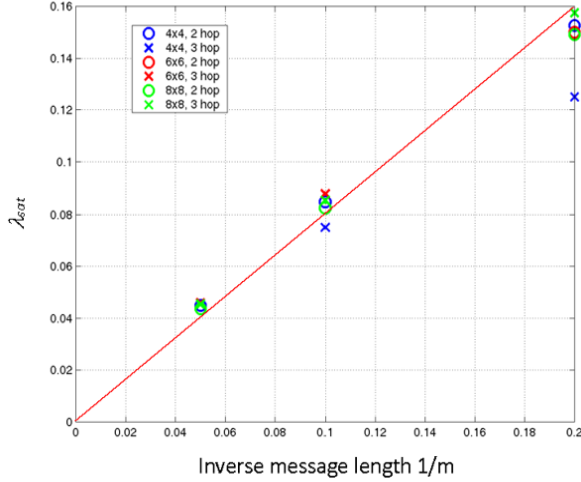


Figure 9. This graph shows the message generation probability at which network saturation occurs ( $\lambda_{cr}$ ) as a function of the inverse message length  $1/m$ , where the red line represents  $\lambda_{sat} = 0.8/m$ .

Values of  $N_s$  were measured by averaging the number of messages in the network from  $t_{min}$  up to the end of simulation, and the number of messages in the network were calculated using the observed values of  $\tau_s$ . Figures 10 and 11 show that the directly measured values of  $N_s$  and those calculated by the use of Little's theorem are in very good agreement, which supports the validity of the simulation experiments. However, it should be noted that when the state of the network is closed to saturation, the calculated number of messages usually exceeds the measured value.

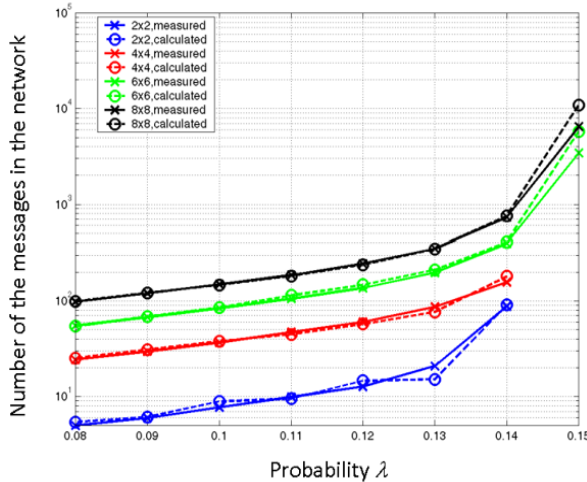


Figure 10. This graph shows the number of messages in the network as a function of  $\lambda$ , where a solid line represents values measured during simulation, a dashed line the calculated value by use of Little's theorem; and, where message length is  $m = 5$  Flits, and path length is  $l = 2$  hops.

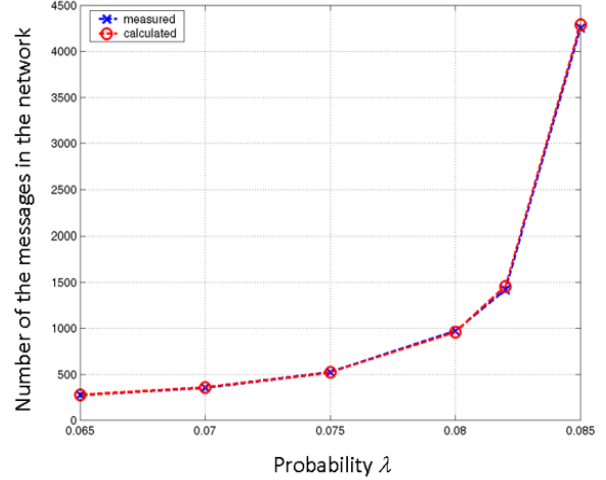


Figure 11. This graph shows the number of messages in the network as a function of  $\lambda$ , where mesh size is  $8 \times 8$ , message length is  $m = 10$  flits, and path length is  $l = 3$  hops; and, where a solid line represents measured values and a dashed line the calculated values.

## Conclusions

A model of a 2-dimensional toroidal interconnection network with virtual cut-through routing was studied. Analytical expressions for the saturation point and approximate expressions for the network latency for the ranges of small network loads and loads close to the critical value were obtained.

- The critical value of the probability of message generation,  $\lambda = \lambda_{cr}$ , is inversely proportional to the distance between the source and the destination,  $l$ , and the length of messages,  $m$ :  $\lambda_{cr} = \frac{4}{lm}$
- The latency,  $\tau$ , at the saturation point experiences a second-order (continuous) phase transition with the critical exponent equal to 1.
- For small values of  $\lambda$ , latency grows as a linear function of  $\lambda$ .

Simulation experiments were performed in order to determine and analyze certain empirical relationships that can be used as a starting point for a deeper theoretical analysis and further research. In particular, the following results were obtained.

- Network behavior (latency and saturation point) does not depend on mesh size, if the mesh is large enough with respect to path length. As an appropriate criterion, the mesh linear dimension should be at least twice as large as the message path length:  $s \geq 2l$ .
- For the same message generation rate, latency increases and saturation occurs earlier for longer messages. It appears that the saturation point,  $\lambda_{cr}$

(message generation rate at which the network saturates), is inversely proportional to message length. If the condition  $s \geq 2l$  is satisfied, numerical results are in a good agreement with a simple empirical relation  $\lambda_{cr} = 0.8/m$  independently of mesh size. (It seems to be consistent also with Equation 3).

- If the network is in the steady state, the independently measured number of messages,  $N_s$ , and the average delivery time,  $\tau_s$ , are in a good agreement with Little's theorem for their expected values of  $N = \lambda n \tau$ .

## References

- Chen, D., Eisley, N. A., Heidelberger, P., Senger, R. M., Sugawara, Y., Kumar, S., Salapura, V., ..., Parker, J. J. (2011). The IBM Blue Gene/Q interconnection network and message unit. *Proceedings of the 2011 International Conference for High Performance Computing, Networking, Storage and Analysis*. New York: ACM.
- Choudhary, S., & Qureshi, S. (2012). Performance evaluation of mesh-based NoCs: Implementation of a new architecture and routing algorithm. *International Journal of Automation and Computing*, 9(4), 403-413.
- Dabrowski, C. (2015, November). Catastrophic event phenomena in communication networks. *Computer Science Review*, 18, 10-45. doi: <https://doi.org/10.1016/j.cosrev.2015.10.001>
- Daf, M. P., & Saynkar, B. B. (2014). Performance and evaluation of loopback virtual channel router with heterogeneous router for on-chip network. *Proceedings of the 2014 Fourth International Conference on Communication Systems and Network Technologies*. Piscatawny, NJ: IEEE.
- Domkondwar, P., & Chaudhari, D. (2012). Implementation of five port router architecture using VHDL. *International Journal of Advanced Research in Computer Science and Electronics Engineering*, 1(3), 17-20.
- Duato, J., Robles, A., Silla, F., & Beivide, R. (2001). A comparison of router architectures for virtual cut-through and wormhole switching in a NOW environment. *Journal of Parallel and Distributed Computing*, 61(2), 224-253. doi: <http://dx.doi.org/10.1006/jpdc.2000.1679>
- Hag, A. A. Y., Hafizur Rahman, M.M., Nor, R. M., Sembok, T. M. T., Miura, Y., & Inoguchi, Y. (2015). Uniform traffic patterns using virtual cut-through flow control on VMMN. *Procedia Computer Science*, 59, 400-409. doi: <http://dx.doi.org/10.1016/j.procs.2015.07.553>
- Jackson, P. (1963). Job shop like queueing systems. *Management Science*, 10(1), 131-142.
- Karpovsky, M. G., Levitin, L. B., & Mustafa, M. (2014). Optimal turn prohibition for deadlock prevention in networks with regular topologies. *IEEE Transactions on Control of Network Systems*, 1(1), 74-85.
- Kaushal, A., & Singh, S. (2014). Network on chip architecture and routing techniques: A survey. *International Journal of Research in Engineering and Science*, 2(6), 65-79.
- Kermani, P., & Kleinrock, L. (1979). Virtual cut-through: A new computer communication switching technique. *Computer Networks*, 3(2), 267-286.
- Kiasari, A. E., Lu, Z., & Jantsch, A. (2013). An analytical latency model for networks-on chip. *IEEE Transactions on Very Large Scale Integration Systems (VLSI)*, 21(1), 113-123.
- Kleinrock, L. (1975). *Queueing systems volume I: Theory*. New York: Wiley.
- Kodgire, S., & Shiurkar, U. (2015). An analytical router model for networks-on-chip. *IOSR Journal of VLSI and Signal Processing*, 5(4), 16-21.
- Lekariya, D., & Gaikwad, M.A. (2013). Performance analysis of minimum hop source routing algorithm for two dimensional torus topology NOC architecture under CBR traffic. *IOSR Journal of Electronics and Communication Engineering*, 7(2), 5-12.
- Levitin, L. B., & Rykalova, Y. (2015). Analysis and simulation of computer networks with unlimited buffers. In A. -S. Pathan, M. Monowar, & S. Khan (Eds.). *Simulation Technologies in networking and communications: Selecting the best tool for the test* (pp. 3-300). St. Paul, MN: CRC Press.
- Levitin, L. B., & Rykalova, Y. (2016). Latency and phase transitions in interconnection networks with unlimited buffers. *International Journal of Modern Engineering*, 17(1), 70-77.
- Levitin, L. B., Karpovsky, M. G., & Mustafa, M. (2006). A new algorithm for finding minimal cycle-breaking sets of turns in a graph. *Journal of Graph Algorithms and Applications*, 10(2), 387-420.
- Levitin, L. B., Karpovsky, M. G., & Mustafa, M. (2009). Minimal sets of turns for breaking cycles in graphs modeling networks. *IEEE Transactions Parallel and Distributed Systems*, 21(9), 1342-1353.
- Levitin, L. B., Karpovsky, M. G., & Mustafa, M. (2013). Deadlock prevention in networks of workstations with wormhole routing: irregular topology. In A. Loo (Ed.). *Distributed innovations for business, engineering and science* (pp. 47-73). Hershey PA: IGI.
- Li, W., Bashan, A., Buldyrev, S. V., Stanley, H. E., & Havlin, S. (2012). Cascading failures in interdependent lattice networks: The critical role of the length of dependency links. *Physical Review Letters*, 108(22), 228702.
- Liu, N., & Carothers, C. D. (2011). Modeling billion-node torus networks using massively parallel discrete-event

- 
- simulation. *IEEE Workshop on Principles of Advanced and Distributed Simulation*. Piscataway, NJ: IEEE. doi: 10.1109/PADS.2011.5936761
- McCarthy, C. M., Isaacs, K. E., Bhatele, A., Bremer, P.-T., & Hamann, B. (2014). Visualizing the five-dimensional torus network of the IBM blue gene/Q. *Proceedings of the First Workshop on Visual Performance Analysis*. Piscataway, NJ: IEEE. doi: <http://dx.doi.org/10.1109/VPA.2014.10J>
- Minkenberg, C. (2013, May 21). *Interconnection network architectures for high-performance computing*. *Advanced computer networks*. [PowerPoint slides]. Retrieved from <https://manualzz.com/doc/13508828/interconnection-network-architectures-for-high-performance-computing>
- Nikitin, N., & Cortadella, J. (2009). A performance analytical model for network-on-chip with constant service time routers. *Proceedings of the 2009 International Conference on Computer-Aided Design*. New York: ACM.
- Opoku Agyeman, M., Zong, W., Yakolev, A., Tong, K.-F., & Mak, T. (2017). Extending the performance of hybrid NoCs beyond the limitations of network heterogeneity. *Journal of Low Power Electronics and Applications*, 7(2), 8.
- Rexford, J., & Shin, K. G. (1996). *Analytical modeling of routing algorithms in virtual cut-through networks*. Ann Arbor, MI: University of Michigan Press.
- Rykalova, Y., Levitin, L. B., & Brower, R. (2010). Critical phenomena in discrete-time interconnection networks. *Physica A: Statistical Mechanics and Its Applications*, 389(22), 5259-5278.
- Rykalova, Y., & Levitin, L. (2017). Phase transitions in interconnection networks with finite buffers. *International Journal of Modern Engineering*, 17(2), 33-40.
- Sadawarte, Y. A., Gaikwad, M. A., & Patrikar, R. M. (2011). Implementation of virtual cut-through algorithm for network on chip architecture. *IJCA Proceedings on International Symposium on Devices MEMS, Intelligent Systems & Communication, 1*, 5-8.
- Wang, P., Ma, S., Lu, H., & Wang, Z. (2014). A comprehensive comparison between virtual cut-through and wormhole routers for cache coherent network on-chips. *IEICE Electronics Express*, 11(14), 20140496-20140496.
- simulation, physics of computation, quantum computing, quantum theory of measurements, mathematical linguistics, theory of complex systems, coding theory, theory of computer hardware testing, reliable computer networks, and bioinformatics. He is a Life Fellow of IEEE, a member of the International Academy of Informatics and other professional societies. Prof. Levitin may be reached at [levitin@bu.edu](mailto:levitin@bu.edu)
- YELENA RYKALOVA** is currently an assistant professor at UMass Lowell and Visiting Researcher in the Department of Electrical and Computer Engineering at Boston University. Her research interests include computer networks, in particular in application of concepts and models of statistical physics to the analysis of network performance. She is a member of IEEE and the Society for Modeling and Simulation International (SCS). Since 2008, she has been active in the organization and preparation for the Spring Simulation Multiconference (SpringSim) as a technical committee member, reviewer, and publicity and session chair. Dr. Rykalova may be reached at [yelena\\_rykalova@uml.edu](mailto:yelena_rykalova@uml.edu)

## Biographies

**LEV LEVITIN** is currently a Distinguished Professor of Engineering Science in the Department of Electrical and Computer Engineering at Boston University. He has over 200 published papers, presentations, and patents. His research areas include information theory, quantum communi-

# INSTRUCTIONS FOR AUTHORS: MANUSCRIPT FORMATTING REQUIREMENTS

The INTERNATIONAL JOURNAL OF MODERN ENGINEERING is an online/print publication designed for Engineering, Engineering Technology, and Industrial Technology professionals. All submissions to this journal, submission of manuscripts, peer-reviews of submitted documents, requested editing changes, notification of acceptance or rejection, and final publication of accepted manuscripts will be handled electronically. The only exception is the submission of separate high-quality image files that are too large to send electronically.

All manuscript submissions must be prepared in Microsoft Word (.doc or .docx) and contain all figures, images and/or pictures embedded where you want them and appropriately captioned. Also included here is a summary of the formatting instructions. You should, however, review the [sample Word document](http://ijme.us/formatting_guidelines/) on our website ([http://ijme.us/formatting\\_guidelines/](http://ijme.us/formatting_guidelines/)) for details on how to correctly format your manuscript. The editorial staff reserves the right to edit and reformat any submitted document in order to meet publication standards of the journal.

The references included in the References section of your manuscript must follow APA-formatting guidelines. In order to help you, the sample Word document also includes numerous examples of how to format a variety of scenarios. Keep in mind that an incorrectly formatted manuscript will be returned to you, a delay that may cause it (if accepted) to be moved to a subsequent issue of the journal.

1. **Word Document Page Setup:** Two columns with ¼" spacing between columns; top of page = ¾"; bottom of page = 1" (from the top of the footer to bottom of page); left margin = ¾"; right margin = ¾".
2. **Paper Title:** Centered at the top of the first page with a 22-point Times New Roman (Bold), small-caps font.
3. **Page Breaks:** Do not use page breaks.
4. **Figures, Tables, and Equations:** All figures, tables, and equations must be placed immediately after the first paragraph in which they are introduced. And, each must be introduced. For example: "Figure 1 shows the operation of supercapacitors." "The speed of light can be determined using Equation 4:"

5. **More on Tables and Figures:** Center table captions above each table; center figure captions below each figure. Use 9-point Times New Roman (TNR) font. Italicize the words for table and figure, as well as their respective numbers; the remaining information in the caption is not italicized and followed by a period—e.g., "*Table 1.* Number of research universities in the state." or "*Figure 5.* Cross-sectional aerial map of the forested area."
6. **Figures with Multiple Images:** If any given figure includes multiple images, do NOT group them; they must be placed individually and have individual minor captions using, "(a)" "(b)" etc. Again, use 9-point TNR.
7. **Equations:** Each equation must be numbered, placed in numerical order within the document, and introduced—as noted in item #4.
8. **Tables, Graphs, and Flowcharts:** All tables, graphs, and flowcharts must be created directly in Word; tables must be enclosed on all sides. The use of color and/or highlighting is acceptable and encouraged, if it provides clarity for the reader.
9. **Textboxes:** Do not use text boxes anywhere in the document. For example, table/figure captions must be regular text and not attached in any way to their tables or images.
10. **Body Fonts:** Use 10-point TNR for body text throughout (1/8" paragraph indentation); indent all new paragraphs as per the images shown below; do not use tabs anywhere in the document; 9-point TNR for author names/affiliations under the paper title; 16-point TNR for major section titles; 14-point TNR for minor section titles.  

11. **Personal Pronouns:** Do not use personal pronouns (e.g., "we" "our" etc.).
12. **Section Numbering:** Do not use section numbering of any kind.
13. **Headers and Footers:** Do not use either.

- 
14. **References in the Abstract:** Do NOT include any references in the Abstract.
  15. **In-Text Referencing:** For the first occurrence of a given reference, list all authors—last names only—up to seven (7); if more than seven, use “et al.” after the seventh author. For a second citation of the same reference—assuming that it has three or more authors—add “et al.” after the third author. Again, see the *sample Word document* and the *formatting guide for references* for specifics.
  16. **More on In-Text References:** If you include a reference on any table, figure, or equation that was not created or originally published by one or more authors on your manuscript, you may not republish it without the expressed, written consent of the publishing author(s). The same holds true for name-brand products.
  17. **End-of-Document References Section:** List all references in alphabetical order using the last name of the first author—last name first, followed by a comma and the author’s initials. Do not use retrieval dates for websites.
  18. **Author Biographies:** Include biographies and current email addresses for each author at the end of the document.
  19. **Page Limit:** Manuscripts should not be more than 15 pages (single-spaced, 2-column format, 10-point TNR font).
  20. **Page Numbering:** Do not use page numbers.
  21. **Publication Charges:** Manuscripts accepted for publication are subject to mandatory publication charges.
  22. **Copyright Agreement:** A copyright transfer agreement form must be signed by all authors on a given manuscript and submitted by the corresponding author before that manuscript will be published. Two versions of the form will be sent with your manuscript’s acceptance email.
  23. **Submissions:** All manuscripts and required files and forms must be submitted electronically to Dr. Philip D. Weinsier, manuscript editor, at [philipw@bgsu.edu](mailto:philipw@bgsu.edu).
  24. **Published Deadlines:** Manuscripts may be submitted at any time during the year, irrespective of published deadlines, and the editor will automatically have your manuscript reviewed for the next-available issue of the journal. Published deadlines are intended as “target” dates for submitting new manuscripts as well as revised documents. Assuming that all other submission conditions have been met, and that there is space available in the associated issue, your manuscript will be published in that issue if the submission process—including payment of publication fees—has been completed by the posted deadline for that issue.

Missing a deadline generally only means that your manuscript may be held for a subsequent issue of the journal. However, conditions exist under which a given manuscript may be rejected. Always check with the editor to be sure. Also, if you do not complete the submission process (including all required revisions) within 12 months of the original submission of your manuscript, your manuscript may be rejected or it may have to begin the entire review process anew.

Only one form is required. Do not submit both forms!

The form named “paper” must be hand-signed by each author. The other form, “electronic,” does not require hand signatures and may be filled out by the corresponding author, as long as he/she receives written permission from all authors to have him/her sign on their behalf.



[www.ijeri.org](http://www.ijeri.org)

Print ISSN: 2152-4157  
Online ISSN: 2152-4165



[www.iajc.org](http://www.iajc.org)

## INTERNATIONAL JOURNAL OF ENGINEERING RESEARCH AND INNOVATION

### **ABOUT IJERI:**

- IJERI is the second official journal of the International Association of Journals and Conferences (IAJC).
- IJERI is a high-quality, independent journal steered by a distinguished board of directors and supported by an international review board representing many well-known universities, colleges, and corporations in the U.S. and abroad.
- IJERI has an impact factor of **1.58**, placing it among an elite group of most-cited engineering journals worldwide.

### **OTHER IAJC JOURNALS:**

- The International Journal of Modern Engineering (IJME)  
For more information visit [www.ijme.us](http://www.ijme.us)
- The Technology Interface International Journal (TIIJ)  
For more information visit [www.tiij.org](http://www.tiij.org)

### **IJERI SUBMISSIONS:**

- Manuscripts should be sent electronically to the manuscript editor, Dr. Philip Weinsier, at [philipw@bgsu.edu](mailto:philipw@bgsu.edu).

For submission guidelines visit  
[www.ijeri.org/submissions](http://www.ijeri.org/submissions)

### **TO JOIN THE REVIEW BOARD:**

- Contact the chair of the International Review Board, Dr. Philip Weinsier, at [philipw@bgsu.edu](mailto:philipw@bgsu.edu).

For more information visit  
[www.ijeri.org/editorial](http://www.ijeri.org/editorial)

### **INDEXING ORGANIZATIONS:**

- IJERI is currently indexed by 16 agencies. For a complete listing, please visit us at [www.ijeri.org](http://www.ijeri.org).

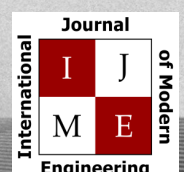
### **Contact us:**

**Mark Rajai, Ph.D.**

Editor-in-Chief  
California State University-Northridge  
College of Engineering and Computer Science  
Room: JD 4510  
Northridge, CA 91330  
Office: (818) 677-5003  
Email: [mrajai@csun.edu](mailto:mrajai@csun.edu)



[www.tiij.org](http://www.tiij.org)



[www.ijme.us](http://www.ijme.us)

# THE LEADING JOURNAL OF ENGINEERING, APPLIED SCIENCE AND TECHNOLOGY

**The latest impact factor (IF) calculation (Google Scholar method) for IJME of 3.0 moves  
it even higher in its march towards the top 10 engineering journals.**

**IJME IS THE OFFICAL AND FLAGSHIP JOURNAL OF THE  
INTERNATIONAL ASSOCIATION OF JOURNALS AND CONFERENCE (IAJC)**

[www.iajc.org](http://www.iajc.org)



The International Journal of Modern Engineering (IJME) is a highly-selective, peer-reviewed journal covering topics that appeal to a broad readership of various branches of engineering and related technologies. IJME is steered by the IAJC distinguished board of directors and is supported by an international review board consisting of prominent individuals representing many well-known universities, colleges, and corporations in the United States and abroad.

## **IJME Contact Information**

**General questions or inquiries about sponsorship of the journal should be directed to:**

**Mark Rajai, Ph.D.**

**Editor-in-Chief**

**Office: (818) 677-5003**

**Email: [editor@ijme.us](mailto:editor@ijme.us)**

**Department of Manufacturing Systems Engineering & Management**

**California State University-Northridge**

**1811 Nordhoff St.**

**Northridge, CA 91330**